UNIVERSIDAD DE CHILE
FACULTAD DE CIENCIAS FÍSICAS Y MATEMÁTICAS
DEPARTAMENTO DE CIENCIAS DE LA COMPUTACIÓN

PIECEWISE ADJACENT ACTIVE CONTOURS FOR MULTICELLULAR STRUCTURES IN FLUORESCENCE MICROSCOPY IMAGES

TESIS PARA OPTAR AL GRADO DE
DOCTOR EN CIENCIAS, MENCIÓN COMPUTACIÓN

JORGE FRANCISCO JARA WILDE

PROFESORA GUÍA:
NANCY HITSCHFELD KAHLER
PROFESOR CO-GUÍA:
STEFFEN HÄRTEL GRÜNDLER

MIEMBROS DE LA COMISIÓN:
BENJAMÍN BUSTOS CÁRDENAS
MIGUEL CONCHA NORDEMANN
FEDERICO LECUMBERRY RUVERTONI

SANTIAGO DE CHILE
2021

Resumen

La microscopía de fluorescencia permite observar fenómenos *in vivo* a nivel sub-celular, celular y supra-celular, con numerosas aplicaciones en ciencias biomédicas. Al usar marcadores fluorescentes para moléculas, organelos o células específicas, es posible observar el desarrollo de tejidos, órganos o embriones animales completos. En este contexto, la segmentación de membranas adyacentes en agregados celulares es un desafío pendiente: la bicapa lipídica de las membranas es muy fina en comparación con la longitud de onda de los fotones del espectro visible, los marcadores fluorescentes de membrana entregan una señal limitada, y la dispersión de la luz combinada con la dinámica en muestras vivas resulta en señales débiles o ambiguas que impiden su localización precisa. En células vecinas las membranas se acercan y distancian; protrusiones como blebs, filopodios y lamelipodios; *microvilli*; y el tráfico de vesículas, producen señales dinámicas variadas que dificultan aún más la localización. Existen muchos métodos de segmentación de membranas, pero no se enfocan en precisar la localización para membranas adyacentes. Esta tesis presenta un método basado en contornos activos paramétricos seccionados 2D que (i) detecta proximidad de contornos adyacentes, (ii) detecta secciones de contorno adyacentes, no adyacentes e intersectadas, (iii) define una polilínea como sección de contorno compartido optimizado entre dos secciones adyacentes, y (iv) conecta secciones adyacentes y no adyacentes bajo la restricción de conservar la morfología celular inicial. El método fue evaluado en imágenes de células de órgano parapineal de un embrión de pez cebra y sintéticas: detecta y corrige secciones de contorno adyacentes, no adyacentes e intersectadas, en función de una Distancia de Adyacencia d; calcula secciones compartidas para células vecinas con alteraciones mínimas de sus características, y entrega soluciones de contornos activos seccionados que preservan su morfología general. El método presentado puede usarse para mejorar algoritmos de mallas de superficie 3D, estimaciones de fuerzas, y/o seguimiento temporal. Se presentan fortalezas, limitaciones y casos extremos, y recomendaciones para aplicaciones en diferentes condiciones experimentales.

Abstract

Fluorescence microscopy allows *in vivo* observation of phenomena at sub-cellular, cellular and supra-cellular levels, with many applications in biomedical sciences. Fluorescent probes to label specific molecules, organelles, or cells, allow 2D/3D time-lapse imaging of living tissues, organs or embryos. In this context, the segmentation of adjacent cell membranes within cell aggregates remains an essential, challenging task. The lipid bilayer is a very thin membrane when compared to the wavelength of photons in the visual spectra. Fluorescent membrane markers provide a limited signal intensity, and the light scattering combined with sample dynamics leads to poor or ambivalent signal patterns that hinder an accurate localization of membrane sheets. In the proximity of cells, membranes approach and distance each other; the presence of membrane protrusions such as blebs, filopodia, and lamellipodia; microvilli; and vesicle trafficking, lead to a plurality of signal patterns, and accurate localization becomes harder. Several methods for membrane segmentation have been developed, but few of them address the issue of adjacent membranes. This thesis presents a method based on 2D piecewise parametric active contours that (i) defines proximity for adjacent contours, (ii) detects adjacent, non-adjacent, and overlapping contour sections, (iii) defines a polyline for an optimized shared contour within adjacent sections, and (iv) connects adjacent and non-adjacent sections under the constraint of preserving the initial cell morphology. The method was evaluated upon images of parapineal organ cells of a zebrafish embryo and a synthetic data set: it detects and corrects adjacent, non-adjacent, and overlapping contour sections within a selected Adjacency Distance d; calculates shared contour sections for neighboring cells with minimum alterations of the contour characteristics; and yields piecewise active contour solutions that preserve contour shape and overall cell morphology. The presented method can improve 3D surface meshing, force estimations, or contour tracking when combined with existing algorithms. Pitfalls, strengths, and limitations of the method are presented, together with a guideline for applications in varying experimental conditions.

Este trabajo se debe a la guía, apoyo, y paciencia extremada de los profesores Nancy Hitschfeld y Steffen Härtel. También, a la acogida, motivación y visión de los profesores Miguel Concha, Gregory Randall, Claudio Gutiérrez, Hartmut Dickhaus, Isaac Scherson, Karl Rohr y Jean Michel Morel, que en distintas y a veces sutiles maneras cruzan fronteras, disciplinas y generaciones. Además, muchas personas hicieron posible este trabajo antes del fin de siglo (¡o de mí!) con datos, experimentos, figuras y textos (útiles y de los otros), críticas, trámites, energía, ¡comida!, café y brebajes varios, cariño, y compañia, ya sea en momentos significativos o por una amistad de años. Los listo en orden de aparición para que no se peleen: Areli Cárdenas, Angélica Aguirre, Carmen "Yoya" Lemus, Ailen Signore, Karina Palma, Diego Sans, Martín Pinuer, Alcides Quispe, Carlos Bedregal, Felipe Olmos, Luis Silvestre, Ismael Figueroa, Eduardo Pulgar, Héctor Moraga, Omar Ramírez, Paola Scavone, Pablo Liddle, Felipe Santibáñez, Jan Scheer, Petra Narrog, Erika Labbé, Néstor Guerrero, Jorge Toledo, Alex Córdova, Jorge Mansilla, Sergio Pavez, Mauricio Cerda, Víctor Castañeda, Margarita Meynard, Patricio Ahumada, Etiene Verdugo, Juan Edo. Rodríguez, Miguel Colom, Nelson Monzón, Jamilet Miranda, Malcolm Moreno, Iván Castro, Loreto López, Camila Weiss, Marcela Aguirre, Francisca Valdés, Camilo Allende, Ignacio Gutiérrez, Anita Cancino, Karla Chandía. A ustedes, a mi familia y amigos de toda la vida, siempre presentes, gracias y pescado (frito :)

Acknowledgments

This thesis involved collaborative work with the following people: Carmen Gloria Lemus, Karina Palma, Francisca Valdés, Eduardo Pulgar, and Alex Córdova, from biomedical sciences; Mauricio Cerda, Jan Scheer, Víctor Castañeda, Héctor Moraga, Felipe Santibáñez, Juan Eduardo Rodríguez, and Iván Castro from medical informatics, electrical, electronics, and computer science engineering.

This work has been funded by the following agencies and grants:

- CONICYT PhD scholarships program in Chile.
- FONDECYT 1020579, 1181823, 1211988.
- FONDEF D11|1096.
- ICM P04-068F (Nucleus of Neural Morphogenesis, Chilean Millennium Scientific Initiative).
- ICM P09-015F (Biomedical Neuroscience Institute, Chilean Millennium Scientific Initiative).
- Center of Excellence for Innovative Research and Education in Medical Informatics, University of Chile and University of Heidelberg (DAAD, German Foreign Ministry).

Contents

1 Introduction **1**
1.1 Motivation . . . 1
1.2 Fluorescence Microscopy for Large Scale Imaging . . . 2
1.3 Segmentation for Morpho-Topological Analysis of Multi-Cellular Structures . 4
1.4 Thesis Contribution . . . 7
1.4.1 Publications, Related Work, and Collaborations . . . 8

2 Background: Active Contour Models and Multiple-Object Segmentation **11**
2.1 Membrane Detection in Fluorescence Microscopy . . . 12
2.1.1 Fluorescence Microscopy . . . 12
2.1.2 Membrane Segmentation Approaches . . . 15
2.2 Active Contour Models . . . 23
2.2.1 Parametric Models . . . 24
2.2.2 Implicit Models . . . 27
2.3 Multiple-Object Segmentation . . . 29

3 ALPACA: ALgorithm for Piecewise Adjacent Contour Adjustment **32**
3.1 Overview . . . 32
3.1.1 Input Parameters . . . 32
3.2 Algorithm Steps . . . 35
3.2.1 Gradient Vector Flow Image Force Computation . . . 35
3.2.2 Free Parametric Active Contour Deformation . . . 39
3.2.3 Detection of Adjacent, Overlapping, and Non-Adjacent Contour Sections 42
3.2.4 Shared Contour Section Computation . . . 42
3.2.5 Piecewise Active Contours Reconstruction . . . 44
3.3 Implementation Language and Libraries . . . 45
3.4 Implemented Optimizations . . . 45
3.4.1 Neighbor ROI/Shared Section Computations . . . 45
3.5 Computational Complexity . . . 46
3.5.1 Operations . . . 46
3.5.2 Memory . . . 46

4 Validation and Application **48**
4.1 Quality Indicators . . . 48
4.1.1 Morphological Indices . . . 48
4.1.2 Similarity Indices . . . 50

4.2 Test and Validation Cases 53
4.2.1 Microscopy Image Acquisition of PpO Cells 53
4.2.2 Synthetic Image with Hexagon Cells of Defined Adjacency 53
4.2.3 Manually Outlined Contours (MOC) 53
4.2.4 Algorithm Settings 54
4.3 Results and Discussion 57
4.4 Alternative Approaches 66

5 Conclusion **69**
5.1 General Remarks 69
5.2 Future Work 70

Bibliography **73**

Appendices **89**
A Statistical Analysis of Similarity Indices 89
A .1 Similarity Indices across Algorithm Steps in Synthetic Cells 90
A .2 Similarity Indices for Expert/Expert in Synthetic Cells 91
A .3 Comparison of Experts and ALPACA Steps in PpO Cells 94

List of Tables

2.1 Handling of Adjacent Sections within different segmentation approaches . . . 22

4.1 Variations of Morphological Indices for increasing Adjacency Distance d . . . 63
4.2 Pairwise Morphological and Similarity Indices between experts for membrane segmentation of PpO cells . . . 64
4.3 Morphological and Similarity Indices against Ground Truth for membrane segmentation of synthetic cells . . . 65
4.4 Morphological and Similarity Indices between experts for membrane segmentation of synthetic cells . . . 65

A1 Normality test of Experts/Ground Truth Similarity Indices in synthetic cells 92
A2 Friedman and *post hoc* Dunn tests applied to the Experts/Ground Truth Similarity Indices for MOC/PAC/ALPACA steps in synthetic cells . . . 92
A3 Normality test of Expert/Expert Similarity Indices in synthetic cells . . . 93
A4 Friedman and ANOVA/Tukey tests applied to the Expert/Expert Similarity Indices for ALPACA steps in synthetic cells . . . 93
A5 Normality test of Expert/Expert Similarity Indices from ALPACA steps in PpO cells . . . 95
A6 Friedman and ANODA/Tukey tests applied to the Expert/Expert Similarity Indices for ALPACA steps in PpO cells . . . 95

List of Figures

1.1 Large scale imaging with light-sheet microscopy 3
1.2 Acquisition, segmentation and morphological analysis of a fluorescent embryo 5
1.3 Membrane segmentation of a cell complex in a microscopy image 6

2.1 2D Intensity profiles of cell membranes in confocal fluorescence microscopy . 13
2.2 Effect of the Point Spread Function (PSF) in a point signal. 14
2.3 Manual and classical edge detector membrane segmentation examples 16
2.4 Threshold membrane segmentation examples 18
2.5 Anisotropic filtering membrane segmentation examples 20
2.6 Trained membrane segmentation example 21
2.7 2D Parametric Active Contours in a microscopy image of lipid monolayers . 26
2.8 2D implicit active contours in a microscopy image of a zebrafish embryo . . . 28

3.1 Segmentation and definition of contour sections in adjacent cell membranes . 33
3.2 Algorithm flowchart - ALPACA 34
3.3 Intensity gradients and edgemap in fluorescent PpO cell membranes 36
3.4 GGVF field in fluorescent PpO cell membranes 37
3.5 Algorithm flowchart - Parametric Active Contour adjustment 40
3.6 Parametric Active Contour deformation example 41
3.7 Correspondence Vertex Mapping defines shared contour sections 43
3.8 Algorithm flowchart - Axis-Aligned Bounding Boxes intersection 47

4.1 Distance and curvature of shared section with respect to ROI contour sections 55
4.2 Morphological Indices for increasing Adjacency Distance d 56
4.3 Optimized detection and adjustment of PpO cell membrane contour sections 57
4.4 Expert/Expert variations PpO cells segmented by MOC, PAC and ALPACA 61
4.5 Adjacent and non-adjacent sections calculated by ALPACA in synthetic test 62

Chapter 1

Introduction

This chapter gives an overview of object segmentation and analysis of cellular structures from live microscopy imaging, from a quantitative image processing perspective. To this end, light microscopy imaging techniques are introduced, together with image processing approaches for object segmentation and quantitative descriptions.

1.1 Motivation

High-resolution imaging and object analysis from massive data has become a key element for basic and applied sciences worldwide: robotics, astronomy, earth & life sciences, among many others. Continuous demand for extracting quantitative information from imaging data added to the ubiquity of imaging systems pushes technology to increase capacities for acquisition and processing. In particular, biological imaging and analysis techniques have become essential to improve time and space resolution for the study of several phenomena (such as [Vonesch et al., 2006, Skylaki et al., 2016, Pantazis and Supatto, 2014, Bengtsson, 2014]). In this context, fast and accurate mathematical-computational analysis tools have become as relevant as optics, fluorescence chemistry, or genetics.

In image analysis, the **segmentation** process aims to find regions of interest and is regarded as a first, crucial step [Marr, 1982]. Regions can be represented by geometric models suitable for quantifying morphology, topology[1], and dynamics, in order to describe organization and events at sub-cellular, cellular and supra-cellular levels [Meijering, 2012, Antony et al., 2013, Mikut et al., 2013, Castañeda et al., 2014]. Hence, segmentation leads to a representation of structures whose form and spatial distribution can be further analyzed for a given image or time series. To date, several segmentation approaches have been developed with a great variety of applications. Combined with object modeling techniques, they are essential for high-throughput scientific imaging, where most of the information is not accessible through visual inspection and thus cannot be quantified without automated approaches. In this context, proper modeling of expert knowledge remains a challenge in computer vision and

[1] It must be noted that the terms "morphology" and "topology" are used here according to their mathematical meanings, which may differ from their common usage in biology. Topology refers to the study of object properties such as continuity, boundaries and related features which are independent of size and shape, such as junctions and endpoints. Morphology, in turn, refers to size and shape object properties.

image processing research. Different constraints derive from application environments, such as real-time computation, precision thresholds, or interactivity. In particular, for microscopy image processing, skills for data acquisition, storing, and multi-dimensional analysis require intense collaboration at the interface of computer science, physics, and biology. The need for such interdisciplinary approaches is illustrated worldwide: established scientific centers like Janelia Farm[2], the Computational Neurobiology and Imaging Centre at Mount Sinai School of Medicine[3], and the BioQuant[4] gather researchers from different disciplines for the development of image analysis techniques in life science microscopy, with notable examples in STED [Hell et al., 2004] and PALM [Betzig et al., 2006], combining image processing and optics to overcome the diffraction barrier, achieving super-resolution imaging at nanometer-scale. Following this spirit, this thesis presents a segmentation approach for fluorescence microscopy *in vivo* imaging, suitable for structure and organization quantification, and intended to be integrated with time-lapse image analysis tools such as tracking and motion estimation. It addresses the issue of detecting non-adjacent, adjacent, and overlapping contour sections for active contours of single cells, and suggest a geometrically consistent solution for a common shared contour with cell neighbors under the constraint of maintaining the overall contour morphologies. This work sets out to enable access to physical interaction properties such as membrane adhesion and surface tension, by producing the best solution for cell-cell segmentation within the given constraints of acquisition setups.

1.2 Fluorescence Microscopy for Large Scale Imaging

Fast optical microscopy is the method of choice when it comes to *in vivo* observation and quantification of cellular dynamics, migration, tissue formation, or organization of whole organisms. The development of fast confocal microscopy techniques such as spinning disk or light sheet, in combination with fluorescent markers that can be encoded genetically, expressed *in vivo* and targeted to cell nuclei, organelles, membranes, or further constituents, contribute to increasing spatial/temporal resolutions and signal-noise ratios. In fluorescence microscopy, the specimens are not required to be fixed in order to be scanned, and 2D/3D time-lapse acquisition can be performed using multiple fluorescence channels, opening a new dimension for the study of dynamic processes that can be observed *in vivo* at the cellular, sub-cellular and supra-cellular level [Pawley, 2006]. However, image quality is always a trade-off between experimental needs and factors such as quantum yield, stability, and specificity of the fluorescent markers, as well as optics, illumination, filters, or detectors. Together, they define the signal quality and the size of the Point Spread Function (PSF) that collects the photon response of a single fluorescent emitter within the focal plane [Fink et al., 1998, Lakowicz, 2006, Waters and Wittman, 2014, Kubitschek, 2017] (see also Section 2.1.1). This poses an active research focus in mathematical and computational image processing, considering that:

1. State of the art microscopes can generate large amounts of image data, in the range of TiB[5] per minutes (Fig. 1.1). Examples are: light sheet or single-plane illumination [Verveer et al., 2007, Keller and Stelzer, 2008, Swoger et al., 2014], Bessel beam

[2] `http://www.hhmi.org/janelia/`

[3] `http://www.mssm.edu/`

[4] `http://www.bioquant.uni-heidelberg.de/`

[5] Here the international system designation is used, with 1 tebibyte (TiB) denoting 2^{40} bytes; 1 gibibyte (GiB), 2^{20} bytes, etc.

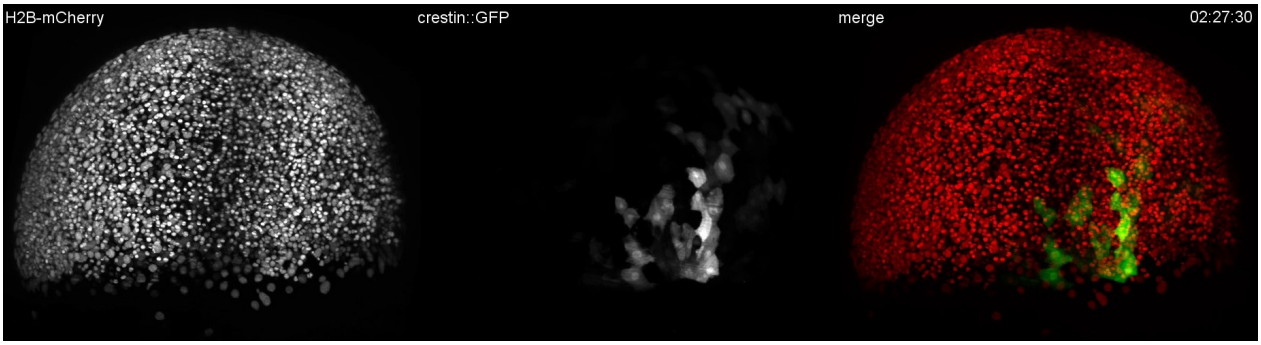

Figure 1.1: High-throughput microscopy generates high-resolution, high-speed image series of hundreds to thousands of cells in time windows ranging from minutes to days. The panels show the maximum-intensity projection of a 3D, 2-channel 4-lens multiview light-sheet microscope image stack of the gastrulation process in a fluorescent transgenic zebrafish embryo. **Left**: Cell nuclei (H2A-mCherry labeling) acquired by the light sheet microscope. **Center**: cell cytoplasm of the Kupffer's vesicle (asymmetry organ) dorsal forerunner cells (crestin:GFP labeling). **Right**: superposition of the nuclei (red) and cytoplasm (green) fluorescence channels. Image size: $2048 \times 2048 \times 400$ voxels, acquired every 1 minute for 24h, totaling ∼8TiB. Source: E. Pulgar & M.L. Concha (Laboratory of Experimental Ontogeny, U. of Chile); collaboration with Philipp Keller (Janelia Farm, HHMI, USA). Unpublished.

[Planchon et al., 2011], macro-zoom, and whole-slide scanning.

2. Optical microscopy constraints, such as light diffraction or labeling imprecision, often restrict the extraction of accurate descriptions from image content, requiring expert knowledge about experimental settings and features of interest.

3. Advanced mathematical-computational techniques for quantitative analysis of ROI structure and organization within known or bounded error margins, allow for comparison and a better understanding of experiments, as well as the discovery of novel phenomena at different organization levels [Keller et al., 2008, Vonesch et al., 2006, Skylaki et al., 2016, Pantazis and Supatto, 2014].

Figure 1.1 shows an example of a high-throughput imaging experiment, from the development of a fish embryo can be observed during several days by acquiring 2-channel 3D-images with a fast sample rate that allows capturing cell motion, deformation, organization, and proliferation. For such scenarios, proper computation capabilities for image acquisition, registration, segmentation, and subsequent analysis, become an essential component for biomedical imaging workflows [Meijering, 2012, Mikut et al., 2013]. Especially in fluorescence imaging, automated segmentation systems are still an open field, given the difficulties for defining ground truth/gold standards which depend on expert knowledge, and the variability of experimental conditions to take into account. Additional analysis tasks such as object characterization and classification can lead to different results depending on the methods and/or criteria used for segmentation. Geometry descriptors, mass distribution, and spatial orientation are examples of such cases [Castañeda et al., 2014, Pantazis and Supatto, 2014]. Thus, adequate ROI segmentation approaches, together with prior knowledge about the structures of interest, acquisition systems, and related image properties, will significantly improve both segmentation and morpho-topological analysis, as discussed next.

1.3 Segmentation for Morpho-Topological Analysis of Multi-Cellular Structures

Perception, quantification and understanding of the form of living cells and tissue are essential for basic and applied biomedical sciences. Examples from studies in morphogenesis, wound healing, and diseases are numerous and have motivated the development of image processing techniques and software tools in 2D and 3D [Mosaliganti et al., 2012, Brodland et al., 2014, Veldhuis et al., 2017]. The morphology of single cells, as well as their organization with respect to adjacent cells, are relevant for the mediation of cell-cell communication through biochemical signals (proteins, lipids, ions or gases), or mechanical stimuli through direct, physical contact [Veldhuis et al., 2017]. Regarding cell migration and tissue organization, the adjacency of cells and the direct contact between cell membranes mediate the type and strength of biochemical and mechanical interactions. The detection and quantification of adjacent and non-adjacent membranes, the number and temporal organization of neighboring cells, membrane morphology, angles formed at membrane junctions between two or more cells, and the number and morphology of cellular protrusions, are important for a better understanding of cell-cell communication. Cells can exert or respond to forces, and physical contact can stimulate or inhibit the formation of cell protrusions or migration [Richardson et al., 2016,Reig et al., 2017]. Adhesion forces and membrane contractility drive the formation of complex supra-cellular structures like vesicles or rosettes, and cell rearrangements such as intercalation, invagination or evagination. Specific examples are gastrulation [Montero and Heisenberg, 2004, Reig et al., 2017], laterality organ formation [Wang et al., 2012], and brain development in zebrafish [Concha et al., 2012, Signore and Concha, 2014, Richardson et al., 2016], endoderm cells evagination in ascidian embryos [Sherrard et al., 2010], and forces in epithelia of developing *Drosophila* [Aigouy et al., 2010, Bosveld et al., 2012, Ishihara and Sugimura, 2012] and mice [Pop et al., 2013]. Examples of contact-mediated inhibition of cell locomotion are summarized in a recent review [Roycroft and Mayor, 2018]. Cell collisions can stimulate the formation of protrusions and migration in the opposite direction of the contact site, loss of collisions between cancer and healthy cells is associated with metastasis. Understanding this kind of phenomena requires also the study of cell-cell interactions within events and processes at multicellular level, such as the extra-embryonic epithelial enveloping cell layer and the mesenchymal embryonic cell layer during early development in annual killifish [Reig et al., 2017]. Here, the enveloping layer is used by embryonic cells as a substrate for migration, directing the spreading of the embryonic tissue. Tissue-tissue interaction is mediated by cell adhesion and tension and relies on the ability of embryonic cells to couple motility to non-autonomous signals from the expanding enveloping layer. Multicellular-level phenomena is ubiquitous in living beings, and as such it can be observed not only during morphogenesis or organogenesis, but also in injury response processes, or disease progression/treatment, where studies are manifold (see reviews in [Friedl and Gilmour, 2009, Rørth, 2009, Castañeda et al., 2014]).

In summary, cell-cell and cell-medium contours need to be correctly identified and localized at both cellular and supra-cellular levels, and the segmentation of cell membranes becomes an essential task. The detection and quantification of intercellular junctions becomes also relevant, since they provide integrity to epithelia and other tissues, and the mechanical machinery necessary to execute morphogenetic and homeostatic intercellular rearrangements to coordinate tissue architecture with behavior [Yap et al., 2018].

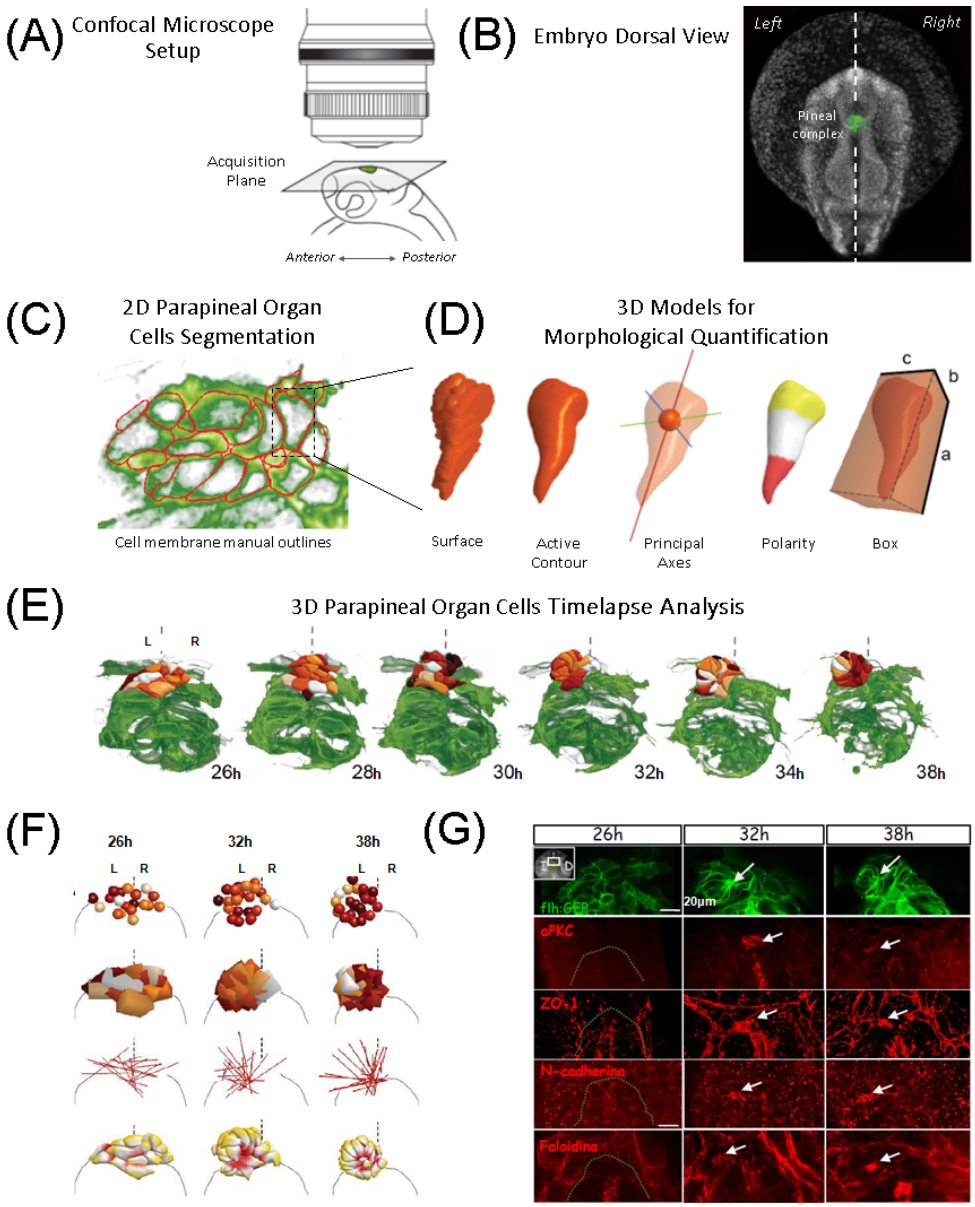

Figure 1.2: Acquisition, segmentation and morphological analysis models of a fluorescent embryo. **A:** Setup for PpO confocal microscopy imaging in a zebrafish embryo. **B:** Dorsal view of a transgenic *flh*::GAP43-EGFP zebrafish embryo acquired by fluorescence confocal microscopy with pineal complex cell membrane labeling (green) and nuclei staining (grey). **C:** 2D cell membrane segmentation of the PpO cells with manual outlining from fluorescence confocal spinning-disk microscope images. **D:** 3D surface-based models (Surface, Active Contour) and volume-based models (Principal Axes, Polarity, Box) for morphological analysis of the segmented PpO cells. **E:** 3D surface models of the PpO cells at different times (hpf), superposed to the fluorescence projection image of the pineal complex. **F:** Cell re-arrangement depicted by graphic models (from top to bottom: mass center, box overlap, principal axes, and cell polarity relative to the group mass center). **G:** Protein expression markers for membrane adhesion (n-cadherin), cell polarity (aPKC apical, ZO-1 basolateral), and actin cytoskeleton (phalloidin) indicate the formation of the PpO as a separate structure from the pineal organ. Published in [Lemus et al., 2017]. 3D models and descriptors implemented previously [Härtel et al., 2007].

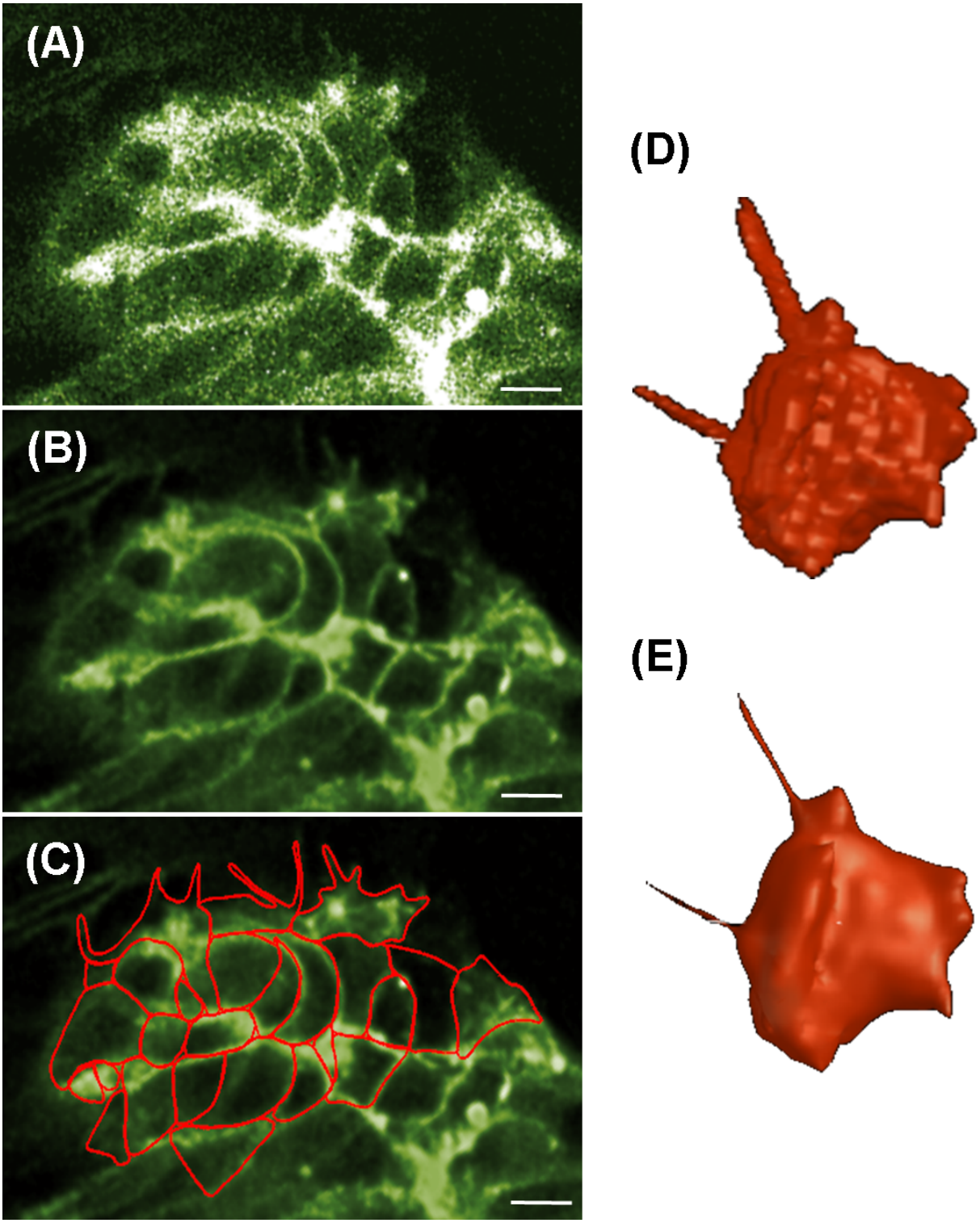

Figure 1.3: Membrane segmentation of a cell complex in a microscopy image. **A**: Sample slice from a 3D confocal microscopy image stack, showing the cells of the pineal complex in a zebrafish embryo. **B-C**: Segmentation of the pineal cell membranes (red contours), manually (B) and optimized with 2D active contours (C). Scale bar: 5 µm. **D-E**: Zoomed 3D surface models of a sample cell, reconstructed from the 2D segmented image slices, using a voxel-based approach (D) next to a 3D active contour approach (E). 3D models and algorithms implemented previously [Härtel et al., 2007].

Given the former, it becomes clear that models of interaction between cells are a key feature for processes simulation and characterization in both reference (control) and manipulated experimental conditions, in order to assess the state and behavior of single cells and their organelles, as well as higher level aggregates like tissues or organs (Fig. 1.3). ROI boundary descriptors become an essential element to quantify and further understand the interplay between cell form and function on the basis of properties like surface tension, membrane adhesion (*e.g.* number of cell neighbors or shared boundary percentage), junction angles between membranes, and protrusions. From the image processing perspective, proximity/adjacency between two or more objects can be used to improve ROI detection and optimization models by defining inter-object interaction properties, which can, at the same time, lead to their quantification from a given image set.

1.4 Thesis Contribution

This thesis contributes to improved segmentation of adjacent structures in images with limited resolution and/or signal strength. It presents an approach for finding and adjusting adjacent contour sections of two or more regions of interest (ROIs) in fluorescence microscopy images. The ALgorithm for Piecewise Adjacent Contour Adjustment (ALPACA) [Jara-Wilde et al., 2020] was defined considering:

1. a definition of proximity for adjacent ROI contours;
2. a detection criterion of adjacent, non-adjacent, and overlapping contour sections;
3. the definition of a polyline for an optimized shared contour within adjacent sections;
4. a solution for connecting adjacent and non-adjacent sections under the constraint of preserving the inherent cell morphology.

The test scenarios for ALPACA are a synthetic data set, and a group of neuroepithelial cells forming the PpO during morphogenesis in a zebrafish embryo. Quantitative analysis of morphology, membrane adjacency, and neighbor switching frequency, are the basis to understand underlying mechanisms of asymmetric morphogenesis of PpO cells and, more generally, the vertebrate brain. During morphogenesis, PpO cells form rosette-like structures that detach from the pineal complex and form a small brain nucleus [Concha et al., 2003, Härtel et al., 2007, Regan et al., 2009]. During this process, the cells change their shape and relationship with their neighbors, either by approaching/attaching or moving away/detaching. This is a very dynamic process in which the membrane of each cell undergoes deformations and displacements, with varying intercellular space between two or more neighboring cells. All these changes influence the observed fluorescent membrane signal and further hinder automatic segmentation approaches. ALPACA detects contour sections within a defined Adjacency Distance d, defines a polyline for optimized shared contours, and calculates a solution for connecting adjacent and non-adjacent sections under the constraint of preserving the inherent cell morphology and to obtain the best solution for cell-cell segmentation within the given constraints. ALPACA allows quantifying adjacent contours and can improve the meshing of 3D surfaces, the estimation of forces, or contour tracking when combined with existing algorithms. Pitfalls, strengths, and limits of ALPACA are presented, together with guidelines for applications under varying experimental conditions with *in vivo* microscopy.

1.4.1 Publications, Related Work, and Collaborations

To date, ten articles in indexed journals have been originated or derived from this thesis work. Eight of them are already published (first author in two), one is under revision, and one is in preparation. Eight articles are published in journals indexed by Web of Science[6] (formerly ISI), and one, by Scopus[7]. Contributions from the thesis author are listed below, grouped by topic, and with the corresponding field of knowledge of the publication in parenthesis.

The ALPACA approach

- The main ALPACA approach (microscopy and image processing) [Jara-Wilde et al., 2020]. First author.
- ALPACA applied to the 3D characterization of zebrafish embryos PpO cells (developmental biology) [Lemus et al., 2021].

2D Active contours with GVF/GGVF and contour interpolation techniques Implemented established algorithms [Kass et al., 1988, Xu and Prince, 1997], together with resolution control parameters for contour interpolation. Implemented approaches, parameter values, and resolution settings, were applied to the segmentation and morphological analysis of fluorescent structures.

- Time-lapse quantification of shape-dependent biophysical properties of lipid domains in monolayers (membrane biophysics) [Fanani et al., 2009].
- Segmentation combined with tracking approaches for time-lapse dynamics quantification of geometry in bacteria, macrophages, and extra-cellular traps (microbiology) [Mónaco et al., 2021].

Numerical PDE solvers and discrete differential operators Implemented and evaluated for motion estimation with established optical flow algorithms [Horn and Schunk, 1981, Bruhn and Weickert, 2005, Bruhn et al., 2002].

- Tests and comparison of optical flow algorithms in fluorescence images (image processing) [Delpiano et al., 2012]. Established algorithms for combined, local and global optical flow were implemented to compare different discrete differential operators and iterative linear system equation solving schemes, upon synthetic and real fluorescence microscopy image sequences. A reference framework was defined to allow comparing numerical approaches of Euler-Lagrange partial differential equations to minimize integral energy functionals, which are common for variational models of active contours and optical flow. Collaboration with a thesis work in electrical engineering [Delpiano, 2013], aimed to integrate ALPACA and tracking approaches for segmentation in 2D+time.
- An open access article for reproducible research (image processing) [Jara-Wilde et al., 2015]. Open source, peer-validated implementation of combined local-global optical flow approaches and PDE solver algorithms, in addition to a detailed evaluation with established performance metrics within an online demo, and synthetic and real sample images from sources other than microscopy. First author.

[6] `https://clarivate.com/products/web-of-science/`
[7] `https://www.scopus.com/`

Axis-aligned bounding boxes Implemented for 2D/3D ROI proximity and intersection computations. A collaboration for implementing the 2D Sweep-and-Prune algorithm was carried with a thesis project in computer science [Moraga, 2019]. The implemented algorithms were integrated with the broadband proximity computations for ALPACA (see 3.4). The 3D version was integrated with the SCIAN-Soft tools (see 3.3) for 3D segmentation and quantification.

- Neighboring/overlapping ROIs localization and distribution for the quantification of damage *foci* relative to DNA replication sites in culture cells with confocal microscopy (cellular biology and biochemistry) [Liddle et al., 2014].
- A follow-up work was published upon super-resolution microscopy experiments and data (cellular biology and biochemistry) [Liddle et al., 2020]. Clustering methods were applied to quantify the *foci* distribution in different experimental conditions.

Surveys

- Shape and dynamics of lipid monolayers, and derived properties in fluorescence images (membrane biophysics) [Fanani et al., 2010]. The GVF/GGVF active contour approach [Kass et al., 1988, Xu and Prince, 1997] applied to lipid domains is described and illustrated, together with the effect of contour resolution and force coefficients. The approach and its advantages were introduced and discussed for the tasks of segmentation and quantification of shape-related biophysical properties.
- Image processing methods for analysis of dynamic events in cell migration from fluorescence microscopy imaging: acquisition, registration, segmentation and quantification of morphology and topology [Castañeda et al., 2014]. Intended as a primer for live fluorescence microscopy users and researchers entering the field, that involves physics, chemistry, and signal/image processing concepts, all of which need to be considered in addition to the biological/medical experimental background. Filtering and segmentation techniques reviewed in this thesis served as a basis for elaborating the corresponding section of the survey, in addition to contributing with motion estimation/registration approaches such as optical flow, and other image processing methods such as PSF deconvolution.

In addition, the following first-author conference contributions were presented:

- "Modelos geométricos y análisis de imágenes biológicas 3D: un caso de aplicación". J. Jara, N. Hitschfeld-Kahler and S. Härtel. Encuentro de Tesistas, Jornadas Chilenas de Computación. Antofagasta, Chile. Nov. 15-19, 2010.
  3D intersection computation and proximity descriptors for surface mesh models in fluorescence microscopy.
- "Computational analysis for segmentation and description of biological structures in microscopy images". J. Jara, J. Delpiano, J. Scheer and S. Härtel. Chilean Society for Cell Biology XXIV Annual Meeting. Pucón, Chile. Nov. 01-05, 2010.
  Optical flow in moving fluorescent signals for cell biology.
- "Combining active contours and optical flow for semi-automated quantification of spatio-temporal cell-cell dynamics in microscopy image series". J. Jara, J. Scheer, C.G. Lemus, K. Palma, E. Pulgar, L. Briones, G. Reig, C. Figueroa, M.L. Concha, N. Hitschfeld-

Kahler and S. Härtel. International Conference on Systems Biology. Mannheim/Heidelberg, Germany. Aug. 28-Sep. 01, 2011.
Combined optical flow with active contours.

- "An IPOL publication story... Combined Local-Global Optical Flow". J. Jara, M. Cerda and S. Härtel. STIC-AmSud Reproducible Research on Image and Signal Processing Symposium. Apr. 06-08, 2015. Maceió, Brazil.
  Reproducible research in image processing, implementation and evaluation of optical flow algorithms in an open access journal.
- "Adjacent active contours for segmenting and quantifying aggregated cell membranes in fluorescence microscopy images". J. Jara-Wilde, I. Castro, C.G. Lemus, K. Palma, V. Castañeda, N. Histchfeld, M.L. Concha and S. Härtel. EMBO Workshop: Bridging cell and tissue mechanics to fate specification in development. European Molecular Biology Organization. Apr. 02-05, 2019. Santiago, Chile.
  The ALPACA approach applied for the first time to *in vivo* images.

The realization of this work involved collaboration with the following people:

- Carmen Gloria Lemus, Karina Palma and Eduardo Pulgar from LEO/SCIAN-Lab (BNI and University of Chile): images and figures.
- José Delpiano, Mauricio Cerda and Jan Scheer (SCIAN-Lab, BNI and University of Chile): co-implementation and evaluation of discrete operators in digital images and numerical solver algorithms for energy minimization approaches [Delpiano et al., 2012, Jara-Wilde et al., 2015].
- Héctor Moraga (University of Chile, DCC): Sweep-and-Prune algorithm for AABBs [Moraga, 2019].
- Víctor Castañeda, Felipe Santibáñez, Juan Eduardo Rodríguez, Iván Castro, and Mauricio Cerda from SCIAN-Lab; and Karina Palma, Carmen Gloria Lemus and Francisca Valdés from LEO/SCIAN-Lab: article writing, data processing, code/text reviewing, unit tests, and support in miscellaneous coding and evaluation tasks.

Chapter 2

Background: Active Contour Models and Multiple-Object Segmentation

In computer vision/image processing, segmentation is the process of partitioning a given image into multiple disjoint segments or subsets, with the goal of simplifying and/or changing its representation towards meaningful components that are easier to analyze [Shapiro and Stockman, 2001, Marr, 1982]. Image segmentation is typically used to locate objects of interest and its boundaries, which become ROIs or foreground in opposition to the background. ROIs can be regarded as sets of shapes and/or lines (squares, circles, curves, straight angles, etc.), but also, as real-world objects (cell membranes in the case of this work). The segmentation problem then requires criteria for finding and grouping image elements with common properties such as intensity/color homogeneity, discontinuities, or texture.

A very large number of segmentation approaches, ranging from simple pixel-level operations to highly complex models, has been devised to address different requirements for image analysis. Relatively simple criteria, such as pixel similarity, discontinuities (for ROI boundaries), or template matching approaches, can give a fast but rough estimation of total number, size and spatial distribution of ROIs like nuclei, vesicles or fibers, when they present homogeneous labeling. Images with weak ROI signals and/or complex structures like membranes and their protrusions (*e.g.* blebs, filopodia) require more advanced techniques to detect them among variable acquisition conditions [Pawley, 2006, Pantazis and Supatto, 2014]. This chapter sets the context for the issue of adjacent membrane detection addressed in this thesis. It starts with a review of fluorescence microscopy imaging and existing approaches for membrane segmentation. Next, active contour models, related image processing and computational geometry techniques for segmenting multiple objects are presented.

Notation An image I in n dimensions will be denoted as $I = I(\omega_1, \omega_2, ..., \omega_n)$, where the values of I represent a measurable feature, such as light intensity, color, depth, temperature, density, etc. In this work, 2D images are defined as arrays of pixels in a Cartesian grid, $I = I(\omega_1, \omega_2) = I(x, y)$, with discrete coordinates (pixels) and function values (light intensity readings). Unless stated otherwise, single values (grey-scale) are used.

2.1 Membrane Detection in Fluorescence Microscopy

Cell membranes are three-dimensional, continuous structures that enclose the cell organelles. They appear in microscopy images as lines or planes in 2D, depending on their orientation with respect to the acquisition plane. For fluorescence microscopy experiments, membranes are labeled with fluorophores: molecules capable of emitting light within known wavelength ranges that allow their acquisition. However, different factors from the sample and microscope optics hinder a precise localization, as described in Section 2.1.1. Current segmentation approaches suitable for membrane-like structures are reviewed in Section 2.1.2.

2.1.1 Fluorescence Microscopy

To label cellular structures of interest, fluorescence imaging relies mainly on two approaches: synthetic dyes that bind to the targets; and over-expression of exogenous DNA-encoded fluorescence proteins, translated and delivered to the targets through the cell machinery for *in vivo* experiments [1]. An ideal marker should bind only to the targets (specificity), have a small size in order to not alter the target observed position and size, in addition to physical-chemical properties for reliable time-lapse imaging [Pawley, 2006, Lakowicz, 2006, Waters and Wittman, 2014, Skylaki et al., 2016]. The marker also should be able to reach every target in the sample, requiring a perfect delivery mechanism. In practice, almost none of the aforementioned conditions can be fully attained, which results in non-homogeneous labeling that leads to non-uniform intensity profiles in the acquired images. Localizing membrane sheets, especially in adjacency zones, becomes difficult, since blurry, missing, or non-specific membrane signals are present throughout the images. In addition, cellular membranes exhibit intrinsically heterogeneous molecular expression timings, and present deformations like blebs, microvilli, or protrusions, which result in a plurality of signal patterns (Figs. 1.2 and 2.1).

Regarding the acquisition process, image quality is always a trade-off between experimental needs and factors such as quantum yield, stability, and specificity of the fluorescent markers, as well as optics, illumination, filters, and detectors that determine the PSF [Lakowicz, 2006, Pawley, 2006, Waters and Wittman, 2014, Kubitschek, 2017]. Confocal microscopes illuminate the whole 3D sample (xyz) and acquire one focal plane (xy) at a time, by blocking out the light from the rest of the sample (out-of-focus planes). This filtering is performed with physical devices that cannot entirely block the out-of-focus light -even with the current state of the art- and diffuses the ROI signals, affecting the image quality. In addition, optical microscopy is subject to the light diffraction limit, expressed in Abbe's law [Abbe, 1873], so the typical PSF diameter for an *in vivo* confocal microscopy setting, given by the full width at half-maximum, is $\sim$0.25 µm in the focal xy plane, and $\sim$0.8 µm in the optical sectioning z axis (Fig. 2.2). This is 50 to 160 times the thickness of a lipid bilayer of a eukaryotic cell membrane ($\sim$5 nm [Clausen et al., 2017]), whose orientation with respect to the focal membrane plane in combination with the PSF defines different intensity profiles. Fluorescence signals are integrated only within the convolution of the PSF with the fluorescent intensity distribution, which is a function of the density of fluorophores attached to or embedded within the membrane. In this regard, the effect of the convolution for different orientations of giant unilamellar vesicle membranes with respect to the PSF has been discussed

[1] In some cases the auto-fluorescence phenomenon can be used, with examples in plants or fungi. In others, the signals of interest could be masked by naturally autofluorescent molecules such as colagen or elastin.

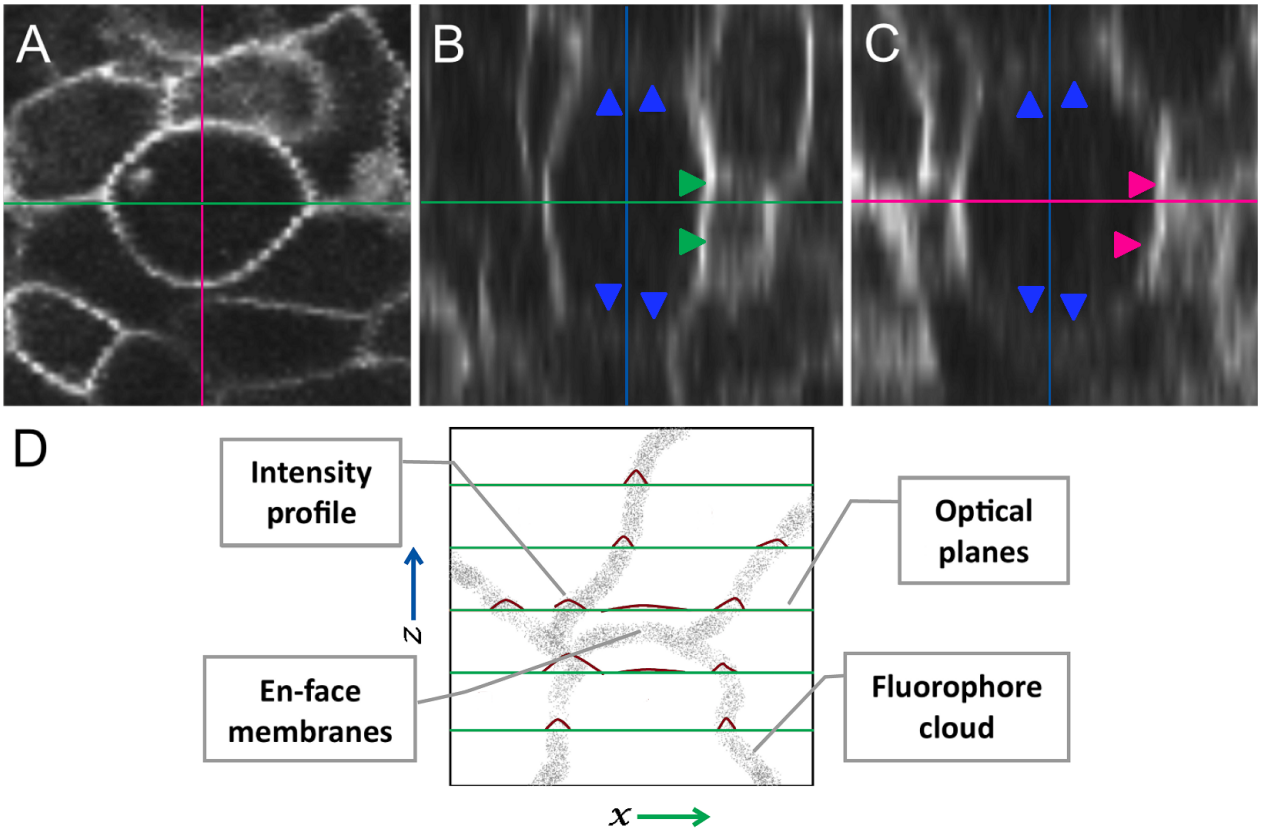

Figure 2.1: 2D Intensity profiles of cell membranes in confocal fluorescence microscopy. **A-C:** A cell with fluorescent membrane is shown centered, across orthogonal sections in the xy (A), xz (B), and yz (C) planes. Membrane sections orthogonal to the xy focal plane appear with a strong and uniform signal (green and magenta arrows), while sections en-face to xy (orthogonal to the xz and yz planes) appear a with weak and diffuse signal (blue arrows). **D:** A qualitative model describing the formation of a fluorescence membrane image with optical sectioning in 2D. Membrane signals are shown as a point cloud (input) in the xz plane. Sample xy focal planes are marked by green lines (orthogonal to the figure plane) and the resulting intensity profiles in the intersections are shown as plots (dark red). Cell membranes imaged oblique and en-face such as the interface between cells are difficult to resolve in comparison to those orthogonal to the focal planes. Adapted from [Mosaliganti et al., 2012].

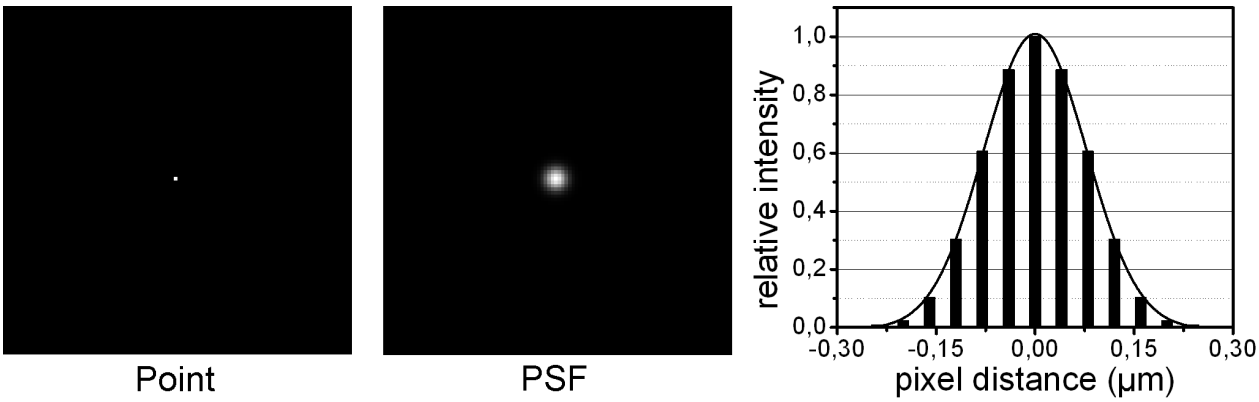

Figure 2.2: Effect of the Point Spread Function (PSF) in a point signal (1 pixel). **Left:** synthetic fluorescent point signal. **Center:** PSF-convolved point signal a confocal microscope. Images of 100×100 pixels were generated for a theoretical PSF from a confocal microscope with $60\times$ water objective, wavelengths of 543nm for excitation and 560nm for emission. Pixel size is 107 µm in x and y. **Right:** 1-dimensional PSF intensity profile. Published in [Delpiano et al., 2012].

(see for example [Fidorra et al., 2009]). Cellular membranes, however, are more complex than model membranes: they show deformations like blebs, microvilli, or protrusions, which result in images with a plurality of signal patterns, and the accurate detection of photon activity and membrane morphology becomes difficult [Fink et al., 1998, Mosaliganti et al., 2012]. The precise localization of a membrane sheet, especially when adjacent to a neighboring membrane becomes difficult, since blurry, missing, or non-specific membrane signals are present throughout the images (Fig. 2.3). It is frequent for neighboring cell membranes to appear adjacent along the z axis, but clearly separated within the xy plane due to the PSF shape [Mosaliganti et al., 2012].

To date, super-resolution approaches [Schermelleh et al., 2010] can help to overcome such limitation but they require fixed samples, high laser energy and/or limited fields of view, which makes them unsuitable for *in vivo* experiments. An additional issue for conventional confocal microscopes is the light that comes from outside the acquisition plane.Recent diffraction-limited techniques for selective plane illumination, also called light sheet microscopy (review in [Santi, 2011]), avoid illuminating the entire sample along its vertical axis. Instead, a quasi-planar z-section section orthogonal to the emission direction is excited with a light-sheet laser beam. This approach currently yields an out-of-focus region with a height below 500 nm [Ritter et al., 2010, Swoger et al., 2014, Mohan et al., 2014], but still with a resolution in the focal plane that is not improved over confocal systems.

An additional issue when fast acquisition is required for rapid events *in vivo*, either in 2D or 3D, is that low exposure times can result in low signal/noise ratios for the resulting image. Even with recent advances that significantly improve the emission efficiency [Clausen et al., 2017], an input quality trade-off between segmentation and motion estimation algorithms [Delpiano et al., 2012, Castañeda et al., 2014].

In the example case used for this thesis work, during zebrafish morphogenesis, the cells of the parapineal organ form rosette-like structures that detach from the pineal complex and

form a small brain nucleus [Concha et al., 2003, Härtel et al., 2007, Regan et al., 2009]. In this process, the cells change their shape and relationship with their neighbors, either by approaching/attaching or moving away/detaching. This is a very dynamic process in which the membrane of each cell undergoes different deformations and displacements varying the intercellular space between two or more neighboring cells. All of these changes influence the observed fluorescent membrane signal and result in further hindrances to automatic segmentation approaches that have precluded satisfactory performances so far.

2.1.2 Membrane Segmentation Approaches

Over the years, different algorithms for the detection and segmentation of cellular membranes have been introduced. However, the detection and appropriate handling of cell contours for multiple cells in tissue and whole organisms have not been solved on a general level so far. A summary of existing methods suitable for adjacent membranes is presented in Table 2.1, and a descriptive categorization of methods is presented next. A more extended review on segmentation methods for the analysis of dynamic events in cell migration with microscopy imaging can be found in a previously published work [Castañeda et al., 2014].

Template-based Operators

A simple approach is to look for line patterns in an image by finding aligned pixels, with the Hough transform [Hough, 1959] as the classical example. A complementary approach is the edge detection filtering which uses intensity gradient magnitudes (contrast) as ROI boundary indicators [Marr and Hildreth, 1980, Gonzalez and Woods, 2007, Nixon and Aguado, 2008]. Edge detection filters such as Sobel [Sobel, 1970] (Fig. 2.3C) or Prewitt [Prewitt, 1970] return the computed gradient image, upon which the Hough transform can be applied. With additional filtering, the Canny detector [Canny, 1986] (Fig. 2.3D) and derived approaches select only image pixels whose gradient magnitude is a local maximum and satisfies connectivity rules in order to yield thin ROI boundaries, without requiring them to be straight lines. Different methods for thinning can be also selected from a broad range, according to different requirements, such as pixel connectivity, symmetry or others (reviews in [Lam et al., 1992, Papari and Petkov, 2011]). The performance of these approaches is undermined by irregular shapes and/or intensity profiles that translate in missing or spurious gradient information, leading to over- or under-segmentation (Fig. 2.3). Nevertheless, this class of methods is still useful for simple and regular shapes, as in the case of the generalized Hough transform [Ballard, 1981] for circular/spherical object detection, successfully applied to 3D cell nuclei images in [Zanella et al., 2010]. Simpler approaches with lines (2D) and planes (3D) have also been used [Dzyubachyk et al., 2010].

Pixel Grouping

Instead of directly finding the ROI contours, it is also possible to segment sets of connected ROI pixels and then recover those located at the boundaries. This kind of approach is often used when the ROIs have homogeneous intensity profiles or present inner and outer boundaries (*e.g.* membranes with thickness greater than 1 pixel, see Fig. 2.3A/C). In such cases, the first step is to group pixels with similar intensity or texture patterns. The simplest approaches use threshold values to discard or select pixels (Fig. 2.4), which can be further

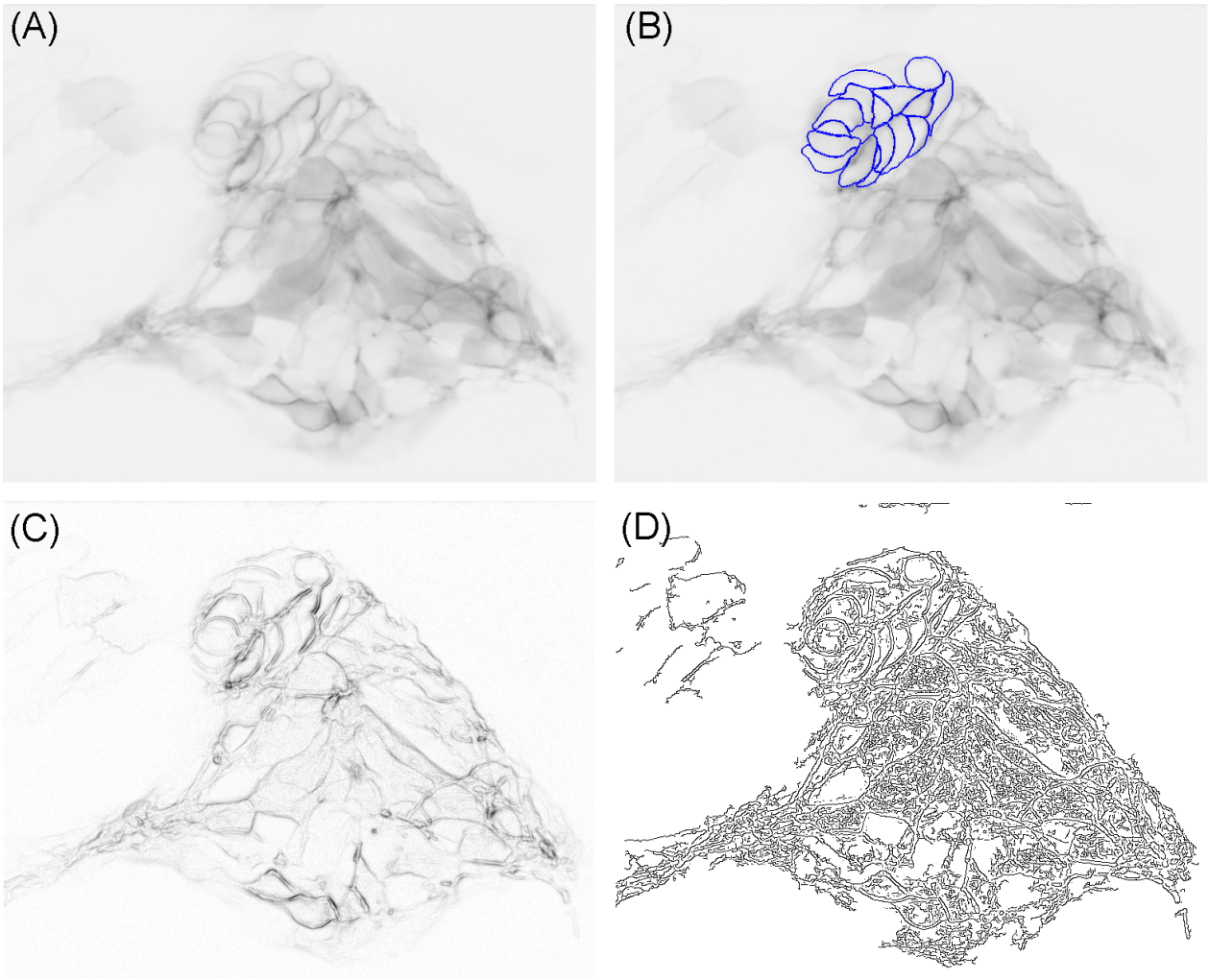

Figure 2.3: Classical edge detectors on a fluorescence microscopy image can be used to highlight pixels of high signal values located next to pixels of low signal values, providing a highly rough estimation of the PpO cell membranes from *in vivo* fluorescence imaging. **A:** 2D image slice from the sample stack of PpO cells in a zebrafish embryo with fluorescent membrane labeling (*flh*::GAP43-EGFP). The intensities are inverted in order to ease visualization. **B:** Manual outline (blue) of the cell membranes superposed to the image slice. **C:** Sobel edge detector applied to the image slice. **D:** Canny edge detector applied to the image slice.

filtered by applying similarity criteria for clustering (*e.g.* intensity variance [Otsu, 1979] or entropy [Kapur et al., 1985]). If needed, the obtained ROI boundaries can be smoothed by applying morphological operations (see examples in the books from [Gonzalez and Woods, 2007,Nixon and Aguado, 2008]). These approaches are mainly limited by the variability in the acquisition and sample labeling conditions that give images with poor and/or irregular ROI contrast (see example in Fig. 2.4, and [Dima et al., 2011] for evaluation on cells segmentation in fluorescence imaging). Nevertheless, they can be useful in images with a strong signal-to-noise ratio and/or when only a rough segmentation is required.

Watershed Methods

Watershed methods operate on binary images, defining and handling ROI adjacency lines by neighborhood criteria or chain codes at pixel level [Beucher and Lantuéjoul, 1979, Bertrand, 2005, Mashburn et al., 2012]. However, morphological characterization of the objects that require the length or the curvature of border segments lacks precision due to the discrete pixel representation. Watershed-smoothing (*e.g.* [Vachier and Meyer, 2005]) and posterior fine meshing [Veldhuis et al., 2017] methods have been proposed to improve the watershed quality and the subsequent membrane localization. In addition, membrane or edge enhancement filters are frequently applied in order to avoid under/oversegmentation by smoothing and connecting membranes previous to the watershed (*e.g.* [Stegmaier et al., 2016]).

Intensity Gradient Vector Fields

To improve the detection of ROIs with boundaries that can appear with low contrast, these approaches look for image zones with similar gradient orientations, in some cases filling missing information in weak boundary sections from their surroundings. The gradient vector flow models (GVF/GGVF) [Xu and Prince, 1997, Xu and Prince, 1998] define a field that optimizes two properties: alignment with the strong image gradient zones, and smoothness. From a convex integral optimization functional for the vector field, a system of partial differential equations (PDEs) is iteratively solved to compute the solution. Different weight functions have been used in order to provide robustness against image noise [Xu and Prince, 1997], enhance the strong gradient attraction [Xu and Prince, 1998], equalize weak signals [Li et al., 2005, Olmos, 2009], and/or to account for multi-channel images [Sapiro, 1997, Jaouen et al., 2014]. Once the vector field is obtained, an active contour model adjusts the ROI boundaries (see Fig. 2.8 and Section 3.2.1). Alternative approaches are the line segment detector (LSD) [von Gioi et al., 2012], which requires no input parameters but needs pronounced intensity gradients, and the Histogram of Oriented Gradients (HOG) [Ludwig et al., 2009] which performs angle binning with pixels of similar gradient orientation.

Morphometric Features

A more recent kind of approaches takes into account the characteristic morphology of membrane structures, stemming from previous works for vessel detection in medical imaging (since vessels and membranes can appear with the same shape in a 2D image). These approaches enhance and/or look for intensity distribution profiles of PSF-convolved membrane zones (Fig. 2.1D), using basic probe patterns of lines (rods), disks (balls) and planes, evaluating a fitness function for each pattern over image patches. For increased flexibility, a multi-scale strategy can be included to handle different membrane/image sizes (as in the case of

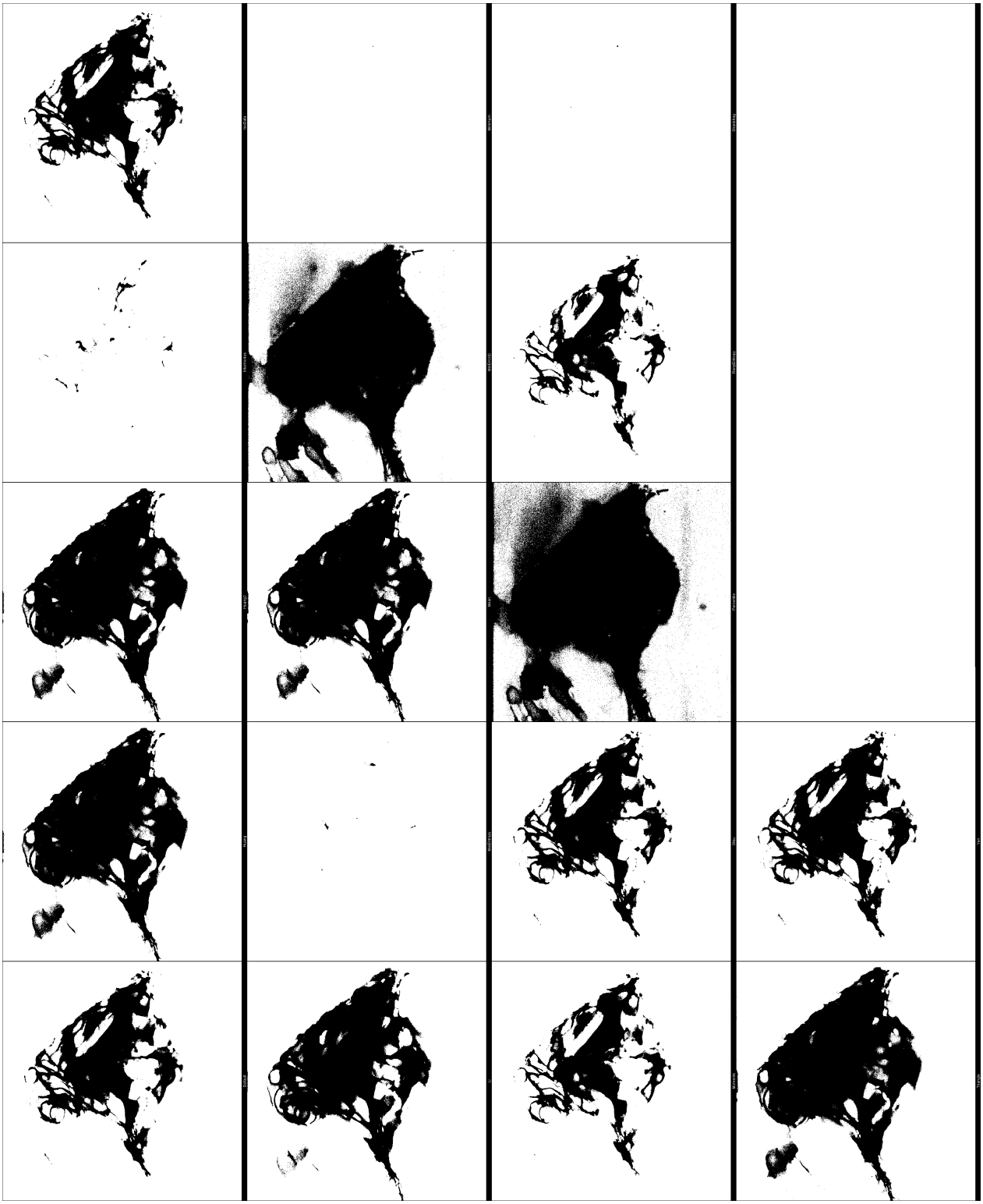

Figure 2.4: Segmentation by threshold is a simple but highly rough approach to detect PpO cell membrane signals *in vivo*, as for the image of Fig. 2.3, and, consequently, localize adjacent membranes. Available thresholding algorithms from FIJI software were used [Schindelin et al., 2012]. **First row**: Default (user set), Huang, Huang2, Intermodes, IsoData. **Second row**: Li, MaxEntropy, Mean, MinEntropy, Minimum. **Third row**: Moments, Otsu, Percentile, RenyiEntropy, Shanbhag. **Fourth row**: Triangle, Yen. Images are rotated 90° left.

ACME [Mosaliganti et al., 2012]). Within a given scale, these methods evaluate the intensity distribution using moments of inertia tensors (commonly used for mass distribution and principal component analysis, [Castañeda et al., 2014]). Hessian-based methods for vessel detection [Frangi et al., 1998, Obara et al., 2012] were first introduced and later extended to 3D fluorescence imaging with approaches like ACME [Mosaliganti et al., 2012] and voting schemes for estimating cell junctions [Michelin et al., 2014]. Examples are shown in Fig. 2.5.

Combined Approaches and Machine Learning

In addition to advances in each approach (reviews for microscopy imaging can be found in [Dima et al., 2011, Castañeda et al., 2014, Bhanu and Talbot, 2015]), the combination of methods often allows to overcome individual limitations and to provide flexibility for different scenarios. In practice, this comes at the cost of having multiple parameter settings and filter combinations to test before finding a proper processing workflow. From a more general perspective, the problem translates into having different selection methods and criteria for detecting points/regions of interest in a given data set, with a large space of feasible solutions from which an ideal or optimum setting has to be found. Machine learning approaches such as neural networks with deep learning [Schmidhuber, 2012, LeCun et al., 2015] have been applied to ease this task, with two main types: **unsupervised approaches** look for the best classification scheme according to given class separation criteria, while **supervised approaches** use a training set with segmentation examples given by the user (usually labeling of pixels), upon which a series of filters and feature descriptors are tried within a classification algorithm. In both cases, different filter/descriptor combinations are tried with different weighting and/or parameter values for classification, in order to find an optimal setting that yields the best segmentation according to a fitness criterion with respect to the training set. The obtained classification setting can then be applied to new image sets that have not been segmented by the user but are similar to the training set (*e.g.* with the same acquisition settings, ROI intensity profiles, etc.). Machine learning approaches have shown satisfactory performance in a number of applications within microscopy and biomedical imaging [Ching et al., 2018]. However, they still are unable to resolve membrane structures in live fluorescence imaging, due to the lack of higher-level descriptors to account for tissue/organ characteristics of specific scenarios, as in the case of the embryonic zebrafish PpO cells. Results from a trainable membrane segmentation approach upon a sample image are shown in Fig. 2.6.

The majority of the existing approaches are available in the form of software packages, both proprietary and open-source [Castañeda et al., 2014], designed for biomedical imaging [Sommer et al., 2011, Schindelin et al., 2012, de Chaumont et al., 2012] as well as for general purpose [Hall et al., 2009]. Such schemes can be applied to large image sets, significantly alleviating manual labor, but still requiring user inspection and corrections. As in the example from Fig. 2.6, the absence of shape or adjacency constraints results in missing/disconnected, or merged membrane sections; and the detection of individual cells cannot be achieved, which precludes the quantification of membrane geometry and physical properties (described in Section 1.3).

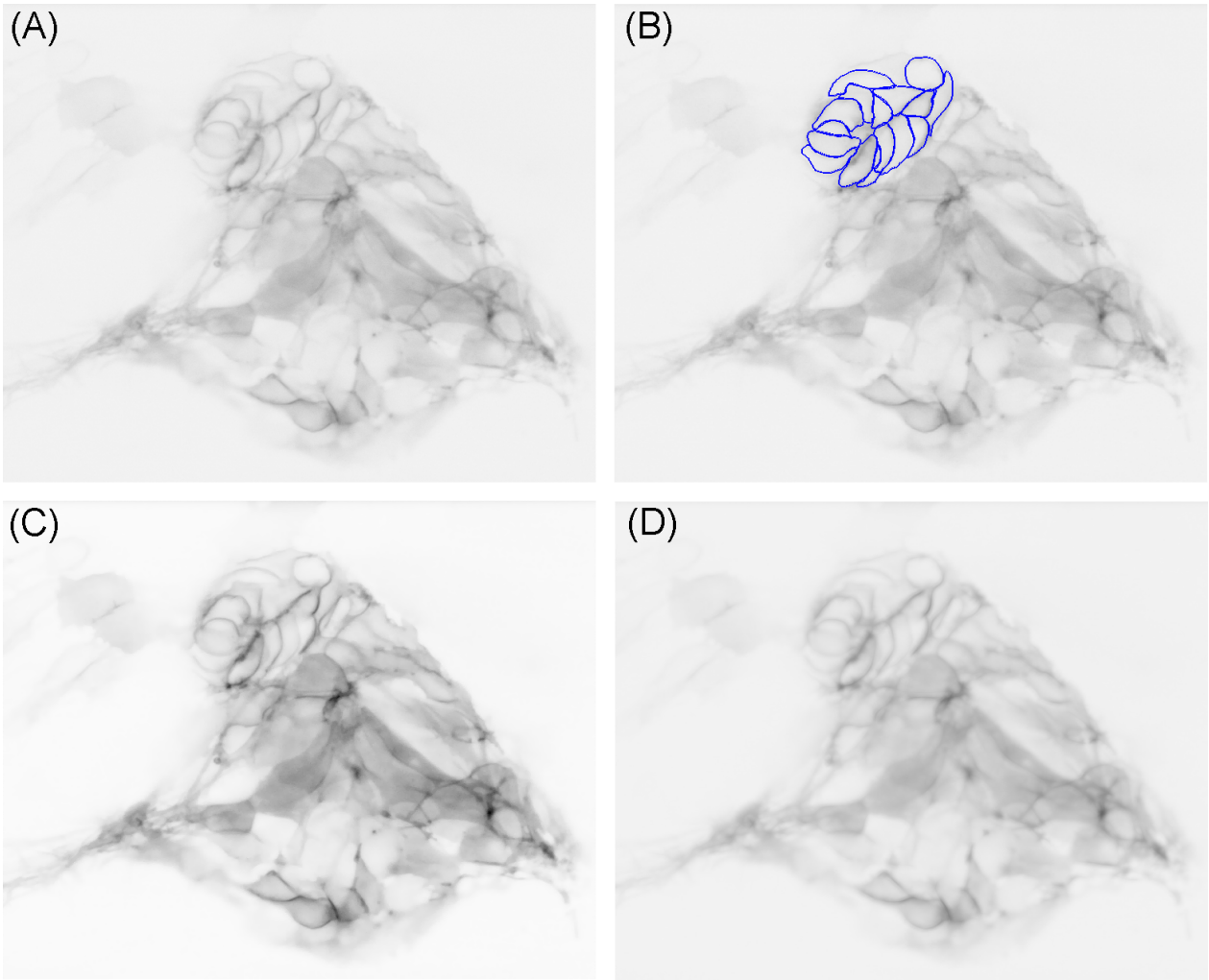

Figure 2.5: Anisotropic filtering over a fluorescence microscopy image can be used to improve signal quality of membrane structures. **A:** Original fluorescence microscopy image from Fig. 2.3. The intensities are inverted in order to ease visualization. **B:** Manual outline (blue) of the cell membranes superposed to the image slice. **C:** Perona-Malik filter, applied with $k = 10$, 100 iterations. (0 pixel side). **D:** Tubule enhancement filter, 7 pixels length.

Figure 2.6: Trained membrane segmentation example of fluorescent PpO cells. Upon the image of Fig. 2.3, a Random Forest trainable classifier was applied using a the Weka plug-in with FIJI software [Hall et al., 2009, Schindelin et al., 2012] (`http://fiji.sc/Trainable_Weka_Segmentation`).

Table 2.1: Handling of Adjacent Sections within different segmentation approaches (published in [Jara-Wilde et al., 2020]).

Approach	Handling of Adjacent Sections
Watershed [Bertrand, 2005, Beucher and Lantuéjoul, 1979]: Subdivides an image into a number of ROIs, following topographic profile transformations that generate digital elevation models on the basis of the image intensity pattern. The result are separated ROIs at pixel level.	+ Adjacency between objects can be defined and handled easily at pixel level. - ROIs defined at pixel level, border pixels must be defined by neighborhood criteria or chaincode algorithms. Limited morphological characterization.
Automated Cell Morphology Extractor, ACME (watershed based) [Mosaliganti et al., 2012, Frangi et al., 1998]: Principal directions of intensity variations from the image enhance membrane detection in zones with weak signal intensities of adjacent membranes, helping to reconstruct interfaces of adjacent cells.	+ Enhances weak membrane signals and applies morphological watershed. Multiscale approach. - No direct characterization of adjacent interface besides watershed. Robust morphological separation not ensured.
Real-time Accurate Cell-shape Extractor, RACE (watershed based) [Stegmaier et al., 2016, Vachier and Meyer, 2005]: 2D/3D cell shape characterization from membrane and nucleus segmentation similar to ACME. It uses morphological watershed with flooding of a viscous liquid.	+ Enhances the membrane signal and applies morphological viscous watershed, therefore getting a smoother solution for low resolution/information boundaries. - Same as ACME.
T-snakes (active contours) [McInerney and Terzopoulos, 1995b]: Grid-based model for contour merging/splitting. Grid recognizes collision between snakes.	+ Contours are either separated or fused, automatically discarding adjacency conflicts. - No adjacency definition to resolve a shared section between touching ROIs.
Active Contours without Edges (active contours) [Chan and Vese, 2001]: Curvature-driven contour evolution considering ROI interior properties. ROI boundary completion does not require strong intensity gradients.	+ Few parameters. - No intrinsic handling of overlapping sections. No intrinsic adjacency detection (reliant on the intensity gradient).
Subjective Surfaces (active contours) [Sarti et al., 2002]: Boundary completion with missing information. Contour perimeter minimization term allows for boundary completion in absence of strong gradients. Requires initialization from a point in the ROI interior.	Same as Chan and Vese.
3-D Active Meshes (active contours) [Dufour et al., 2011, Dufour et al., 2005]: Discrete variational energy optimization. Fast multiple coupled active contours with and without edges. More computationally costly than distance-based methods. Defines a repulsion term but without measuring the outcome.	+ Repulsion forces are exerted over overlapping contour sections. - Adjacency separation not guaranteed.
Advanced Level-Set-Based Cell Tracking (active contour-based) [Dzyubachyk et al., 2010]: Radon transform with active meshes. Separation planes are computed for touching ROIs with the Radon transform.	+ Separates adjacent cells using planes/lines (3D/2D). - Lacks expressive separation to account for adjacent membrane curvatures.
Deformable Model Array (other) [Namías et al., 2016]: Pipeline of deformable and non-deformable models. Cooperative multi-object 2D/3D segmentation.	+ *Ad-hoc* collision detection handling. - Not implemented. Algorithms for contour stop/rollback only.

2.2 Active Contour Models

Active contour models are optimization functions which impose constraints on the ROI boundaries, acting like deformation forces over a physical body: a balance equation is defined for desired properties, whose solution yields the optimum contour shape and placement on the image [Aubert and Kornprobst, 2006]. The constraint-based approach has made active contour models a broadly used technique for segmentation because of its great adaptability to detect different shapes and to encompass high-level morphological properties. Upon these, techniques for contour modeling and numerical solutions have been developed for fast computation, improved flexibility or robustness, and handling issues regarding contour morphology, initialization, and parameter sensitivity, among others.

Active contours can be described as adjustable ROI boundaries (curves in 2D, surfaces in 3D) subject to constraints of object morphology and image features which deform them until reaching an equilibrium state. They are regarded as a type of deformable model[2], stemming from the idea of physical bodies deformed by the action of forces towards a state of minimal energy. The contours are typically represented by parametric or implicit functions, for which the constraints and the optimum are defined with integral functionals and/or PDEs approaches (in-depth descriptions can be found in [Aubert and Kornprobst, 2006, Osher and Paragios, 2003]). The first active contour model for image segmentation is known is the *snake* [Kass et al., 1988]: a parametric 2D curve is iteratively deformed over the input image until it converges to its equilibrium state, given by the solution of a PDE system that minimizes an integral energy functional. In the snake model, the optimality condition for minimal energy is achieved by the solution of a PDE system known as the Euler-Lagrange equations, which is analogous to the physical phenomena of energy minimization (integral functional) through *force balance* equations (PDE system); each energy term of the optimization functional is related to a feature or constraint that the optimal contours must satisfy. The inclusion of a time derivative yields an iterative solution (see Figs. 2.7 and 2.8, and Section 3.2.2 for details in the parametric contour model). Most of the posterior active contour models developed follow this scheme, either by constructing a force balance system or defining a minimal energy functional (or both). The following main types of forces are distinguished for active contours:

- The **internal forces** are properties intrinsic to the contours, such as smoothness, curvature, inflection points, or size, defined by respective terms in the minimization model. These properties do not restrict a particular contour morphology, yielding high flexibility for a broad variety of forms.
- The **external forces** correspond to image features that need to be maintained by the contours (like intensity gradients) while satisfying the constraints of the internal forces (see section 2.1). In addition, *ad-hoc* interest points or regions can be defined to attract or repulse contours from them (for example the "spring" and "volcano" forces from the original snakes model [Kass et al., 1988]).
- Other forces can be distinguished for parametric and implicit models, aimed to address issues like local optima, weak object boundaries or low capture range for distant objects. Some of these forces are not included in the analytic optimization functionals, but are included in the PDE numerical model and/or as intermediate steps between iterations:

[2]However, "active contours" and "deformable models" can be found as synonyms in the literature.

– contour-region interaction forces that depend on specific contour features and placement during adjustment, like the "balloon force" [Cohen, 1991], the "geometric potential field" [Yeo et al., 2011], or the variable force for contour regularity versus image features in the subjective contour model [Sarti et al., 2000, Sarti et al., 2002];
– parametric contours with merging/splitting criteria, by checking for ROI-ROI intersections and single-ROI continuity between iterations, in the topologically adaptive snakes [McInerney and Terzopoulos, 1995b] and its 3D extension to surfaces [McInerney and Terzopoulos, 1999].

Regarding the representation of the contour function, two main approaches have been described: the explicit (parametric) and the implicit models. Each approach requires different numerical-computational methods for solving the contour adjustment, as described in the remainder of this section. It is worth mentioning that in some cases it is possible to derive equivalent parametric and implicit models from a common optimization functional (*e.g.* [Xu et al., 2000, Sapiro, 2001, Aubert and Kornprobst, 2006]).

2.2.1 Parametric Models

The snake method from Kass *et al.* is a typical example of a parametric model: a set of geometric elements, such as line segments (2D) or surface mesh triangles (3D), defines a parametric function for each ROI boundary, suitable for calculating morphology-related properties such as contour size or curvature. An iterative scheme for the force balance is applied to each parametric function until convergence. Fig. 2.7 shows an example of parametric active contours for segmentation and contour description of microscopic structures in a 2D image. The coefficients α and β weight internal forces known as elasticity and rigidity, respectively. The elasticity acts as a contraction force, while the rigidity controls the degree of bending for the contour. The additional force coefficients κ and q weight image forces, and γ is an artificial viscosity coefficient that regulates the contour response to the other forces.

Parametric formulations require control methods over the contour sampling (such as interpolation or mesh refinement), mainly due to the placement of contour elements after each deformation step which can lead to numerical instabilities. Also, special handling for topology changes is needed (contour splitting, merging or collapsing) when the number of initial ROIs is not the same in the optimal segmentation, or bad initialization scenarios yield local optima with a correct number of ROIs. Proposed approaches for handling this kind of scenarios include contour interpolation [Williams and Shah, 1992, Fanani et al., 2010] and grid data structures for intersection detection and topology tracking [McInerney and Terzopoulos, 1995b, McInerney and Terzopoulos, 1999]. A drawback for parametric contour functionals is that conditions for global optimum and convexity are not fully guaranteed (see [Aubert and Kornprobst, 2006] for the snakes functional), making it necessary to use supporting techniques in order to avoid local minima (for example, the balloon forces of [Cohen, 1991]). Nevertheless, parametric models are easy to understand and implement in comparison with implicit approaches, and the contour model allows flexibility for user interactivity (see for example the "volcano" and "spring" forces in the original snake model). Another advantage of the parametric modeling of ROI boundaries is that they allow the direct computation of morpho-topology properties such as volume, surface area, perimeter, etc.

Following the snake method, other parametric models were developed to extend its functionality and improve convergence issues: a 3D parametric model for surfaces was presented in [Cohen et al., 1992]. Xu & Prince introduced an image force model based on diffusion equations to extend the capture range of the intensity gradients over the image [Xu and Prince, 1997, Xu and Prince, 1998]. The *active shape* models restrict the ROI morphology to given shape templates, using landmark points that represent features of interest [Cootes et al., 1995]. A classification between boundary-based and region-based active contours is also used for models based on other ROI properties, such as color/intensity homogeneity, size, etc. The well-known model of active contours without edges [Chan and Vese, 2001] is a typical example of region-based contours, although it is defined as an implicit method. The *active polygons* model [Unal et al., 2005] uses information entropy measurements for image textures as properties to detect the interior of ROIs, in addition to boundary properties.

Computational Complexity

Computational solving methods for parametric models must perform: (i) pre-processing or filtering of the original image to obtain a feature or edge map that as the external force, and (ii) evolution of the ROI boundaries from its initial state to a relaxed state, according to the corresponding iterative scheme with internal and external forces. In this context, the computations of internal forces depend intrinsically on the parametrization of the boundary, being expressed as PDEs, for which derivatives are approximated using spatial neighborhoods for each boundary element. The overall complexity of the computation process is the sum of the complexities for the computation of the external (image) force and the iterative scheme for the contour: for a 3D image with $s_x \times s_y \times s_z$ pixels and a single contour with n elements, the first term requires space and computation time of $O(s_x s_y s_z)$ (i.e. directly proportional to the number of image pixels); for the second term, the iterative scheme can be solved at each iteration by *ad-hoc* strategies whose computation uses $O(n)$ memory space and time when the derivative computations are $O(1)$, or by algebraic solvers ranging from $O(n^3)$ for classic L/U matrix decompositions to $O(n)$ for multigrid methods. It also should be taken into account that re-parametrization of the contour may be necessary, adding $O(n)$ complexity for typical cases. The use of additional topology control strategies like grids for t-snakes approaches or similar involves additional complexity to the defining bound of $O(s_x s_y s_z) + O(n)$.

Upon parametric contour models, morphological properties intrinsic to each ROI can be computed directly: given a 2D polygon or a 3D surface mesh, computations of surface area, perimeter, volume, curvature, etc. can be performed using the same data structure, most of them in $O(n)$ time. Mass distribution computations can involve additional processes for computing interior volume elements. Also, the parametric contour models need dedicated data structures for distance computations (such as bounding volume hierarchies, space partitioning or level set functions) in order to compute efficiently these kinds of properties, especially for highly complex object shapes which otherwise require much more distance computations (see the additional computation approaches in the following subsection and in 2.3).

Parametric curve:

$$C = C(s,t) = [x(t), y(t)]$$

Force balance:

$$\gamma \frac{\partial C}{\partial t} = \underbrace{\beta \frac{\partial^4 C}{\partial s^4} - \alpha \frac{\partial^2 C}{\partial s^2}}_{\text{internal forces}} + \underbrace{f_{img}(C)}_{\text{image forces}}$$

Force parameters:

α elasticity
β bending
γ viscosity

- Bending

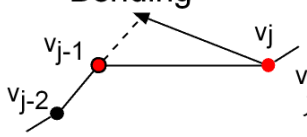

- Elasticity

- $k \cdot V(C)$ GVF field $V(C)$
- $q \cdot B(C)$ Balloon force $B(C)$

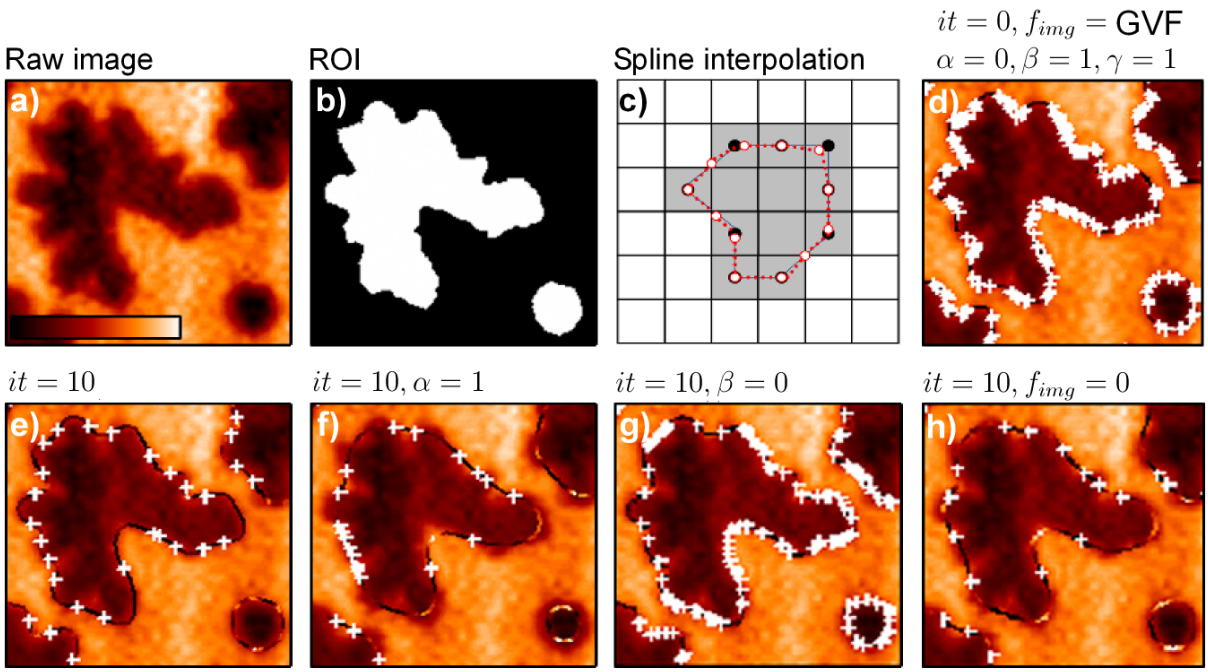

Figure 2.7: 2D Parametric Active Contours ("snakes") in a microscopy image of lipid monolayers. **a**: Sample image of ceramide-enriched lipid domains using a pseudo-color scale (see bar). **b**: Threshold segmentation of the lipid domains as ROIs. **c**: Spline interpolated snakes, redistributing non-equidistant contour points (black) to equidistant interpolated points (white). **d-h**: Optimization of domain morphologies using the snakes model with different settings. Initial contours (0 iterations, $it = 0$) are shown together with the indicated force parameters. Contours are drawn with pseudo-color from low to high curvature values. White crosses mark inflection points. **e**: Snakes at 10 iterations ($it = 10$) with the settings of d. **f-h**: Snakes after 10 iterations with high elastic force coefficient ($\alpha = 1$, e), without bending force ($\beta = 0$, g), and without image forces ($f_{img} = 0$, h). All other force parameters values were set as in d. Published in [Fanani et al., 2010].

2.2.2 Implicit Models

Based on the Level Sets Method (LSM) [Osher and Sethian, 1988], implicit models embed the deforming contours into a higher dimension function that serves as the level set function, which includes the same (or equivalent) external and internal forces for the contour adjustment. The level set function is deformed according to a system of PDEs or equivalent discrete model [Aubert and Kornprobst, 2006, Hagan and Zhao, 2009] until convergence, and the resulting parametric ROI boundaries are recovered in a post-processing step. As an example, Fig. 2.8 shows an implicit active contour model for segmenting cell membranes in a microscopy image of a zebrafish embryo: given an initial contour (a circle), the level set function evolves until its zero-level set (final contour, upper right image) is placed upon the intensity gradient zones corresponding to the cell membrane. Implicit models can intrinsically handle topological contour changes such as merging or splitting for several ROIs without any special consideration for their implementation, thus being more robust with respect to the initialization, but requiring a separate processing step in order to reconstruct the resulting ROIs, impeding direct access for ROI properties like contour perimeter or surface area. The LSM models how a front propagates depending on its curvature along its normal direction (inwards, outwards or both), which makes it suitable for fluid dynamics and other physics models[3]. LSM-based models have been introduced for detecting ROIs in images of weak/missing intensity gradients [Chan and Vese, 2001, Sarti et al., 2000], non-homogeneous gradients/region interiors, and noise [Chan and Vese, 2001, Yeo et al., 2011]. LSM has also been used for image denoising, curvature-driven shape deformation, computer graphics, and robot navigation systems [Houston et al., 2006, Osher and Paragios, 2003, Sethian, 2010].

Computational Complexity

Solving the LSM equation requires the level set function to be computed for the whole image. For an image with $s_x \times s_y \times s_z$ pixels, the computational complexity depends (in space and time) on the PDE solver used for the equation. If the derivative computation can be performed in time $O(1)$ per image pixel, the complexity ranges from $O((s_x s_y s_z)^3)$ for matrix factorization to $O(s_x s_y s_z)$ for multigrid methods[4]. This is the case for the basic or naive LSM implementation, upon which different optimizations have been developed: the *narrow band* level sets [Adalsteinsson and Sethian, 1995] perform the computations only for the zero-level sets and small neighboring sections within the image (hence the name). Further optimizations address data structures for the iterative scheme: linked lists for storing and updating the level sets [Whitaker, 1998], fast distance computations by relying on octrees [Losasso et al., 2004] and other space partitioning techniques [Bridson, 2003, Chiang et al., 1998], and compressed data structures for the level set functions such as the dynamic tubular grid [Nielsen and Museth, 2006] or the hierarchical run-length encoded level sets [Houston et al., 2006].

The computation of external image forces must be added to the overall complexity in the same way as for parametric models, since edge maps or similar functions need to be computed over the entire image, typically adding $O(s_x s_y s_z)$ space and time. Most of the image filtering techniques perform similarly, with computations commonly bounded by a fixed amount of operations for each image pixel (even for more complex approaches such as the gradient

[3]The LSM equation corresponds to the Hamilton-Jacobi equation, well known in mathematics and physics.

[4]Computation speedups can be obtained at this and other stages by concurrent processing techniques whose review is outside the scope of the present work.

Level set function:

$$\phi = \phi(x, y, t)$$

Contour function:

$$C = C_0(t) = \{\phi(x, y, t) \mid \phi = 0\}$$

Force parameters:

$$\kappa = div\left(\frac{\nabla \phi}{|\nabla \phi|}\right) : \text{curvature}$$

α: curvature threshold

Evolution scheme:

$$\frac{\partial \phi}{\partial t} = \underbrace{g\left(|\nabla I|\right)}_{\text{edge term}} \underbrace{(\kappa + \alpha)|\nabla \phi|}_{\text{curvature-based speed term}} + \underbrace{\nabla g \cdot \nabla \phi}_{\text{speed control term for edge zones}}$$

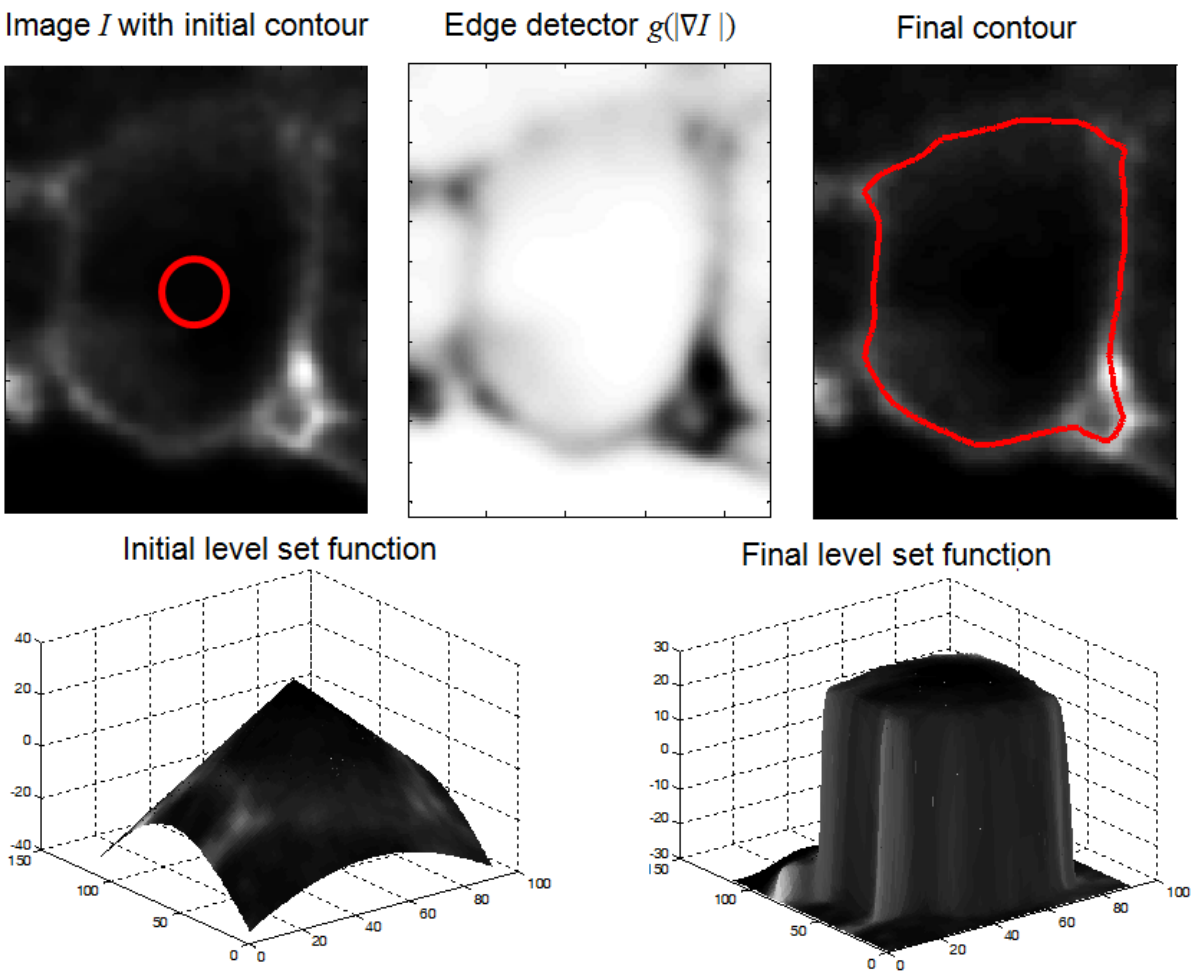

Figure 2.8: 2D implicit active contours in a microscopy image of a zebrafish embryo. The image I shows the fluorescence membrane intensity of a dorsal forerunner cell during the formation of a cell complex known as the Kupffer's vesicle in a zebrafish embryo. Upon I, an edge detector function $g(|\nabla I|)$ is computed, which acts as a stopping term for the level set function evolution. Image courtesy of E. Pulgar (Laboratory of Experimental Ontogeny, U. of Chile). Segmentation performed using the available implementation of the Subjective Surface approach [Sarti et al., 2002, Zanella et al., 2010].

vector flow fields [Xu and Prince, 1997, Xu and Prince, 1998]). Alternative approaches have been used to harness parallel computing architectures, by using formulations equivalent to the LSM, such as Lattice-Boltzmann cellular automata [Hagan and Zhao, 2009].

Implicit models require a dedicated processing step to produce a parametric boundary model suitable for morpho-topological analysis. This can adds significant time and space requirements, depending on the data structure used for the level set function. In turn, implicit models can be used as auxiliary distance maps for fast computations in inter-object topological description scenarios, like lattice formation in molecular films [de Tullio et al., 2007, Fanani et al., 2010], shape patterns in multi-cellular complexes, and shared surface for cell-cell interaction [Sherrard et al., 2010].

2.3 Multiple-Object Segmentation

In biomedical applications, active contour models have been extensively used since their introduction [McInerney and Terzopoulos, 1995b]. Pattern recognition techniques have been used in the form of supervised approaches with prior knowledge [Abufadel et al., 2008], as well as combined with boundary completion techniques [Sarti et al., 2000, Michelin et al., 2014]. In medical imaging, several applications for MRI data in joints and organs like brain and heart have been reported [McInerney and Terzopoulos, 1996, Pham et al., 2000, Zhao and Xie, 2013]. Temporal criteria for 3D segmentation has been included in the so-called 4D segmentation, applied for both research [Mischler et al., 2006, Bourgine et al., 2010, Mikula et al., 2011] and medical imaging [McInerney and Terzopoulos, 1995a, Montagnat and Delingette, 2005, Jaouen et al., 2014]. For time-lapse fluorescence microscopy of living cells, Melani *et al.* combined motion estimation with level sets segmentation, in order to identify and describe structural changes in embryonic brain cells of zebrafish [Melani et al., 2007]. In [Zanella et al., 2010], a variation of the subjective surfaces method [Sarti et al., 2000, Sarti et al., 2002] was used to segment cell membranes in 3D confocal image stacks. In order to properly initialize the subjective surface method, ellipsoidal template matching was used to detect cell nuclei (one inside each cell membrane, excepting special cases such as cell divisions).

When it comes to physical contact between cell membranes, the adjacency of neighboring membrane contours needs to be detected and quantified. This task is subject of ongoing research [Dufour et al., 2017], yet the segmentation of adjacent membranes in cell aggregates such as multicellular samples, tissue, organs, or whole organisms from fluorescence microscopy images remains a challenging task. Table 2.1 presents an overview of the main approaches reviewed. Other approaches applied to fluorescence microscopy have been presented for handling occlusions in 2D [Bergeest and Rohr, 2012], and resolving contiguous ROIs in medical images from CT or MRI [Chan and Vese, 2001, Lucas et al., 2012, Bogovic et al., 2013]. High-throughput and *in toto* imaging have been recently addressed, for nuclei segmentation and tracking, and taking into account fast computation schemes such as parallel processing [Keller, 2013, Mikula et al., 2012]. So far, only an implicit approach for multiple objects [Bogovic et al., 2013] yields a contact-preserving segmentation, but depending on the strength of ROI boundary (intensity gradient) or interior (intensity homogeneity) features. In this case, direct access to ROI morphology depends on constructing an additional model of the ROIs, either adding computation times to the segmentation or requiring post-processing to detect and correct possible errors. The "active meshes" approach [Dufour et al., 2011]

has been used in ROIs with homogeneous interior labeling, penalizing the overlap between ROIs that may occur since the deformation of each ROI is computed without explicit contact rules, either due to the adjustment itself or by moving/deforming each ROI when using motion estimation in time series (as initialization to further adjustment steps). Hence, contact becomes an indirect constraint in the final segmentation, with no quantitative guarantee or measurement for parameter estimations. Simpler approaches such as computing straight lines (planes in 3D) have also been proposed [Dzyubachyk et al., 2010].

More recent approaches on shared boundaries for membrane segmentation [Mosaliganti et al., 2012, Michelin et al., 2014] address multiple-object junction points by membrane-enhancement image filters, but without ROI boundary models, and rely on basic approaches such as watershed methods or circular shape detection [Stegmaier et al., 2016, Chang et al., 2015]. Some authors even suggested the need for a dedicated approach, such as the proposed in this work. A similar work on parametric contours reaches the adjacency detection, but no action is taken besides stopping the contour evolution [Namías et al., 2016] (see also 4.4). Interpolation techniques have also been used to improve upon roughly segmented ROIs, for detecting junction points and estimating interaction forces [Brodland et al., 2014, Veldhuis et al., 2017], and 2D lattices of convex polygons have been used for dense epithelia [Farrell et al., 2017].

Computational Complexity

Adjustment approaches for multiple adjacent ROIs add distance and intersection computations that require a significant number of floating-point operations which are individually slow to perform.The problem has been addressed in separate tasks:

1. **Calculating the distance between two ROIs,** i **and** j. It becomes an $O(D(\mathrm{i}, j)) = O(n_{\mathrm{i}} + n_j)$ operation for implicit models, since they are implemented by computing distance functions (level sets) which are directly accessible, and for each element of one ROI, the distance from the other is accessible in $O(1)$ operations. Parametric models such as polygons or spline curves require calculating distances between all the possible pairs of elements from each ROI. It becomes an $O(D(\mathrm{i}, j)) = O(n_{\mathrm{i}} \times n_j$ operation, where n_{i} and n_j are the number of elements of the ROIs i and j, respectively. A reduction in the number of operations can be attained if the elements of the ROIs are sorted or indexed (see item 3 below).
2. **Determining the intersection of two ROIs**. To date, implicit approaches do not require computing ROI-ROI intersections. MGDM and Active Meshes define repulsive forces over each element of overlapping ROIs (with the overlap determined from their respective level sets). Parametric approaches such as the T-snakes [McInerney and Terzopoulos, 1995b] project the ROI boundaries to a grid which is checked in a given sequence. The Active Meshes hybrid model [Dufour et al., 2011] detects intersecting ROI elements by using a parametric data structure (surface mesh).
3. **Efficiently computing distance and intersection for multiple ROIs**. A broad spectrum of *collision detection* approaches (see surveys in [Lin and Gottschalk, 1998, Teschner et al., 2005, Kockara et al., 2007]) has been developed in past years, and some of them have been combined with parametric models as noted below. For a set of N ROIs, two main scenarios can be defined for both parametric and implicit models:

(a) In absence of auxiliary information, each ROI needs to be checked against the other $N-1$ ROIs for adjacency/intersection (worst-case scenario), which adds up to $O(N^2)$ detailed calculations $D(\mathrm{i}, j)$ over the entire set.

(b) If the set is spatially sorted or indexed, the number of detailed calculations can be reduced to a subset of ROIs within a threshold distance, or only the ROIs adjacent in the sorted set [Lin and Gottschalk, 1998, Teschner et al., 2005]. Sorting algorithms like Sweep-and-Prune [Cohen et al., 1995] are common choices, but also space partitioning structures such as quadtrees/octrees (2D/3D) [Finkel and Bentley, 1974] and k-d trees (non-overlapping) [Bentley, 1975], or R* trees (overlapping) [Beckmann et al., 1990] can be used. Reductions to $O(N \log_2 N)$ detailed calculations are expected. Further reductions can be obtained with the addition of:

- simpler bounding shapes such as rectangles, circles or convex polygons that can be computed for each ROI, in order to simplify distance calculations during the sorting step and avoid complex calculations of non-adjacent ROIs [Lin and Gottschalk, 1998]; and
- data structures for spatial indexing/sorting of subsets of ROI elements can reduce the number of operations to determine adjacency or intersection.

When the complexity in determining adjacency becomes constant ($O(1)$), and the spatial indexing/sorting is used, a lower bound can be defined for the total number of operations in determining adjacency. Let $\overline{g}$ the average number of neighbors for any ROI in the set, the total number of operations for checking the N ROIs becomes $O(N \log_2 \overline{g})$, with an additional number of $O(N \log_2 N)$ operations required for pre-processing.

Chapter 3

ALPACA: ALgorithm for Piecewise Adjacent Contour Adjustment

3.1 Overview

Active contours allow the segmentation of ROIs with possibly different shapes and/or sizes, but sharing common properties related to their geometry, which condition their adjustment over a given image. However, for multiple adjacent objects such as compact membrane aggregates with touching boundaries, object-to-object interaction becomes an important morphological feature that needs to be taken into account for accurate segmentation and quantification. As discussed previously, a proper scheme for shared boundary adjustment and quantification has been unaddressed, motivating the present work. Hence, the ALPACA approach is proposed: first, adjacent sections are detected for ROI contour sections that either overlap or lie within a proximity threshold; then, shared sections are calculated pairwise for ROIs with adjacent sections; finally, an piecewise contour reconstruction takes place connect shared (or adjacent) and non-shared (or non-adjacent) sections. An example of the detection of adjacent sections in PpO cell membranes is shown in Fig. 3.1.

This chapter starts with the depiction of the main algorithm (Fig. 3.2), together with the description of required inputs, produced outputs. Next (3.2), algorithm step descriptions are presented, followed by implementation details (3.3) and optimizations (3.4). Last, a computational complexity analysis is presented (3.5).

3.1.1 Input Parameters

- Fluorescent intensity Image $I(x, y)$.
- Generalized Gradient Vector Flow field $GGVF(I(x, y)) = [u(x, y), v(x, y)]$ (optional).
- Adjacency Distance threshold d set by an expert considering the spatial resolution limit of the specific microscopic setting and the image quality.
- Set of parametric contours $C_{\mathrm{i}}(x, y)$ from an active contour approach (see [Kass et al., 1988,Fanani et al., 2010], 3.2.2), optimized to represent the morphology of the subjacent ROIs by a ground truth (if available) or by an expert. The contours can be obtained on

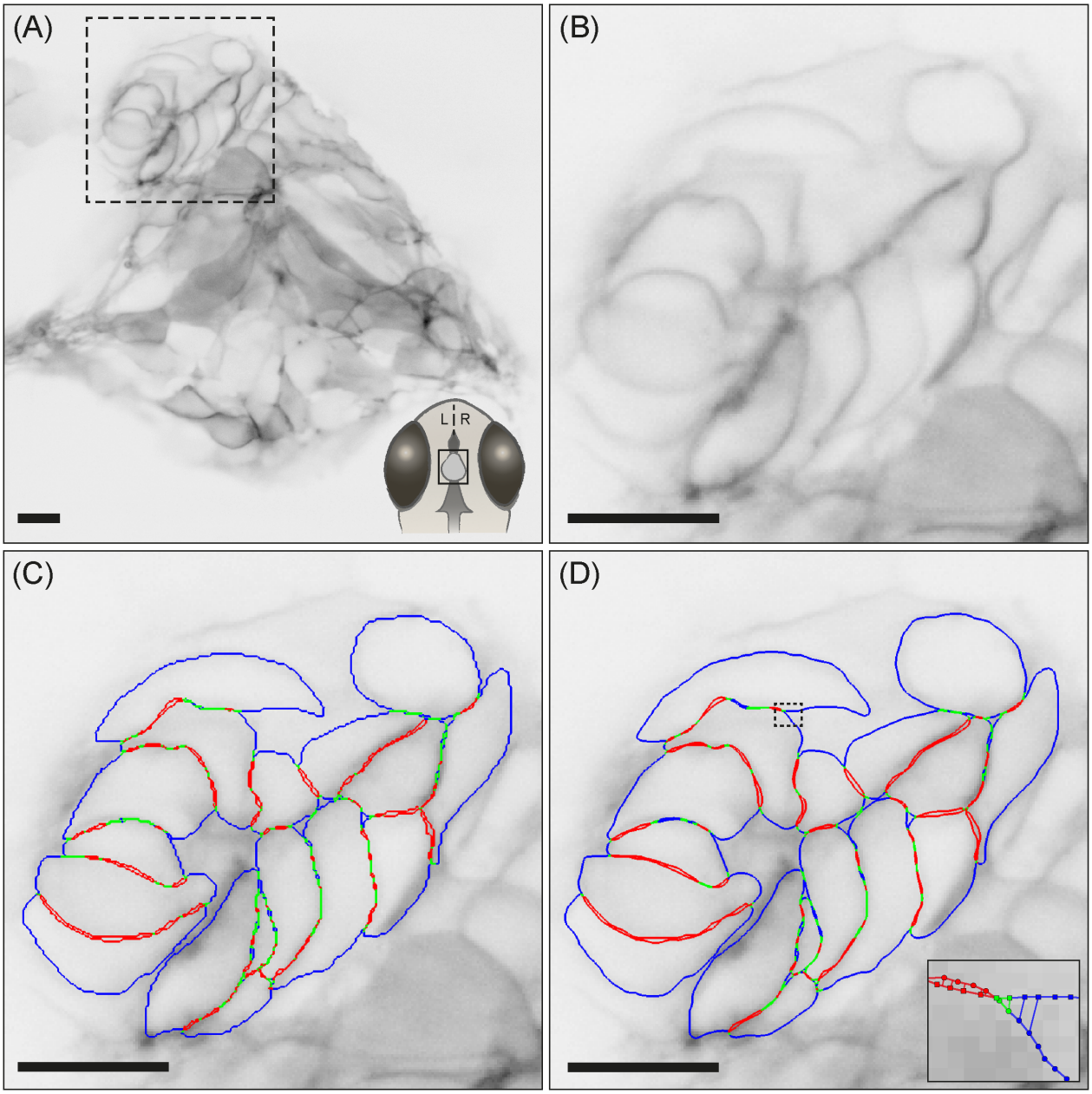

Figure 3.1: Membrane segmentation and definition of overlapping, adjacent and non-adjacent contour sections in neighboring cells. Spinning-disk microscopy image of cell membranes of the pineal complex of a zebrafish (*Danio rerio*) *flh*::GAP43-EGFP transgenic embryo at 38 hours post fertilization. Fluorescence intensities are shown as inverted grey-scale in all panels. **A**: 2D slice taken from a 3D stack (69 slices with 500 nm z-spacing, z position $32 \times 0.5\,\mu\text{m} = 16\,\mu\text{m}$). Bottom right: scheme of the embryo head with the Left-Right (L-R) orientation and the pineal complex marked by a black square. **B**: Detail of the fluorescence intensities of PpO cell membranes (from the dashed red square in A). **C-D**: Manually Outlined Contours (C) and optimized parametric active contours (D) with color coded for overlapping (red), adjacent (green) and non-adjacent (blue) contour sections, defined by an Adjacency Distance $d = 86\,\text{nm}$. The insert in D shows the shortest segment-segment distance from neighboring contours from the dashed rectangle (see section 3.2.4). Scale bars in A/B: $\sim$10 µm, insert (D): $\sim$332 nm. Published in [Jara-Wilde et al., 2020]

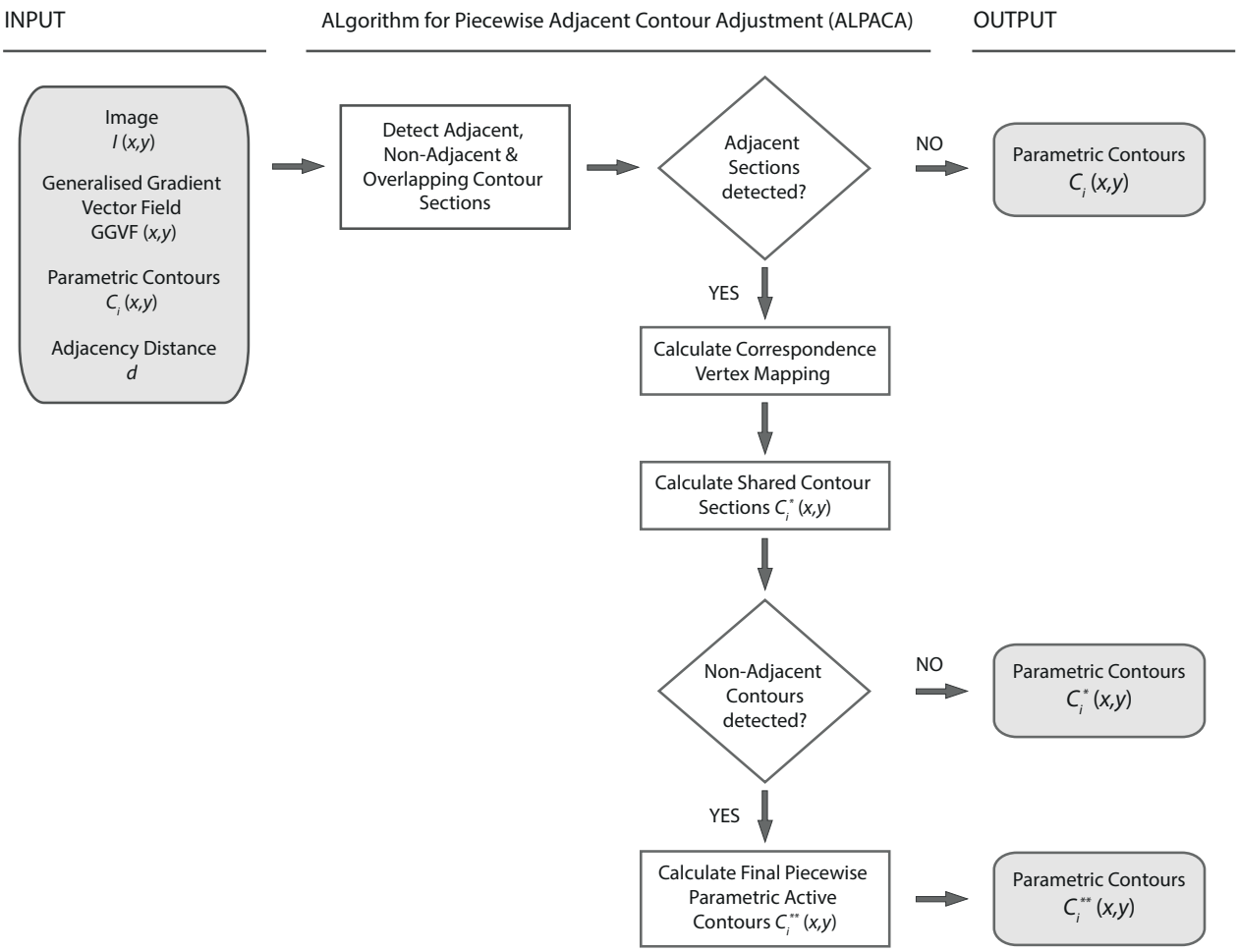

Figure 3.2: Flowchart - ALgorithm for Piecewise Adjacent Contour Adjustment ALPACA.

the basis of either automatic or manual segmentation (see [Härtel et al., 2007, Fanani et al., 2010], Fig. 3.1C/D) and also, with methods alternative to active contours.

On the basis of the set of $C_{\mathrm{i}}(x, y)$ and d, ALPACA calculates the distance between neighboring contour sections based on the Segment-Segment Distance, and classifies non-adjacent, adjacent, and overlapping contour sections (see 3.2.3 and Fig. 3.1C/D). If no adjacent or overlapping sections exist for a given contour $C_{\mathrm{i}}(x, y)$, it is returned with no changes as output. If adjacent or overlapping sections do exist, a calculation of a correspondence vertex mapping based on normalized lengths is performed (see 3.2.4) and Shared Contour Sections are calculated by averaging the (x, y) positions of corresponding vertices. Next, the algorithm checks if non-adjacent contour sections exist (a ROI might consist of adjacent contour sections only). If not, a contour formed by shared sections $C_{\mathrm{i}}^{*}(x, y)$ is output returned. If non-adjacent contour sections do exist, Piecewise Parametric Contours $C_{\mathrm{i}}^{**}(x, y)$ are calculated to connect non-adjacent and shared sections. For the data presented in this thesis, vertices of the shared sections were fixed, and non-adjacent sections readjusted under the initial active contours constraints that respect morphological features of the subjacent ROIs (see 4.1.1, Fig. 3.7G/H). The use of GGVF is optional, and was not applied for the final relaxation in our examples. Finally, $C_{\mathrm{i}}^{**}(x, y)$ are returned for further analysis.

In summary, ALPACA returns one of three possible outputs:

- Parametric Contours $C_{\mathrm{i}}(x, y)$ without adjacent sections.
- Parametric Contours $C_{\mathrm{i}}^{*}(x, y)$ where all sections fulfill the adjacency criteria.
- Piecewise Parametric Contours $C_{\mathrm{i}}^{**}(x, y)$ with sections that fulfill the adjacency criteria and sections that do not.

The artifact of overlapping sections is corrected in $C_{\mathrm{i}}^{*}(x, y)$ and $C_{\mathrm{i}}^{**}(x, y)$, and the results fit the morphological constraints of the microscopic sample.

The main algorithm is depicted in Fig. 3.2. It comprises two main stages:

1. Detection and adjustment of **shared** contour sections, defined by two or more ROIs that overlap or lie within the Adjacency Distance d.
2. Adjustment of **non-adjacent** contour sections, or entire ROI contours with no influence of any adjacent ROI.

3.2 Algorithm Steps

3.2.1 Gradient Vector Flow Image Force Computation

The basic image force field implemented is the intensity gradient, $\nabla I = \nabla I(x, y) = [I_x, I_y]$, which is a vector field that points in the direction of the highest intensity change at each image pixel. Using forward finite differences, it is computed at each pixel position $[\mathrm{i}, j]$:

$$I_x[\mathrm{i}, j] = I[\mathrm{i}+1, j] - I[\mathrm{i}, j] \tag{3.1}$$

$$I_y[\mathrm{i}, j] = I[\mathrm{i}, j+1] - I[\mathrm{i}, j] \tag{3.2}$$

A general description and implementation of intensity gradients in digital images can be found in the works of [Marr, 1982, Spontón and Cardelino, 2015]. In the case of fluorescence microscopy imaging, the implementation and comparison of different numerical schemes for motion estimation with optical flow algorithms were addressed [Delpiano et al., 2012, Jara-Wilde et al., 2015].

To regularize the fluorescence intensity gradients, Gradient Vector Flow approaches (GVF, and its generalized model GGVF) [Xu and Prince, 1997, Xu and Prince, 1998] were implemented. Here, the image gradient ∇I is taken as a starting solution for an advection/diffusion equation which is defined to produce a smooth vector field oriented towards image zones with the highest gradient magnitude. Fig. 3.4 show the resulting GGVF field for fluorescent cell membranes acquired with *in vivo* microscopy imaging.

The vector field $V = V(x, y) = [u(x, y), v(x, y)]$ is computed by an iterative scheme, by making $V = [u(x, y, t), v(x, y, t)]$ and solving the following equation:

$$V_t = g(\nabla I)\nabla^2 V - h(\nabla I)(V - \nabla I) \tag{3.3}$$

$g(\nabla I) = 1 - h(\nabla I)$ is an edge indicator function, with $g(\nabla I) \to 1$ in low or null gradient zones, and $g(\nabla I) \to 0$ in high-gradient zones. A negative exponential function was used, as

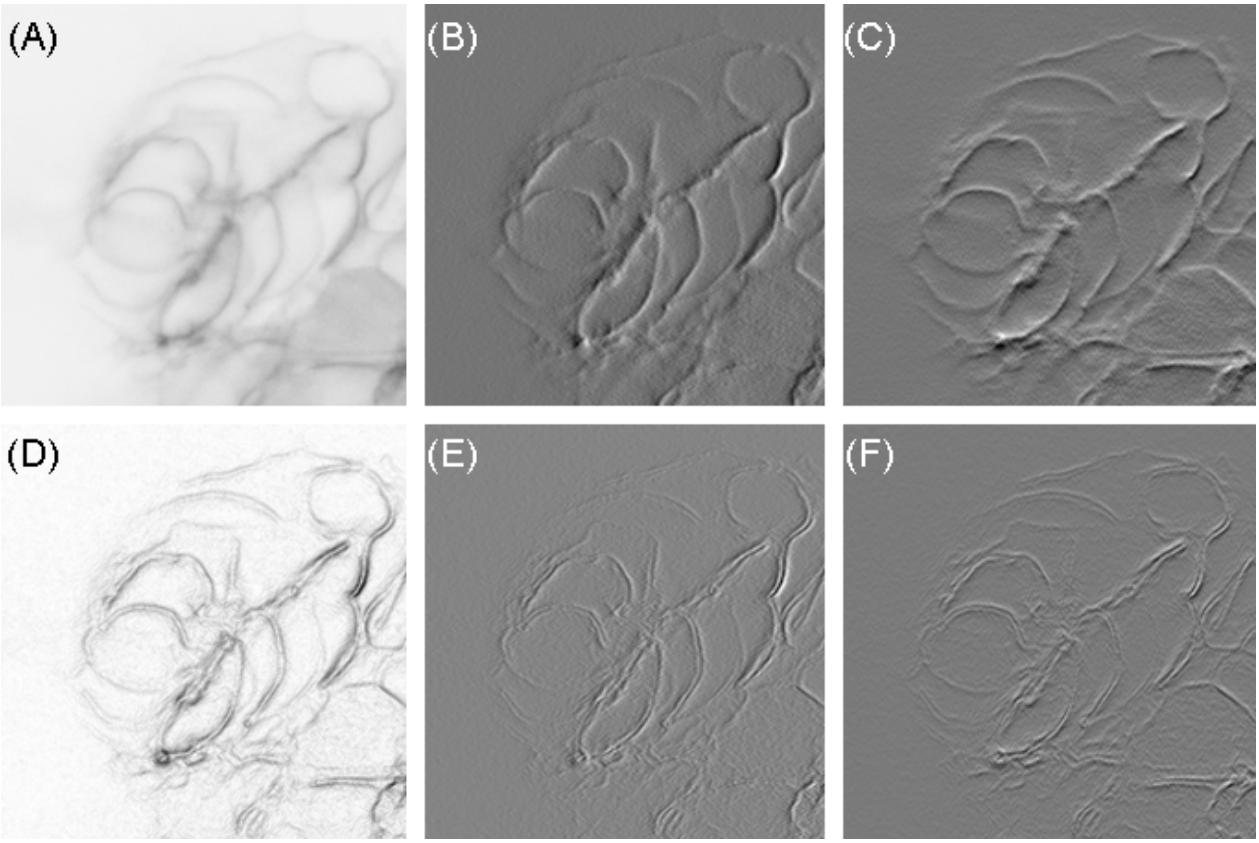

Figure 3.3: Intensity gradients and edgemap in fluorescent PpO cell membranes. **A**: Zoomed region from the sample z-slice image I of PpO cell membranes from Fig. 3.1 (intensities inverted). **B**: x-gradient image I_x. **C**: y-gradient image I_y. **D**: Edgemap image $\mathrm{e} = |I_x| + |I_y|$ (intensities inverted). **E**: Edgemap x-gradient image, e_x. **F**: Edgemap y-gradient image, e_y . In B/C/E/F, the dark (bright) zones correspond to negative (positive) intensity gradients, while the grey zones correspond to homogeneous intensities that make gradient magnitudes approach zero.

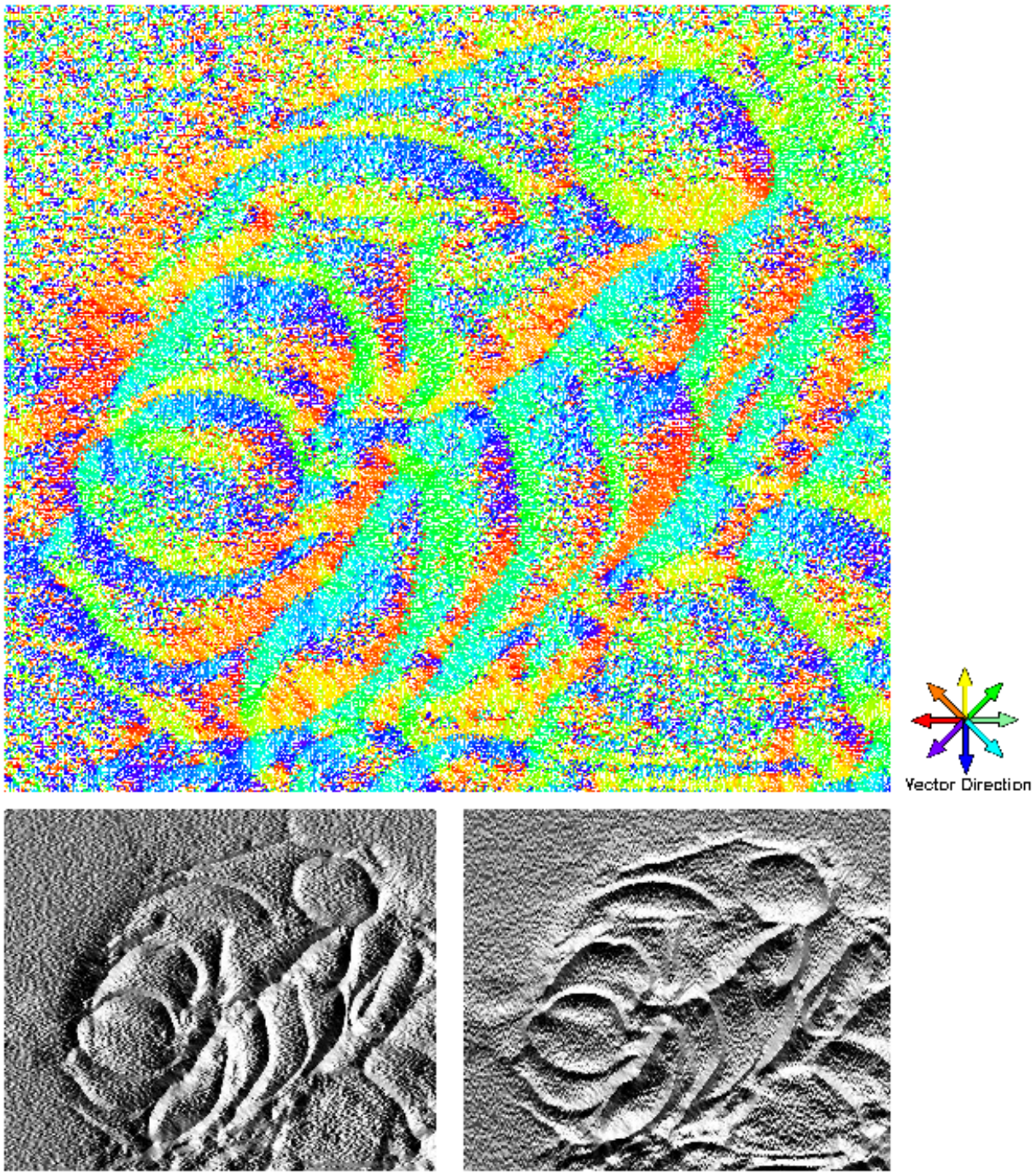

Figure 3.4: GGVF field in fluorescent PpO cell membranes. **Top**: Color-coded Generalized Gradient Vector Flow vector field, computed for the sample image of the PpO cell membranes. **Bottom left**: $GGVF$ x-component image. **Bottom right**: $GGVF$ y-component image. Computed with $g = \mathrm{e}^{-\frac{|\nabla I|}{\mu}}, \mu = 0.05$, 100 iterations.

in the original GGVF model [Xu and Prince, 1998]:

$$g(\nabla I) = \mathrm{e}^{-\frac{|\nabla I|}{\mu}} \tag{3.4}$$

The time constant μ acts as a regularization coefficient to control how pronounced the rise/decay of the vector field will be. This coefficient can be adjusted by the user according to the image residual noise/intensity homogeneity (high values yield more regularization).

The initial condition is set as $V = \nabla I$ at $t = t_0 = 0$ and the boundary conditions are $I_x = 0$ and $I_y = 0$ at the image boundaries (first and last pixel rows/columns). The vector field is then computed by a gradient-descent approach, with successive discrete values of $t \in \{t_\mathrm{i} = \mathrm{i}, \mathrm{i} > 0\}$ and updating until convergence is reached:

$$u[t+1] = g(\nabla I)\nabla^2 u[t] - h(\nabla I)(u[t] - I_x) \tag{3.5}$$
$$v[t+1] = g(\nabla I)\nabla^2 v[t] - h(\nabla I)(v[t] - I_y) \tag{3.6}$$

Since $g(\nabla I) = 1 - h(\nabla I)$, the system is rewritten to avoid redundant calculations as

$$u[t+1] = g(\nabla I)(u[t] + \nabla^2 u[t]) + b_1 \tag{3.7}$$
$$v[t+1] = g(\nabla I)(v[t] + \nabla^2 v[t]) + b_2 \tag{3.8}$$

with constant terms

$$b = I_x^2 + I_y^2 \tag{3.9}$$
$$b_1 = bI_x^2 \tag{3.10}$$
$$b_2 = bI_y^2 \tag{3.11}$$

The equations above are solved until convergence, determined when each vector component reaches a given threshold of magnitude variation considered small enough, and/or when a given limit for the number of iterations has been reached.

An additional step of Gaussian smoothing over the input image is suggested by the authors in order to further reduce spurious gradient zones of small magnitude, to be applied before computing the gradient and GVF/GGVF fields. An optional smoothing step with an isotropic Gaussian filter was implemented, implemented with matrix convolution and parametrized by the standard deviation σ (see review and examples of the smoothing process in [Spontón and Cardelino, 2015]).

As a preliminary work with regards to this thesis, GVF/GGVF approaches were implemented and applied for 2D segmentation in fluorescence microscopy imaging of lipid monolayers [Fanani et al., 2009, Fanani et al., 2010].

3.2.2 Free Parametric Active Contour Deformation

The contour deformation algorithm follows the original parametric active contour model [Kass et al., 1988]. It solved by a gradient-descent algorithm, applied to the set of contour points, and based on an energy minimization functional (see 2.2.1, Fig. 2.7). The minimization is achieved by solving an Euler-Lagrange system of partial differential equations (see mathematical background in [Aubert and Kornprobst, 2006]). Let $C_{\mathrm{i}} = C_{\mathrm{i}}(s), s \in [0,1]$ a parametric curve:

$$-\alpha\frac{\partial^2 C_{\mathrm{i}}(s)}{\partial s^2} + \beta\frac{\partial^4 C_{\mathrm{i}}(s)}{\partial s^4} + \kappa\nabla g^2(|\nabla I(C_{\mathrm{i}}(s))|)(C_{\mathrm{i}}(s)) = 0 \tag{3.12}$$

The parametric contour C_{i} of a given ROI $\mathrm{i}, \mathrm{i} \in [1, N]$, is represented by an ordered set of vertices that defines a polygon or closed polyline, $C_{\mathrm{i}} = [x_{\mathrm{i},k}, y_{\mathrm{i},k}]$, with $k = 0...n_{\mathrm{i}} - 1$. Each consecutive pair of vertices defines a segment which is the basis for adjacency detection and contour adjustment.

Using centered differences as discrete approximations of the derivatives, the Euler-Lagrange equations take the form:

$$\alpha(-C_{\mathrm{i},k+1} + C_{\mathrm{i},k} - C_{\mathrm{i},k-1}) + \beta C_{\mathrm{i},k+2} - 4\beta C_{\mathrm{i},k+1} + 6\beta C_{\mathrm{i},k} - 4\beta C_{\mathrm{i},k-1} + \beta C_{\mathrm{i},k-2} + \kappa F_{\mathrm{ext}}(C_{\mathrm{i}}, k) = 0 \tag{3.13}$$

The equation above can be used to assemble a linear equation system for all the points x and y [Kass et al., 1988], in the form of a 5-diagonal matrix A where in each row i, the elements of the non-null diagonals hold respective coefficients in terms of α and β as $C_{\mathrm{i},k-2}, C_{\mathrm{i},k-1}, C_{\mathrm{i},k}, C_{\mathrm{i},k+1}, C_{\mathrm{i},k+2}$.

Let $\underline{x}, \underline{y}$ the lists of contour positions, the iterative scheme makes $\underline{x} = \underline{x}(t), \underline{y} = \underline{y}(t)$, for successive discrete values of $t > 0$. Starting from an initial contour estimation $\underline{x}(0), \underline{y}(0)$, the equations to solve at each iteration are written as

$$\underline{x}[t+1] = (A + \gamma\mathbb{I})^{-1}(\gamma\underline{x}[t] + \kappa F_{\mathrm{ext}_x}(\underline{x}[t], \underline{y}[t])) \tag{3.14}$$

$$\underline{y}[t+1] = (A + \gamma\mathbb{I})^{-1}(\gamma\underline{y}[t] + \kappa F_{\mathrm{ext}_y}(\underline{x}[t], \underline{y}[t])) \tag{3.15}$$

where $\mathbb{I}$ denotes the identity matrix.

Equations 3.14 and 3.15 for free deformation were implemented as shown in the algorithm of Fig. 3.5. An example of the contour evolution is shown in Fig. 3.6.

The contour resampling was introduced to maintain the regular spacing between contour vertices, avoiding sparse or dense zones. A cubic spline interpolation method was implemented, with the number of vertices as input parameter. The number of vertices is determined in each case as a the quotient between the estimated contour perimeter and the sampling distance parameter (average segment length ASL, see 4.1.1).

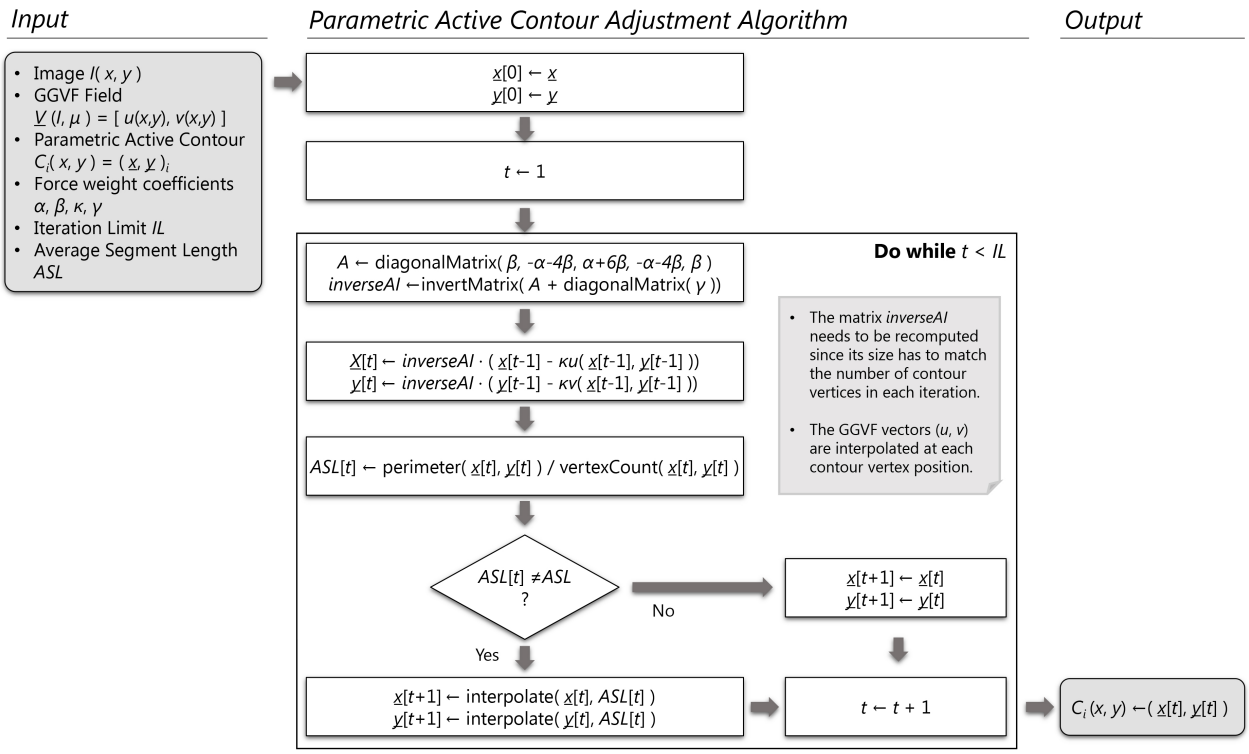

Figure 3.5: Algorithm flowchart - Parametric Active Contour Adjustment. The depicted algorithm is a variant of the classical *snakes* algorithm: it uses the GGVF vector field as image force, and includes a sampling distance parameter (ASL) to keep a regular vertex spacing during the adjustment.

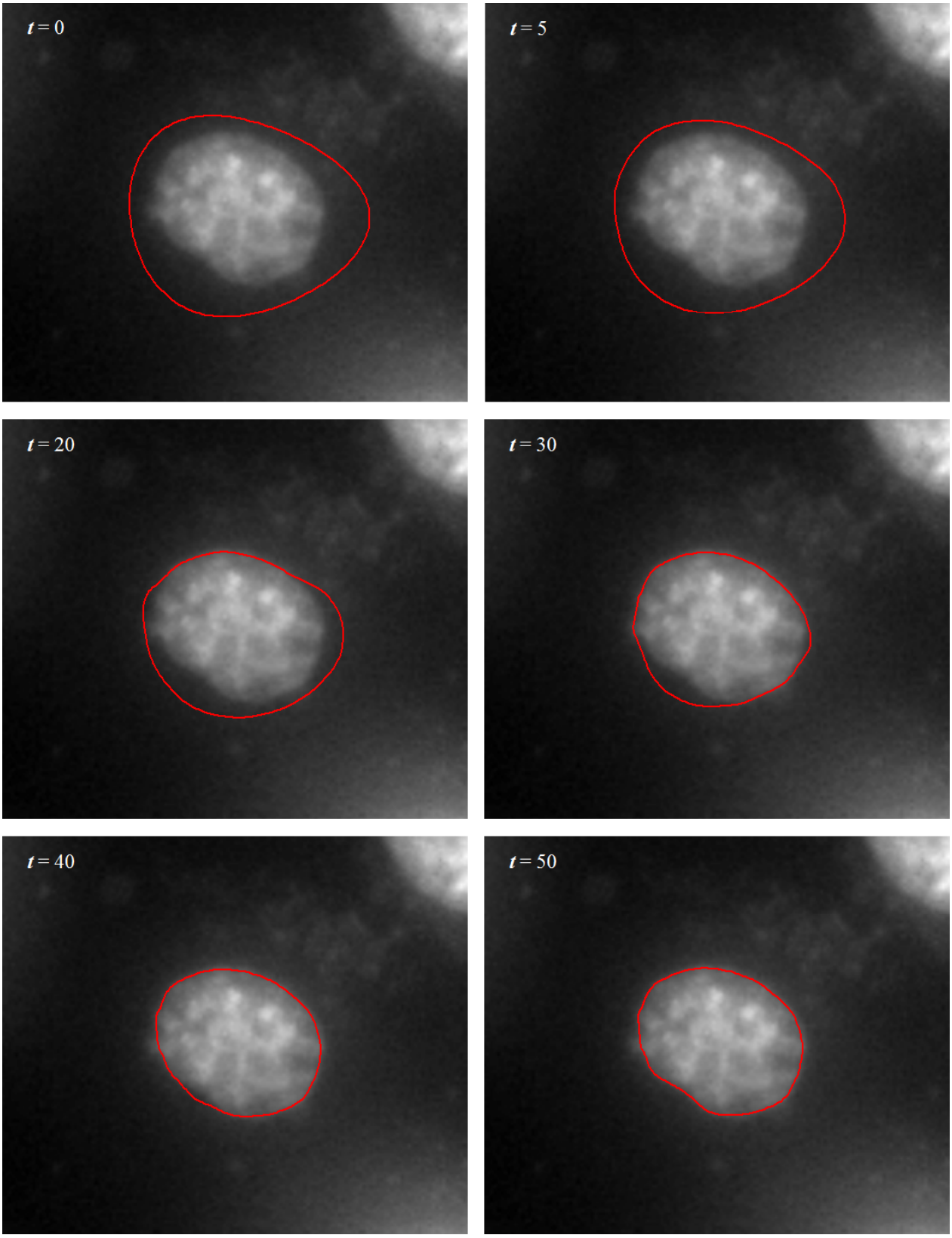

Figure 3.6: Parametric active contour deformation over the fluorescence image of a culture HeLa cell nucleus, shown at different iterations (t).

3.2.3 Detection of Adjacent, Overlapping, and Non-Adjacent Contour Sections

Once the distances between all the segments from two ROI contours have been computed, the nearest segments are checked for adjacency and overlapping:

- **Adjacent contour sections** of neighboring ROI contours are sets of one or more consecutive segments (polylines) that lie at a distance equal or lower than the Adjacency Distance d. The minimum distance between each segment of a first contour and all the segments of a second is calculated by a Segment-Segment distance algorithm [de Berg et al., 2008]. The shortest Euclidean distance is taken from each of the two vertices of the first segment to the second segment line, and from each of the two vertices of the second to the first segment line (see example in inset if Fig. 3.1D).
- **Overlapping contour sections** of neighboring ROI contours are sets of one or more consecutive segments that lie within each other, regardless of the Adjacency Distance d. Overlapping segments are detected upon the Boost implementation of the Weiler-Atherton algorithm [Weiler and Atherton, 1977, Boost, 2017]. The algorithm returns polygons that result from the intersection of two contours. Contour segments that belong to the intersections are labeled as overlapping segments and connected to define the adjacent sections.
- **Non-Adjacent contour sections** are sets of the remaining vertices which are neither adjacent nor overlapping.

3.2.4 Shared Contour Section Computation

Shared contour sections are defined for adjacent contour sections, overlapping contour sections, or sections of consecutive adjacent and overlapping segments. Each shared contour sections is a polyline that is calculated by mapping the vertices of the adjacent contour sections using the Correspondence Vertex Mapping (see 3.2.4), and averaging the position of each pair of vertices. The result is a common shared contour section (Fig. 3.7D/F/H) which depends on the selected mapping approach, and substitutes the adjacent and/or overlapping contour sections of the corresponding ROI contours.

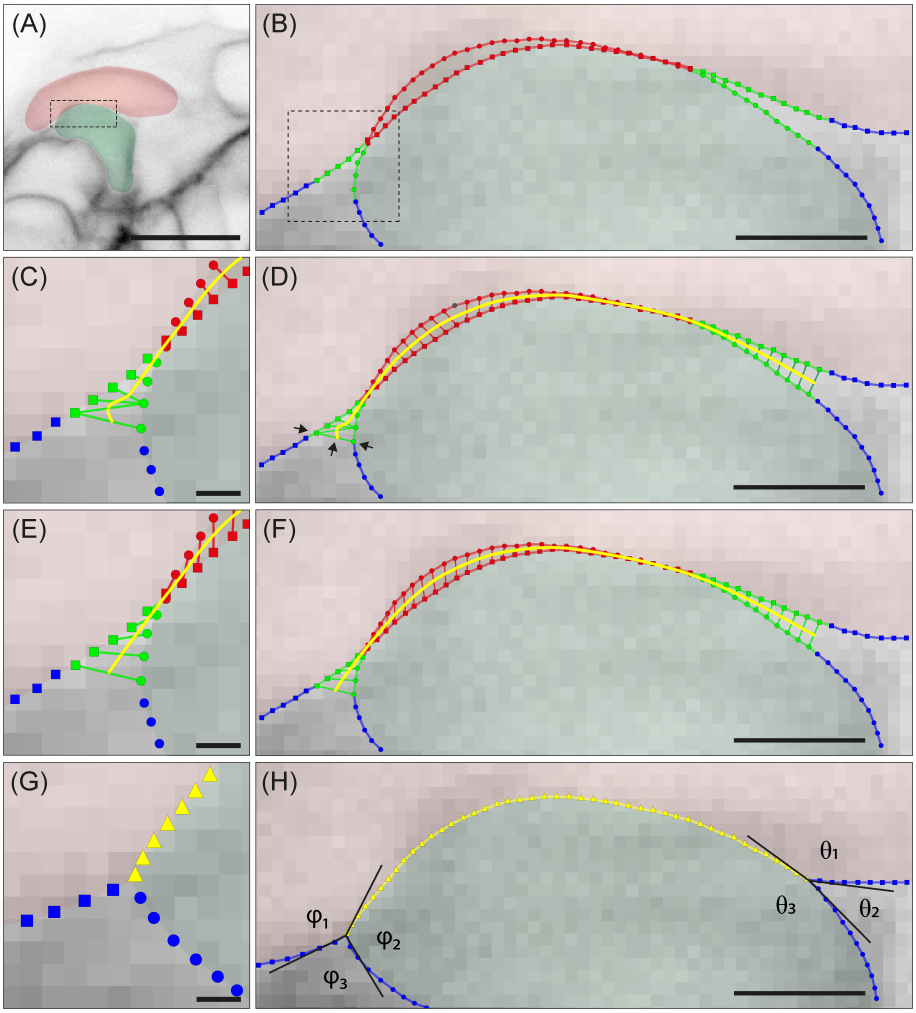

Figure 3.7: Normalized length based correspondence vertex mapping in combination with piecewise active contours lead to morphology preserving shared sections and cell contours. Scale bars for A: 10 µm, B/D/F/H: 2 µm, C/E/G: 332 nm. Arrows in D/F mark the start vertices of each section. **A**: Two neighboring PpO cells (red, green). Detail of the adjacent contour section within the dashed red rectangle is shown in B-H. **B**: Detail of adjacent (green), non-adjacent (blue), and overlapping (red) contour sections defined by $d = 332$ nm. **C-D**: Shared contour section ($C^*(x, y)$, yellow) calculated with the Euclidean distance for correspondence vertex mapping of the contour sections. C: Detail of adjacent, non-adjacent, and overlapping contour sections from the dashed rectangle in B. The vertex mapping leads to undulating extremes in the shared section. **E-F**: Shared contour section ($C^*(x, y)$, yellow) calculated with the normalized length for correspondence vertex mapping of the contour sections. The vertex mapping leads to smooth extremes in the shared section. E: Detail of adjacent, non-adjacent, and overlapping contour sections from the dashed rectangle in B. **G-H**: Piecewise active contours ($C^{**}(x, y)$, yellow triangles and blue squares and circles) guarantee smooth transitions between adjacent and non-adjacent contours, and preserve cell morphology of the two neighboring PpO cells. Angles of the triplet vertices and the corresponding cell contours can be calculated by fitting straight lines to a selected number of contour vertices next to the tip (see representative line segments for angles $\varphi_1, \varphi_2, \varphi_3$,) and $\theta_1, \theta_2, \theta_3$. G: Detail of adjacent, non-adjacent, and overlapping contour sections from the dashed rectangle in B. Published in [Jara-Wilde et al., 2020].

Correspondence Vertex Mapping

The correspondence vertex mapping for two contour sections returns a list of paired vertices for each contour. Two approaches were tested.

A. Euclidean Distance Correspondence Vertex Mapping The correspondence list is constructed by the following sequence:

1. The contour section with the higher number of vertices is selected as reference. If the numbers are equal, the result is independent of the selection.
2. The first two vertices of the polylines are connected, becoming the first pair of the correspondence list. The result is independent of the selection of the first or the last vertex.
3. For each following vertex of the reference polyline, the closest vertex of the second polyline is detected. The paired vertices are added to the correspondence list consecutively.
4. The last two vertices of the polylines are connected, becoming the last pair to the correspondence list.

B. Normalized Length Correspondence Vertex Mapping The correspondence list is constructed by the following sequence:

1. The length of each contour section is calculated by the sum of the length of its segments. The length of a segment is the Euclidean distance between its vertices.
2. Each segment is normalized by the total length of its section, in order produce 1-dimensional normalized vertex positions. The vertices of each section have a normalized length [0,1], with vertices at length 0 and 1 as start and end, respectively.
3. One of the sections is taken as reference list to start the correspondence list. For sections with unequal numbers of vertices, the polyline with more vertices is used. The correspondence list is generated by advancing vertex by vertex from the reference list, matching with the closest vertex in the second list. The matching is made by comparing the normalized lengths of the vertices. The result is independent of the starting vertex.

3.2.5 Piecewise Active Contours Reconstruction

As described before, the algorithm returns one of three possible outputs: (i) Parametric Contours $C_{\mathrm{i}}(x, y)$ without adjacent sections, (ii) Parametric Contours $C_{\mathrm{i}}^{*}(x, y)$ where all sections fulfill the adjacency criteria, and (iii) Piecewise Parametric Contours $C_{\mathrm{i}}^{**}(x, y)$ with sections that fulfill the adjacency criteria and sections that do not. For (i) and (ii), there is no need for further adjustment of the ROI contours. For (iii), the shared contour sections (see 3.2.4) are connected to the non-adjacent contour sections and form a new, adjusted ROI contour. To obtain smooth contours, a piecewise active contour algorithm was applied to adjust non-adjacent contour sections under the constraints of the active contour approach, while keeping the vertices of shared contour sections at fixed positions. The result of this piecewise approach is shown in Fig. 3.7H.

3.3 Implementation Language and Libraries

The main algorithms were implemented in IDL 7.1.2 (ITT/Harris Geospatial, Boulder, CO), a scientific programming language with native support for matrix and vector operations, object orientation, and 2D/3D interactive visualization functions. Further, the algorithms were integrated within the software toolbox SCIAN-Soft from the host laboratory[1] to provide functions for 2D/3D image manipulation, filtering, segmentation; ROI reconstruction, morpho-topology descriptions, tracking; and interactive analysis and visualization. Selected utility algorithms were implemented as dynamic link libraries for improved execution time:

- Polygon intersection computations, implemented in C++ using the geometry package from the Boost library, version 1.71.0 [Boost, 2017].
- Sweep-and-Prune algorithm for 2D axis-aligned bounding boxes, implemented in C++.

The utility algorithms were encapsulated in custom functions, and compiled/built as dynamic link libraries using Visual Studio 2010 version 10.0.40219 SP1Rel (Microsoft, Redmond, WA), in order to be integrated with SCIAN-Soft. The developed code is currently being published at GitHub at `https://github.com/scianlab/sciansoft`.

Experiments (Chapter 4) were performed in a custom built computer, with Core i7 3930K CPU (Intel Corp., Santa Clara, CA), 64GB RAM, 64-bit Windows 7 SP1 Operating System (Microsoft, Redmond, VA).

3.4 Implemented Optimizations

3.4.1 Neighbor ROI/Shared Section Computations

- **Axis-aligned bounding boxes**. When the ROI contours are initialized, the maximum and minimum x and y coordinate values of each contour are stored. They define N rectangles which enclose the ROI contours, and can be checked with a fixed number ($O(1)$) of simple and fast operations to avoid unnecessary detailed comparisons for non-adjacent ROIs. Still, some non-adjacent ROIs can have their overlapping AABBs, but in practice the ratio between the total number of ROIs N and the average of neighbors n_{avg} (for a given ROI) can go from 2 to 20, favoring the use of AABBs. The comparison algorithm is shown in Figure 3.8. In a similar way, when a shared section is constructed, a corresponding AABB is created. In order to account for the proximity distance, the AABBs for the ROI contours are expanded in each direction (with half the specified distance).
- **Sweep-and-Prune** [Cohen et al., 1995]. The $N-1$ AABBs are sorted along the x and y axes in average $O(N \log N)$ operations each (quicksort algorithm), and stored in a heap array. The array is traversed to find pairs of possibly adjacent ROIs or shared sections, whose AABBs lie within the proximity threshold distance, adding N look-up operations (one for each ROI/shared section) to check the distance between adjacent AABBs in the array. The average number of adjacent ROIs in the observed images ranges from 1 to 6, bounding the number of comparisons per look-up operation.

[1] `http://www.scian.cl`

3.5 Computational Complexity

3.5.1 Operations

The main contributing factor to the computation time is the number of ROIs, N in the input image. Coupled to it, the number of points of each ROI contour, including the interpolation factor or point density, factors into the number of operations. Let $c_{\mathrm{i}} = \{[x_p, y_p]\}, p = 1...n_{\mathrm{i}}$ a single ROI contour, the main tasks and their computation costs are:

- Contour deformation, $O(n_{\mathrm{i}})$ for computing the deformation vector over each point and $O(5n_{\mathrm{i}}) = O(n_{\mathrm{i}})$ for the 5-diagonal matrix inversion, if a restricted Gaussian elimination is implemented to take advantage of the matrix sparsity and diagonal symmetry.
- Bounding geometry construction, $O(n_{\mathrm{i}})$ for AABBs.
- Contour resampling, $O(n_{\mathrm{i}})$ for linear interpolation.
- Broadband adjacency checking, $O(1)$ against each other ROIs (pairwise), which totals $O(N \log_2 N)$ for all other ROIs, when using the Sweep-and-Prune algorithm.
- Narrowband adjacency checking against ROI contour $c_j = \{[x_q, y_q]\}, q = 1...n_j$, is the most expensive task which takes $O(n_{\mathrm{i}} n_j)$ operations, accounting for the intersection and proximity computations, and the subsequent scanning for vertex runs, and totaling $O(c_1 n_{avg} n_{avg})$ with c_1, n_{avg} the average number of ROI neighbors and points, respectively.
- Broadband checking for corners (more than two ROIs), has a theoretical cost equivalent to the ROI broadband checking for shared sections, with the addition of one intersection computation for each pair of ROI sections with intersecting AABBs.
- Narrowband checking for corner merging adds the intersection computation for each candidate shared section to be included in a corner.
- Separation computation, dependent on the method of choice (see 3.2.4).
- Iteration convergence update, $O(n_{\mathrm{i}})$ for each ROI.

3.5.2 Memory

The required memory depends linearly on the input size for most of the data structures. Namely:

- The list of N AABBs for each ROI contour.
- The N lists of n_{i} vertices that defines each ROI contour.
- The list of AABBs/bounding polygons and image patches for each of the N_s shared sections.
- The N_s lists of vertices of the adjacent ROIs and their adjusted shared sections.
- The image I, gradients and vector field $GGVF$.

The main non-linear memory data structure is the correspondence vertex matrix that needs to be computed for each ROI pair. It takes $O(n_{\mathrm{i}}^2)$ memory space since it is a square array that stores the distance between each possible pair of segments from neighboring ROI contours.

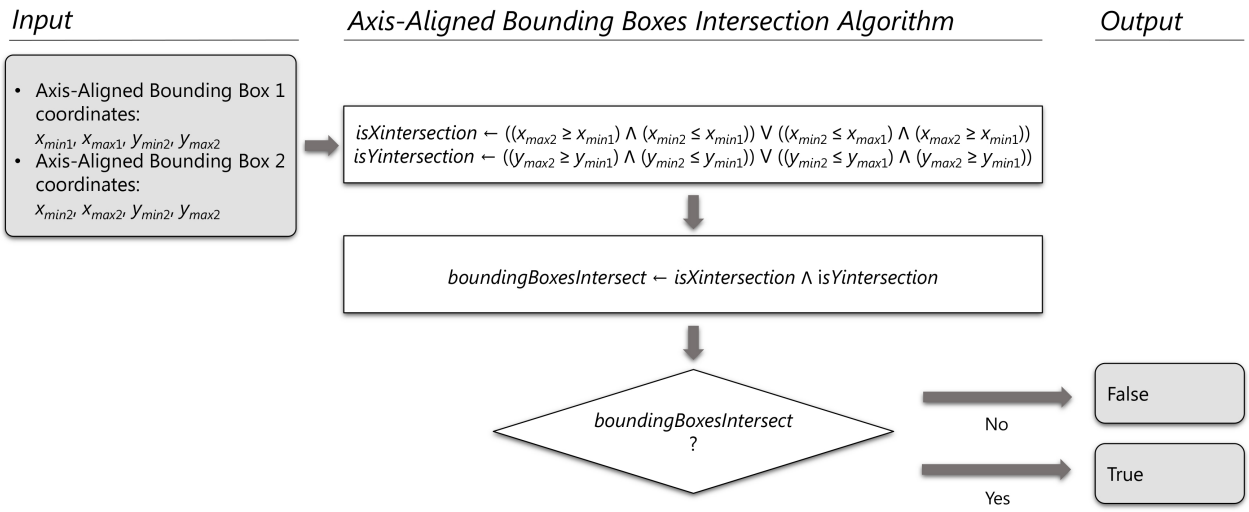

Figure 3.8: Algorithm flowchart - Axis-Aligned Bounding Boxes Intersection. Each bounding box is a rectangle that can be entirely defined by the xy coordinates of two of its opposing corners. The intersection of two bounding boxes occurs if and only if they intersect along both the x and y axes.

Chapter 4

Validation and Application

This section presents the evaluation of the developed ALPACA method in selected synthetic and real microscopy images. The chapter is organized as follows: first, quality indicators for contour and shared sections are presented (4.1); next, test cases and algorithm parameters are presented (4.2), followed by the results and discussion (4.3). Finally, a qualitative comparison between ALPACA and alternative approaches is presented (4.4).

4.1 Quality Indicators

Since ground truth cannot be defined for real images, test scenarios and contour similarity indicators were defined to assess the performance of ALPACA. This kind of approach has been previously used in biological image analysis for fluorescent signals such as co-localization [Ramírez et al., 2010], motion estimation [Baker et al., 2011, Zimmer et al., 2011, Delpiano et al., 2012], and segmentation [Coelho et al., 2009, Castañeda et al., 2014]. Quality criteria and tests were selected by considering expert knowledge about adjacent cell membranes in 2D/3D fluorescence microscopy with weak fluorescence intensity gradients to assess the shared section between cell membranes.

4.1.1 Morphological Indices

Seven indices were defined to quantify the difference of the morphology of the ROIs before and after ALPACA, and the characteristics of the shared contour sections: Relative Area Variation (RAV), Relative Perimeter Variation (RPV), Relative Adjacent Length Variation (RALV), Relative Non-Adjacent Length Variation (RNALV), Section Distance Sim_D, Section Curvature Sim_K, Section Length Sim_L, and Average Segment Length Sim_{ASL}. The indices were calculated using n_1 corresponding to the number of shared contour sections, n_2 corresponding to: (i) each pair of cells adjacent in each shared contour section ($n_2 = 2n_1$) for Relative Area & Perimeter Variation, (ii) each ROI of the slice ($n_3 = 17$) for Relative Adjacent and Non-Adjacent Length Variation, and (iii) each shared contour section (n_1) for the rest.

Relative Area & Perimeter Variation

The basic morphological descriptors area and perimeter are used to quantify the relative variation of the adjusted contours $C_{\mathrm{i}}^{**}(x,y)$ with respect to the original contour $C_{\mathrm{i}}(x,y)$:

- The Perimeter of a contour $C_{\mathrm{i}}(x,y)$ is determined by the sum of the length of its segments.
- The area of a contour $C_{\mathrm{i}}(x,y)$ is calculated with the shoelace algorithm for polygons [Braden, 1986].
- The Relative Perimeter Variation is calculated by

$$\frac{Perimeter(C_{\mathrm{i}}^{**}(x,y))}{Perimeter(C_{\mathrm{i}}(x,y))}. \tag{4.1}$$

- Relative Area Variation RALV is calculated by

$$\frac{Area(C_{\mathrm{i}}^{**}(x,y))}{Area(C_{\mathrm{i}}(x,y))}. \tag{4.2}$$

- The Normalized Perimeter Difference is calculated by

$$\frac{|Perimeter(C_{1,\mathrm{i}}(x,y)) - Perimeter(C_{2,\mathrm{i}}(x,y))|}{max\left\{Perimeter(C_{1,\mathrm{i}}(x,y)), Perimeter(C_{2,\mathrm{i}}(x,y))\right\}}. \tag{4.3}$$

- The Normalized Area Difference is calculated by

$$\frac{|Area(C_{1,\mathrm{i}}(x,y)) - Area(C_{2,\mathrm{i}}(x,y))|}{max\left\{Area(C_{1,\mathrm{i}}(x,y)), Area(C_{2,\mathrm{i}}(x,y))\right\}}. \tag{4.4}$$

Relative Adjacent & Non-Adjacent Length Variation

For each ROI contour, the relative length of the adjacent and non-adjacent sections is calculated as the sum of their segment lengths, and divided by the total contour perimeter. The variation is then calculated as the ratio between the relative lengths of the adjusted contours with respect to their original lengths In order to consider sections with only one vertex the half-length of extreme segments were also summed.

Section Distance

The similarity indicator Section Distance (Sim_D) is defined from the area ratio between contour sections as

$$Sim_{\mathcal{D}} = 1 - \frac{|A_C(SC, AC_1) - A_C(SC, AC_2)|}{A_C(SC, AC_1) + A_C(SC, AC_2)} \tag{4.5}$$

The Contour Area (A_C) defines the area between the Shared Contour (SC) sections and the Adjacent Contour (AC) sections of the first and the second contour (AC_1 and AC_2) section. The area between the contour sections $A_C(SC, AC_{1/2})$ is calculated also by the shoelace algorithm as in 4.1.1.

Section Curvature

The similarity indicator Section Curvature (Sim_K) is defined by the following steps:

1. First, correspondence lists $v_l = 0...N_\mathrm{i} - 1$ between contour sections are defined as in 3.2.4 to allow vertex by vertex comparisons.
2. The Curvature (K) of contour sections is calculated for all of its vertices $v_l = 0...N_\mathrm{i} - 1$ using the differential curvature approximation [Yates, 1974], considering their neighbors v_{l+1} and v_{l-1}. For the first v_0 and the last vertex $v_{N_\mathrm{i}-1}$ of a contour section, the curvature cannot be determined due to missing neighbors.
3. Sim_K is calculated as

$$Sim_\mathcal{K} = 1 - \frac{|\sum_l \Delta K_l(SC, AC_1) - \sum_l \Delta K_l(SC, AC_2)|}{\sum_l \Delta K_l(SC, AC_1) + \sum_l \Delta K_l(SC, AC_2)} \tag{4.6}$$

4. The difference of curvature (ΔK_i) is calculated as the sum of differences of curvature between the Shared Contour (SC) section and the Adjacent Contour sections (AC_1 and AC_2).
5. The difference is summed over all the vertices to obtain the value of Sim_K.

Section Length

The similarity indicator Section Length (Sim_L) is defined as

$$Sim_\mathcal{L} = 1 - \frac{|L(SC)/L(AC_1) - L(SC)/L(AC_2)|}{L(SC)/L(AC_1) + L(SC)/L(AC_2)} \tag{4.7}$$

The Length (L) of contour sections $L(SC)$, $L(AC_1)$ and $L(AC_2)$ is calculated as the sum of the length of the contour segments (as in 4.1.1).

Average Segment Length

The similarity indicator Average Segment Length (Sim_{ASL}) of a section is defined as

$$Sim_{\mathcal{ASL}} = 1 - \frac{|ASL(SC)/ASL(AC_1) - ASL(SC)/ASL(AC_2)|}{ASL(SC)/ASL(AC_1) + ASL(SC)/ASL(AC_2)} \tag{4.8}$$

$ASL(Contour)$ is calculated by dividing the contour total length by the number of its segments. $ASL(AC_1)$ and $ASL(AC_2)$ are averaged and compared to $ASL(SC)$.

4.1.2 Similarity Indices

This section provides the quantitative error metrics for comparing experimental results of ALPACA against a reference or ground truth segmentation, which in this case corresponds to the manual drawings made by an expert in the test cases.

For a common notation regarding a given segmentation of a single ROIs and its corresponding ground truth, let

- GT: the ground truth contour polygon of a given ROI,
- S: the segmented ROI contour polygon (to be evaluated against GT),
- TP: the number of true ROI pixels (*true positives*),
- TN: the number of true background pixels (*true negatives*),
- FP: the number of false ROI pixels (*false positives*), and
- FN: the number of false background pixels (*false negatives*).

Intersection-based Indices

The Dice Coefficient $\mathrm{DC}(C_{1,\mathrm{i}}, C_{2,\mathrm{i}})$ [Dice, 1945, Sørensen, 1948] and the Jaccard Similarity Index $\mathrm{JC}(C_{1,\mathrm{i}}, C_{2,\mathrm{i}})$ [Coelho et al., 2009] for two contours $C_{1/2,\mathrm{i}}(x, y)$, were implemented on the basis of the Area definition and polygon intersection and union (see 4.1.1).

- **Dice Coefficient**

$$\mathrm{DC}(S, GT) = \frac{2\,|S \cap GT|}{|S| + |GT|} = \frac{2TP}{(FP + TP) + (TP + FN)} = \frac{2TP}{2TP + FP + FN} \tag{4.9}$$

  For a polygon-based representation of each ROI between any pair of segmented contours $C_{1,\mathrm{i}}, C_{2,\mathrm{i}}$, the Dice coefficient is defined as:

$$\mathrm{DC}(C_{1,\mathrm{i}}, C_{2,\mathrm{i}}) = \frac{2\,|C_{1,\mathrm{i}} \cap C_{2,\mathrm{i}}|}{|C_{1,\mathrm{i}}| + |C_{2,\mathrm{i}}|} \tag{4.10}$$

  Here, the polygon intersection and union areas between $C_{1,\mathrm{i}}$ and $C_{2,\mathrm{i}}$ are used to compute the coefficient value.

- **Jaccard Similarity Index/Tanimoto Coefficient**

$$\mathrm{JC}(S, GT) = \frac{|S \cap GT|}{|S \cup GT|} = \frac{TP}{TP + FP + FN} \tag{4.11}$$

  In the same way as with the Dice coefficient, this index is defined to account for a polygon-based computation of the similarity between any pair of contours obtained for a given ROI:

$$\mathrm{JC}(C_{1,\mathrm{i}}, C_{2,\mathrm{i}}) = \frac{|C_{1,\mathrm{i}} \cap C_{2,\mathrm{i}}|}{|C_{1,\mathrm{i}} \cup C_{2,\mathrm{i}}|} \tag{4.12}$$

For both Similarity Indices, Dice and Jaccard, the value 1 indicates perfect match between the compared contours, and the value 0, null match.

Boundary-based Indices

- **Hausdorff Distance** HD [Atallah, 1983]. Defined for two contours $C_{1/2}(x, y)$, it was calculated based on the distance algorithm for the line segments that form each contour polygon (see 3.2.3).

  Let D_k the distance from element $k \in C_{1,\mathrm{i}}$ to $C_{2,\mathrm{i}}$, HD is defined first by

$$h\mathrm{d}(C_{1,\mathrm{i}}, C_{2,\mathrm{i}}) = max\left\{D(k) : C_{1,\mathrm{i}_k} \neq C_{2,\mathrm{i}_k}\right\} \tag{4.13}$$

Considering that both object boundaries are represented by polygons, HD can be expressed in terms of the euclidean distance between segments as:

$$\mathrm{HD}(C_{1,\mathrm{i}}, C_{2,\mathrm{i}}) = max(h\mathrm{d}(C_{1,\mathrm{i}}, C_{2,\mathrm{i}}), h\mathrm{d}(C_{2,\mathrm{i}}, C_{1,\mathrm{i}})) \tag{4.14}$$

with hd defined for any pair of polygons $C_{1,\mathrm{i}}, C_{2,\mathrm{i}}$ that represent the ROI i.

$$h\mathrm{d}(C_{1,\mathrm{i}}, C_{2,\mathrm{i}}) = \frac{1}{p}\sum_{k=1}^{p} min_{s_2 \in C_{2,\mathrm{i}}} \|s_{1k} - s_2\| \tag{4.15}$$

- **Normalized Sum of Distances** NSD [Coelho et al., 2009]. It accounts for the accumulated differences (distance) from the pixels of the resulting ROI contours to the reference ones.

  Let D_k the distance from pixel $k \in C_{1,\mathrm{i}}$ to $C_{2,\mathrm{i}}$, NSD is defined as:

$$\mathrm{NSD}(C_{1,\mathrm{i}}, C_{2,\mathrm{i}}) = \frac{\sum_k [C_{1,\mathrm{i}_k} \neq C_{2,\mathrm{i}_k}] * D_k}{\sum_k D_k} \tag{4.16}$$

  or, equivalently [Bergeest and Rohr, 2012],

$$\mathrm{NSD}(C_{1,\mathrm{i}}, C_{2,\mathrm{i}}) = \frac{\sum_{k \in C_{1,\mathrm{i}} \cup C_{2,\mathrm{i}} \setminus C_{1,\mathrm{i}} \cap C_{2,\mathrm{i}}} D_k}{\sum_{k \in C_{1,\mathrm{i}} \cup C_{2,\mathrm{i}}} D_k} \tag{4.17}$$

  with values ranging from 0 (perfect match) to 1 (no overlap). As stated by the authors, NSD is not a metric because it is not symmetric nor does it satisfy the triangle inequality. However, NSD reflects the cumulative sum of contour misalignment, unlike any of the previous indicators. In order to be consistent with the Hausdorff Distance computation, distance between polygon segments (instead of points/vertices) was used (see 3.2.3).

4.2 Test and Validation Cases

ALPACA was tested on cell aggregates from spinning-disk confocal microscopy images of a fluorescent zebrafish embryo [Waters and Wittman, 2014, Pawley, 2006]. The sequence is part of a routine experiment in brain asymmetry studies within developmental biology [Lemus et al., 2021], and as such it provides a representative case of *in vivo* experiments with 3D multi-cellular samples, regarding 3D live imaging acquisition settings and image characteristics. In addition, a simpler, synthetic test case in 2D was defined with cells of regular shape, size, and neighbor distances.

4.2.1 Microscopy Image Acquisition of PpO Cells

Zebrafish (*Danio rerio*) embryos were obtained by natural spawning from a *flh*::GAP43-EGFP transgenic zebrafish line [Concha et al., 2003]. The sample embryo was anesthetized (Tricain 0.003%) and mounted in 1% low melting point agarose. The PpO morphogenesis was observed using a spinning disk confocal microscope (ZEISS; Jena, Germany/PerkinElmer; Waltham, MA) under controlled temperature conditions (28° C). 3D Image stacks (8-bit single channel intensity $I \in [0, 255]$) of $768 \times 768 \times 69$ voxels xyz and $166 \times 166 \times 500$ nm voxel size were captured with a 40× (NA 1.2) water-immersion objective, and excitation/emission wavelength at 488/505-560 nm. Raw images were deconvolved with Huygens Software (SVI, Hilversum, The Netherlands). Sampling distances were calculated with Nyquist rate and PSF calculator[1].

4.2.2 Synthetic Image with Hexagon Cells of Defined Adjacency

A 2D vector image for 88 hexagons was generated with Adobe Illustrator software (Adobe; San Jose, CA), and rasterized to 768×768 pixels. Horizontal edges of the hexagons were 43 pixels long, diagonal edge length and pixel representation varied slightly due to the rasterization algorithm. The membrane adjacency between hexagons was defined as follows: 11 hexagons with 6 Adjacent Edges (AE), 17 with 5 AE, 13 with 4 AE, 12 with 3 AE, 13 with 2 AE, 11 with 1 AE, and 11 hexagons without AE (0 AE). The distances for hexagons with 0 AE to the next hexagon varied from 3 to 12 pixels. Edge/background intensity was set to 255/0 (8 bit). The image was convolved with the theoretical PSF calculated with Huygens Software for a pixel size identical to the xy microscope settings (166×166 nm^2), and re-scaled to 8-bit (Fig. 4.5A).

4.2.3 Manually Outlined Contours (MOC)

Membrane segmentation was performed by three independent experts with 2-15 years of training in *in vivo* microscopy and manual segmentation of diverse cell structures. The contour of each object was outlined as a closed polygon using a digital Pen CTE-440 tablet (Wacom; Saitama, Japan). Binary ROIs were generated with a custom-made macro written for the Image SXM software [Barrett, 2015].

- **PpO cells** 17 Cells, totaling 51 MOC in consecutive xy planes along the z axis.
- **Synthetic cells** 88 Synthetic hexagons 4.2.2.

[1] `https://svi.nl/NyquistCalculator`

4.2.4 Algorithm Settings

Parametric Active Contours (PAC)

The iterative solving scheme from for energy minimization of each contour was modified in order to allow fixed contour vertices from shared sections.

- **PpO cells** The following energy weight coefficient values were used:
  - elasticity $\alpha = 0.0002$,
  - rigidity $\beta = 0.003$,
  - image force field (GGVF) $\kappa = 0.0015$.

  The following contour parameter values were used:
  - viscosity $\gamma = 1.0$,
  - average segment length $ASL = 1$ (equivalent to the pixel length of 166 nm),
  - maximum deformation iterations = 1000,
  - convergence threshold $= 2 \times 10^{-6}$. The measurement used for evaluating the convergence is the ratio between the maximum vertex displacement and the ROI perimeter.

  GGVF field coefficient values:
  - regularization $\mu = 0.5$,
  - iterations = 100.
- **Synthetic cells** The same parameter values used for the PpO cells were used, except:
  - elasticity $\alpha = 0.0001$,
  - rigidity $\beta = 0.5$,
  - image force field (GGVF) $\kappa = 0.5$.

ALPACA

The Adjacency Distance d was set to $83, 166, 332, 498$ nm, equivalent to $0.5, 1.0, 2.0, 3.0$ pixel length for the PpO cells, and 0.5 for the synthetic cells.

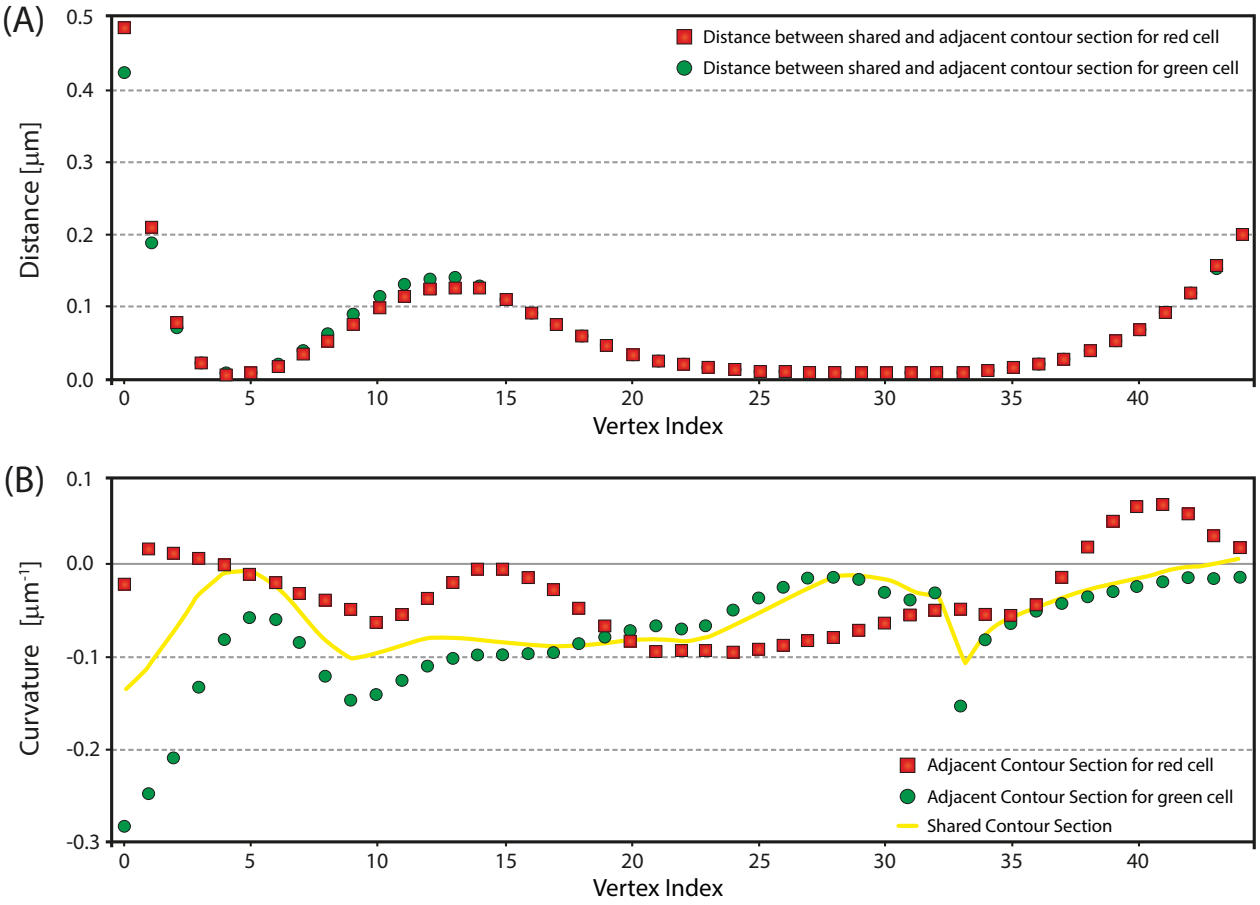

Figure 4.1: Distance and curvature of a sample shared section calculated by ALPACA are balanced with respect to the original ROI contour sections. Distance and curvature of the shared contour section and the adjacent contour sections are plotted as a function of the vertex index for the green and red cell contours shown in Fig. 3.7. The vertex index 0 is indicated by the arrows in Fig. 3.7F. **A**: Distances between the shared contour section and the adjacent and overlapping contour sections of the red and the green cell are plotted as red squares and green dots. A maximum difference of 485 nm was detected for the first vertex (index 0). **B**: Curvature plot of the shared contour section (yellow line) and the adjacent and overlapping contour sections of the red and the green cell are plotted (red squares and green dots). The curvature of each section is calculated using a differential-derived formulation [Yates, 1974]. Positive and negative curvature signs correspond to clockwise and anti-clockwise section turns, respectively. Published in [Jara-Wilde et al., 2020].

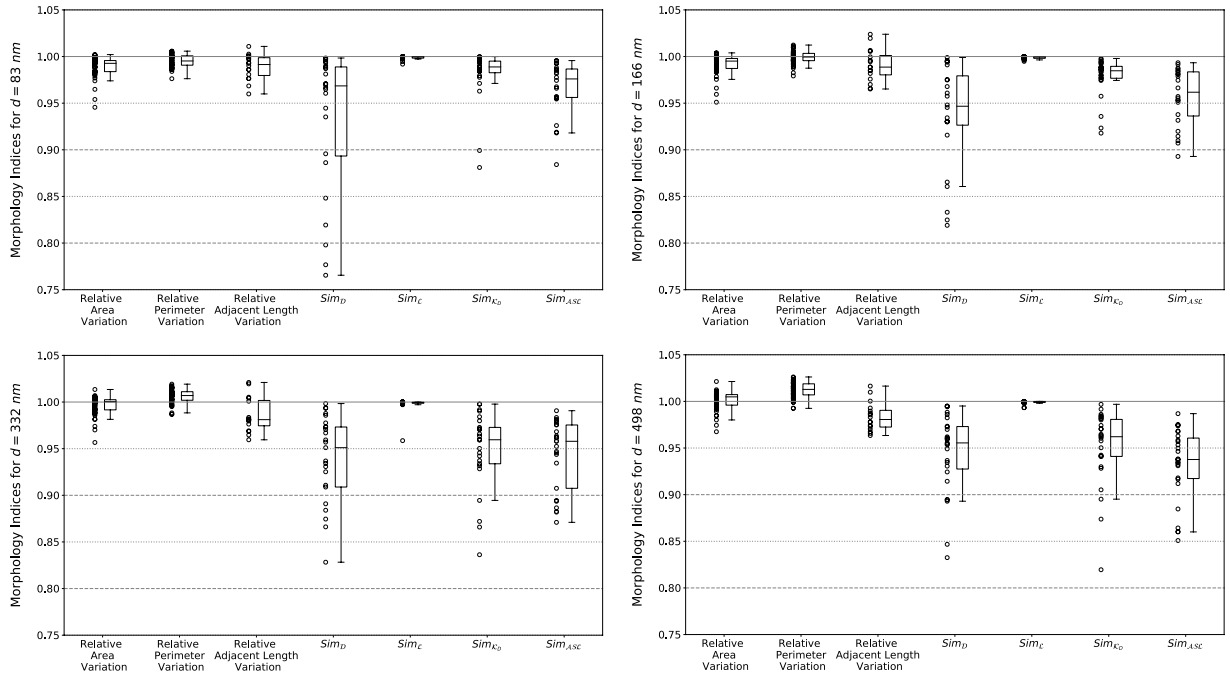

Figure 4.2: Morphological Indices for increasing Adjacency Distance $d = 83, 166, 332$, and 498 nm (from left to right and top to bottom) of PpO cell contours after the application of ALPACA. Three morphological indices (Relative Area, Perimeter, and Adjacent Length Variation) quantify the deviation of the adjusted contours $C_{\mathrm{i}}^{**}(x, y)$ relative to the initial contours $C_{\mathrm{i}}(x, y)$. Four similarity indices ($Sim_D, Sim_L, Sim_K, Sim_{ASL}$) compare shared sections with their respective adjacent/overlapping sections (see description in 4.1.1Indices were normalized with respect to the initial ROI contours $C_{\mathrm{i}}(x, y)$ which are set to 1. Aligned scatter plots contain data for each of the 17 cells with respect to each of the corresponding neighbors (see 4.1.1 for definition), and section similarity indices were computed from the detected shared sections. Published in [Jara-Wilde et al., 2020].

4.3 Results and Discussion

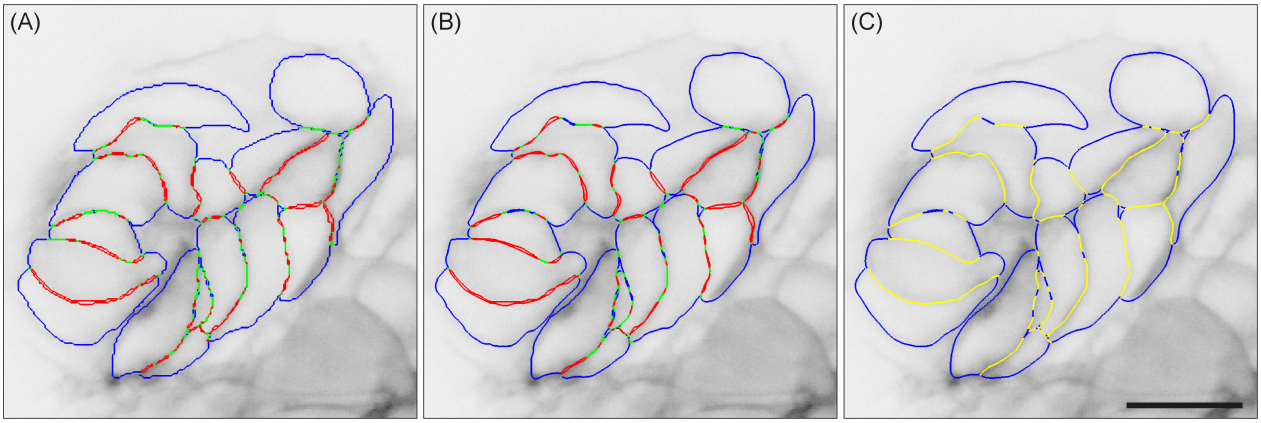

Figure 4.3: Optimized detection and adjustment of adjacent and non-adjacent PpO cell membrane contour sections with an Adjacency Distance $d = 83\,\text{nm}$. Scale bar: $10\,\mu\text{m}$. **A**: Adjacent (green), non-adjacent (blue), and overlapping (red) contour sections $C_\text{i}(x, y)$ detected by ALPACA are plotted on top of the corresponding intensity image $I(x, y)$. **B**: Final adjustment of non-adjacent (blue) and shared (yellow) contour sections $C_\text{i}^{**}(x, y)$ are plotted after application of ALPACA. Published in [Jara-Wilde et al., 2020].

Figure 3.1 shows imaging data and cell membrane segmentations acquired to study the dynamics of PpO morphogenesis (see also 4.2.1). During PpO morphogenesis, 12-18 neuroepithelial adjacent cells form a rosette-like structure and detach from the pineal complex to form a small nuclei on the left side of embryonic zebrafish brain (see [Concha et al., 2003, Härtel et al., 2007, Regan et al., 2009], Fig. 3.1A). Imaging characteristics and quality shown in Fig. 3.1 represent typical scenarios for *in vivo* experiments that focus on group cell migration or tissue development and the use of fluorescent membrane proteins to outline the living form of cells and tissue [Lecaudey et al., 2008, Richardson et al., 2016, Reig et al., 2017, Sanchez-Corrales et al., 2018]. The selected pixel size (166×166 nm) is about 3 times the suggested Nyquist rate of 50 nm (see Section 4.2.1). However, fast *in vivo* imaging is a trade-off between maximizing resolution, the field of view, and fluorescence intensity, and minimizing photon damage, bleaching, and signal noise. For experimental conditions such as the one presented here, the Nyquist rate cannot be kept. In this case, a rate of 166 nm was selected.

Figure 3.1B shows membrane signals that vary in peak intensity and the width of the Gaussian intensity profile of the xy plane. The variations can be explained by the different orientations of the membrane sheets with respect to the microscopic PSF:

1. membrane sheets oriented vertically to the focal xy plane lead to relatively thin membrane profiles with high intensities, since fluorescence signals are integrated along the membrane sheet, collinear to the elongated z axis of the PSF;
2. membrane sheets oriented horizontally to the focal plane lead to thick membrane profiles with relatively low intensities, since the intersection between the membrane sheet and PSF reaches a minimum;
3. membrane sheets oriented diagonally to the xy plane of the PSF, lead to the acquisition of intermediate membrane profiles and signal intensities [Fidorra et al., 2009].

In addition to the geometric constraints, membrane undulations and the dynamic organization of blebs or protrusions add different intensity patterns to the image, and the direct, automated segmentation of cell membranes within the described conditions has not been solved so far [Mosaliganti et al., 2012, Dufour et al., 2017]. For image data shown in Fig. 3.1, Manually Outlined Contours (MOC) are the only choice to obtain a first, rough approximation of cells membranes, especially when the confluence and morphological complexity of the cells prevents the success of automated segmentation (Fig. 3.1A-C). Cell borders cannot be identified unequivocally in all parts of the image, so the definition of a unique ground truth is not possible. The formation of protrusions in different directions, in addition to heterogeneous and weak membrane signals, presents a scenario where only an experienced investigator can take decisions to manually outline the best possible contours (see Section 4.2.3). Naturally, human bias and errors are intrinsically included. In scenarios with missing intensity information, MOC present a possible approximation. In Table 4.2, similarities and differences generated by the three experts are shown for 17 PpO cell contours along 3 z-slice images, producing a total of 153 cell contours. The experts identified an equal number of cells with very similar organization and morphology overall (see A .3 for detailed comparison). The average difference measured for the cell area is below 10%, and for the perimeter, below 8%, from the pairwise comparisons performed upon MOC, Parametric Active Contours (PAC), and ALPACA. The Dice, Jaccard, and NSD indices indicate an equivalent of similarity above 90%, 80%, and 90%, respectively. A Hausdorff Distance of ∼7 pixels (1 µm) also supports a high similarity between MOC, PAC, and ALPACA. In a different scenario, the Expert/Expert variation of MOC was tested, and also the deviation of expert drawings with PAC, and ALPACA within a synthetic, PSF-convolved ground truth image (4.2.2,4.2.3). Figure 4.5 shows 88 hexagons with well-defined areas, edge length and Adjacent Edges (AE $= 0, 1, ...6$); both, MOC and ALPACA contours exhibit almost perfect alignment with the subjacent hexagon borders for all experts (Fig. 4.5B,C). Figure 4.5D shows a nearly perfect correlation of the AE values calculated from ALPACA contours with the ground truth AE values. Morphological and Similarity Indices shown in Supplementary Tables 2/3 indicate nearly perfect match with the ground truth hexagons, and a very low Expert/Expert variation for MOC, PAC, and ALPACA (see A .1 and A .2). The mean differences for area and perimeter are below or equal to 1% for pairwise comparison of expert MOC with the ground truth data. For the Expert/Expert variation of MOC, the mean difference for the quantification of cell area is below 1.5%, and for the perimeter, below 1%. After ALPACA, the mean variations remain similar, but increased standard deviation values are observed in the morphological indices.

For all experts, MOC deviate from the predominantly smooth, curved membrane pattern in different parts of the image (Fig. 3.1B/C, 4.4A/D/G), and overlapping contours cannot be avoided. PAC are a powerful tool for correcting deviations and undulations of manually drawn contours. Well applied GGVF attracts contour vertices towards the intensity profile of the membranes, and contour smoothness is balanced by physical contour properties like elasticity or rigidity. PAC have shown excellent results for the segmentation of contours in different experimental systems and settings [Härtel et al., 2007, Fidorra et al., 2009, Chang et al., 2014, Bustos et al., 2017]. For PpO cells, Figs. 3.1D and 4.4A/D/G show the results of optimized PAC for membrane segmentation 3.2.2, together with the detection of overlapping, adjacent, and non-adjacent sections within the range determined by the selected Adjacency Distance d. The Dice, Jaccard, and NSD values between expert MOC are all within the ∼90%

similarity range for the E1/E2 comparison; 82%, 81% and 92% for the E1/E3 comparison, and 89%, 81% and 93% for the E2/E3 comparison. The measured distance lies below 7 pixels (∼1 µm) for E1/E2, ∼8 pixels (1.1 µm) for E1/E3 and ∼6 pixels (0.9 µm) for the E2/E3. The measured morphological indices for PAC were above 80% for the three comparisons. The measured Similarity Indices lie within 80% and 90%, and the Hausdorff Distance is below 7 pixels (∼1 µm). The rest of the measurements in Table 4.4 show that both PAC and ALPACA preserve this highly small variability between experts within the same range.

The results of ALPACA (Cap. 3, Figs. 4.4,4.3) are shown for two neighboring PpO cells in Fig. 3.7. For adjacent (green), non-adjacent (blue), and overlapping (red) membrane sections, ALPACA calculates a solution for a common shared contour section on the basis of Euclidean distance correspondence vertex mapping (see 3.2.4, Fig. 3.7C/D) and normalized length correspondence vertex mapping (see 3.2.4, Fig. 3.7E/F). As Figs. 3.7E/F show, only the normalized length based correspondence vertex mapping leads to smooth common shared contour sections for adjacent and overlapping membrane sections, and avoids undulations that can be observed at the tips of the sections in selected cases (see representative example in Fig. 3.7C/D). Finally, ALPACA connects the tips of the non-adjacent contour sections to the common shared contour section, and applies piecewise parametric active contour relaxation exclusively to the non-adjacent contours to optimize for smooth transitions between adjacent and non-adjacent contours (Fig. 3.7E/F). From the new contour solution presented in Fig. 3.7G/H, the section length of adjacent vs. non-adjacent membrane sections can be calculated together with morphological descriptors. Angles of the triplet vertices and the corresponding cell contours can be determined by standard fitting of straight lines or circular arcs to a number of contour vertices in proximity to tips (Fig. 3.7H). The improved cell-cell and cell-medium contours also improve the estimation of angles between adjacent cells in 2D and should provide a more solid basis for force inference techniques that allow the estimation of tension maps in 2D and 3D [Veldhuis et al., 2017].

The free parameters of the active contour approach permit to optimize contours for a plurality of shapes, and could be trained to fit *in vivo* imaging data of cellular membranes. However, there is no available ground truth for the exact localization of the membrane sheets that would allow to define unique performance indicators, such as the Hausdorff distance or the Dice coefficient [Chang et al., 2014] for the contours or the segmented ROIs. The proposed series of quality indicators aims to characterize shared and final cell contour sections (Fig. 4.1/4.2). Fig. 4.1 shows that distance (4.1A) and curvature (4.1B) of the shared contour section are balanced with respect to the adjacent and overlapping contour sections. The differences of the distance indicators that compare the shared contour section to each of the original contour sections are within the size of the symbols used in the plot except for the first two vertex positions (compare Fig. 4.1A with Fig. 3.7E/F). The curvature plot of the shared contour section calculated with the normalized length based correspondence vertex mapping with respect to each of the original contour sections (Fig. 4.1B) shows that the curvature of the shared contour section remains within the curvature limits of the original contour sections. A bias towards either one of the original contour section curvatures cannot be observed. It is impossible, however, to provide a perfect match of the shared contour section with respect to the distance and the curvature, since position and curvature are not independent parameters. However, the visual impression of the position of the vertices (Fig. 3.7E-H) combined with the subjective quality indicators for distance and curvature (Fig. 4.1)

satisfy the expectations within this test for shared cell contours in general. The variation of morphological indices was measured for the ROI contours with dependence of the Adjacency Distance d. Figure 4.2 and Table 4.1 present the deviations of a total of seven morphological features of PpO cells after the application of ALPACA with selected Adjacency Distance values $d = 83, 166, 332$, and 498 nm, relative to the features of the cell contours before the adjacency correction (see 4.1.1).

The relative area and perimeter variations start below 1, which is expected for ROIs with highly overlapping contours (red contour sections in Fig. 4.4), and tend to rise slightly with increasing d. This can be explained by the adjacency condition established by ALPACA at the interface of adjacent and non-adjacent contour sections. First, the adjacency condition forces the shared contour to balance the positions of both adjacent contour sections (Fig. 3.7E-H). This leads to shorter shared contour sections relative to both adjacent contour sections (compare Fig. 3.7E-H to Fig. 4.1 and Table 4.1). When d increases, the smoothness condition for the non-adjacent contours at the tips of the shared sections starts to add length to the contours. However, the increase is marginal within the tested range for d with respect to the overall contour morphology (Fig. 4.1, Table 4.1). The relative increase in ROIs with short non-adjacent sections is higher, up to $\sim 20\%$ (data not shown). All further morphological indices: Section Distance (Sim_D), Section Length (Sim_L), Average Segment Length (Sim_{ASL}), and Section Curvature (Sim_K) show deviations from the mean values below 10% with respect to the original contour sections (Fig. 4.2). The indices increment with increasing d, which does not surprise, since the adjacent contour sections enlarge with d. A small number of outliers appear for the Section Curvature index, for short contour sections of dissimilar shapes whose adjusted shared section is not always able to compensate equally (not shown).

Apart from the parameters of the active contour approach (see 3.2.2), the Adjacency Distance d is the only free parameter within ALPACA. Considering the varying conditions for *in vivo* experiments with cells, tissue, or organisms, and the heterogeneous geometries of membrane sheets and the PSFs of different microscopy techniques, there is no unique recommendation for the selection of d: its value needs to respond to the acquisition limits and the quality of the ROI contours of an automated or manually approach for $C_{\mathrm{i}}(x, y)$. Fig. 4.3 shows the detection of adjacent and non-adjacent cellular membranes within an Adjacency Distance $d = 83$ nm, and the solution calculated by the algorithm. This condition for d corresponds to $\sim$1.66$\times$ the recommended sampling distance for the image acquisition in the xy plane ($d = 50$ nm). The visual perception of the solution for the cell contours $C_{\mathrm{i}}^{**}(x, y)$ is convincing and does not rise additional questions beyond the responses to the initial experimental challenge. Since variations of the morphological features in response to ALPACA are relatively small within the tested range for d, the researcher has to take a decision based on the visual perception and the tolerated variation of morphological features in response to the specific scientific question. In the absence of ground truth for adjacency, different solutions for d near the resolution limit should be tested and analyzed, and results can be reported for a single d value or a range to evidence the robustness of the calculated data for adjacent and non-adjacent sections.

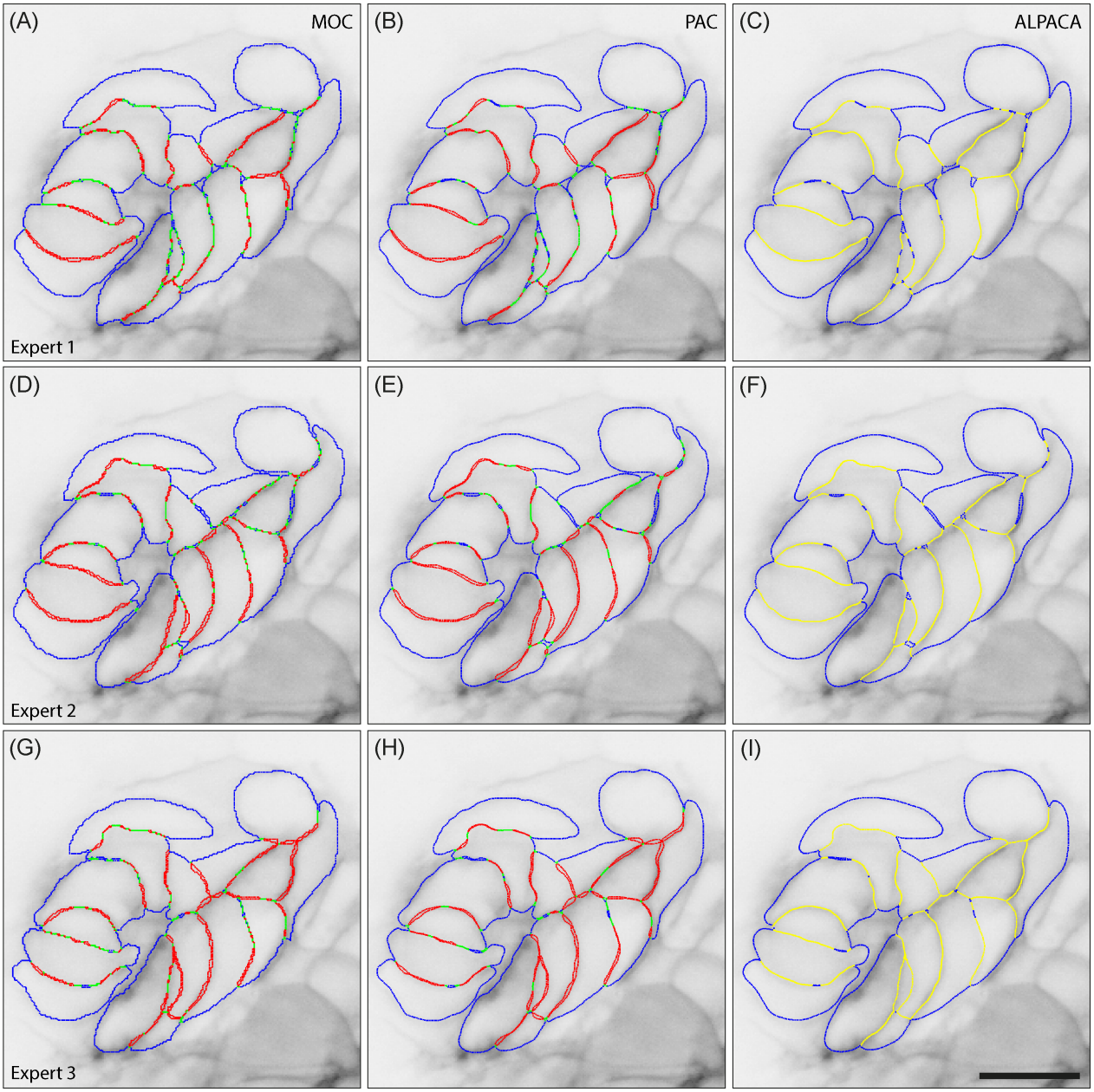

Figure 4.4: Expert/Expert variations (Experts E1,E2,E3) of Manually Outlined Contours (MOCs, panels A/D/G), optimized Parametric Active Contours (PACs, panels B/E/H), and ALPACA (panels C/F/I) of 17 PpO cells from Fig. 3.1. A representative z-slice from a 3D stack is shown. For MOC/PAC overlapping (red), adjacent (green), and non-adjacent (blue) contour sections are shown for an Adjacency Distance $d = 83\,\mathrm{nm}$. For ALPACA, adjacent (yellow) and non-adjacent (blue) contour sections are shown. Scale bar is 10 µm.Published in [Jara-Wilde et al., 2020].

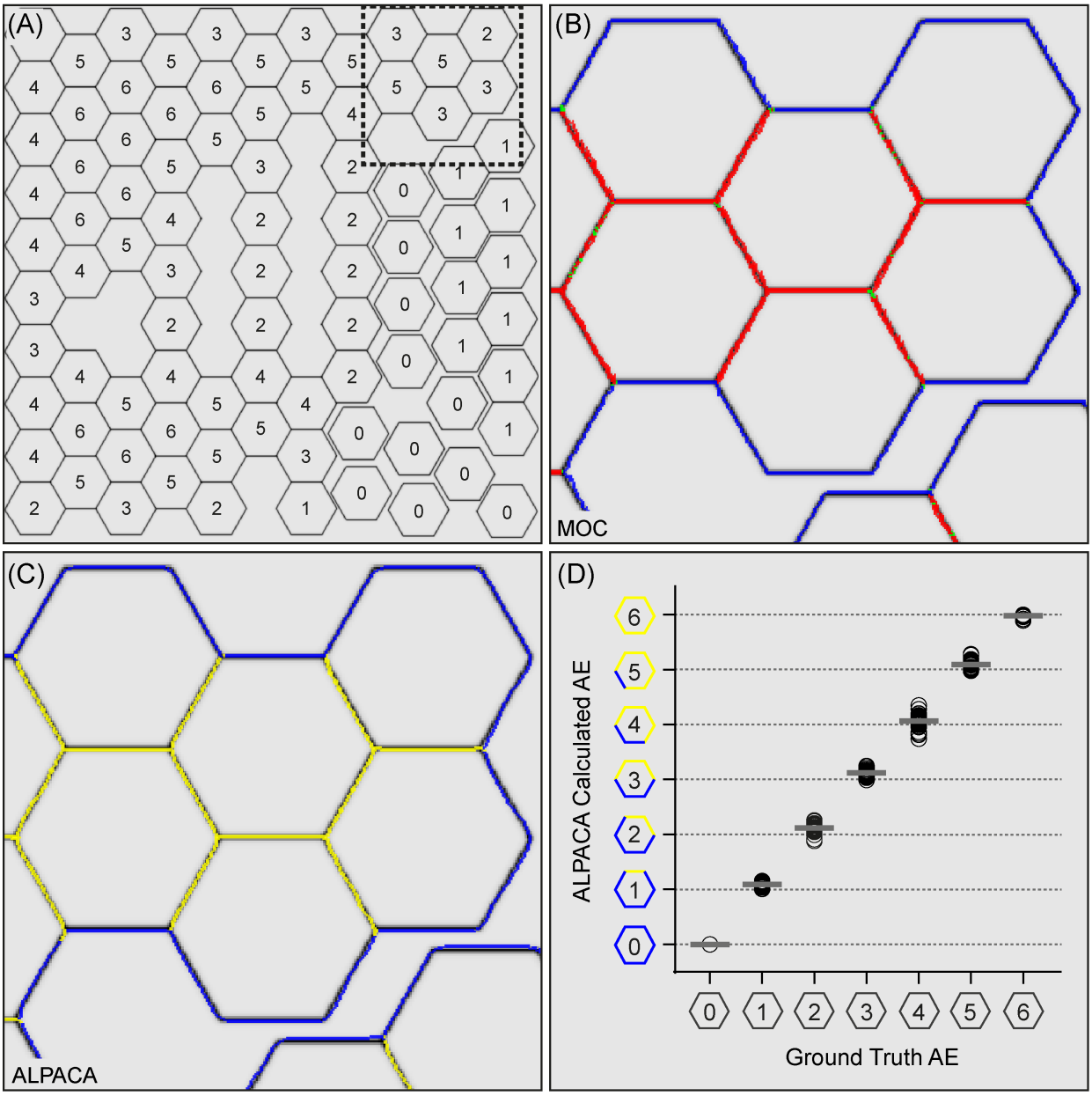

Figure 4.5: Adjacent and non-adjacent sections calculated by ALPACA for manually outlined ROI contours in synthetic test. (A) Synthetic image with 88 hexagons (4.2.2); intensities are shown in inverted grey scale. The number of Adjacent Edges (AE $= 0 - 6$) is indicated for each hexagon. (B/C) Detail of the hexagons from the dashed square in (A). (B) Manually Outlined Contours (MOC) of one representative expert with overlapping (red), adjacent (green), and non-adjacent (blue) contour sections for an Adjacency Distance $d = 1$ pixel. (C) ALPACA defines adjacent (yellow) and non-adjacent (blue) contour sections. All experts yield similar contour quality. (D) Aligned scatter plot of AE calculated by ALPACA vs. Ground Truth AE. Open circles represent data adjusted from three expert MOC for each hexagon. AE values (y axis) were calculated as the ratio between the adjacent contour length and the total contour length, multiplied by 6. The grey lines indicate mean values. Calculated mean $\pm$ standard deviation values: 0 ± 0 (0 AE); 1.09 ± 0.04 (1 AE); 2.12 ± 0.08 (2 AE); 3.12 ± 0.05 (3 AE); 4.07 ± 0.12 (4 AE); 5.09 ± 0.07 (5 AE); 5.98 ± 0.02 (6 AE). Published in [Jara-Wilde et al., 2020].

Table 4.1: Variations of Morphological Indices for increasing Adjacency Distance d. 17 PpO cell membrane contours along three z-slices were measured from ALPACA, upon the MOC of three independent experts, totaling $n_1 = 153$ contours. The number of shared sections (n_2) varies according to the Adjacency Distance d (see 3.2.4, 4.1.1). Mean ± Standard Deviation/Standard Error values are shown, with the maximum and minimum values highlighted in dark and light grey, respectively. RAV: Relative Area Variation, RPV: Relative Perimeter Variation, RALV: Relative Adjacent Length Variation, RNALV: Relative Non-Adjacent Length Variation.

Index	$d = 83$ nm $n_1 = 3 \times 51$ $n_2 = 294$	$d = 166$ nm $n_1 = 3 \times 51$ $n_2 = 265$	$d = 332$ nm $n_1 = 3 \times 51$ $n_2 = 281$	$d = 498$ nm $n_1 = 3 \times 51$ $n_2 = 152$
RAV (n_1)	0.969 ± 0.0031/0.003	0.978 ± 0.032/0.003	0.996 ± 0.010/0.001	0.994 ± 0.039/0.003
RPV (n_1)	0.924 ± 0.028/0.002	0.936 ± 0.028/0.002	1.005 ± 0.008/0.001	0.960 ± 0.039/0.003
RALV (n_1)	0.882 ± 0.058/0.005	0.941 ± 0.017/0.004	0.986 ± 0.051/0.004	0.952 ± 0.049/0.004
RNALV (n_1)	0.969 ± 0.031/0.003	0.923 ± 0.143/0.012	1.082 ± 0.351/0.028	1.034 ± 0.217/0.018
Sim_D (n_2)	0.965 ± 0.068/0.004	0.962 ± 0.057/0.003	0.952 ± 0.044/0.003	0.958 ± 0.043/0.004
Sim_L (n_2)	0.993 ± 0.024/0.001	0.993 ± 0.031/0.002	0.997 ± 0.016/0.001	0.995 ± 0.024/0.002
Sim_{Kd} (n_2)	0.944 ± 0.090/0.005	0.944 ± 0.084/0.005	0.914 ± 0.095/0.006	0.916 ± 0.096/0.008
Sim_{ASL} (n_2)	0.997 ± 0.019/0.001	0.989 ± 0.017/0.001	0.972 ± 0.041/0.003	0.971 ± 0.039/0.003

Table 4.2: Morphological Indices for cell area and perimeter (NAD: Normalized Area Difference, NPD: Normalized Perimeter Difference) and Similarity Indices (Dice, Jaccard, NSD: Normalized Sum of Distances, HD: Hausdorff Distance) for three independent experts (E1/E2/E3) for $n = 51$ PpO cells from a complete 3D stack. Indices were calculated pairwise for E1, E2, and E3, for Manually Outlined Contours (MOC), Parametric Active Contours (PAC), and ALPACA. Mean ± Standard Deviation values are shown, with the maximum and minimum values highlighted in dark and light grey, respectively. Morphological Indices were calculated as described in 4.1.1; Similarity Indices were calculated as described in 4.1.2.

	MOC			PAC			ALPACA		
	E1/E2	E1/E3	E2/E3	E1/E2	E1/E3	E2/E3	E1/E2	E1/E3	E2/E3
NAD	0.082 ±0.060	0.098 ±0.080	0.090 ±0.084	0.084 ±0.061	0.099 ±0.081	0.091 ±0.086	0.075 ±0.054	0.095 ±0.082	0.086 ±0.083
NPD	0.065 ±0.049	0.077 ±0.053	0.064 ±0.049	0.060 ±0.048	0.079 ±0.055	0.066 ±0.049	0.062 ±0.048	0.078 ±0.054	0.066 ±0.048
Dice	0.903 ±0.041	0.895 ±0.052	0.897 ±0.055	0.904 ±0.039	0.896 ±0.051	0.897 ±0.053	0.898 ±0.093	0.896 ±0.056	0.885 ±0.120
Jaccard	0.825 ±0.065	0.814 ±0.079	0.817 ±0.080	0.827 ±0.062	0.814 ±0.077	0.817 ±0.079	0.837 ±0.055	0.816 ±0.083	0.823 ±0.078
NSD	0.066 ±0.059	0.082 ±0.107	0.069 ±0.074	0.063 ±0.056	0.082 ±0.107	0.068 ±0.074	0.058 ±0.048	0.082 ±0.114	0.067 ±0.075
HD	6.345 ±4.051	6.811 ±3.948	5.962 ±2.609	6.096 ±4.061	6.558 ±4.196	5.729 ±2.631	6.053 ±4.085	6.501 ±4.141	5.748 ±2.631
HD [nm]	1053 ±672.5	1131 ±655.4	989.6 ±433.0	1012 ±674.1	1089 ±696.5	951.1 ±436.8	1048.8 ±678.1	1079.2 ±687.4	954.1 ±436.9

Table 4.3: Morphological Indices for cell area and perimeter (NAD, NPD) and Similarity Indices for three independent experts (E1/E2/E3) against Ground Truth (GT) for $n = 88$ synthetic hexagonal cells. Indices were calculated pairwise for GT against E1, E2, and E3, for Manually Outlined Contours (MOC), Parametric Active Contours (PAC), and ALPACA. Mean ± Standard Deviation values are shown, with the maximum and minimum values highlighted in dark and light grey, respectively.

	MOC			PAC			ALPACA		
	GT/E1	GT/E2	GT/E3	GT/E1	GT/E2	GT/E3	GT/E1	GT/E2	GT/E3
NAD	0.006 ±0.006	0.010 ±0.007	0.010 ±0.008	0.014 ±0.013	0.023 ±0.011	0.026 ±0.012	0.027 ±0.107	0.032 ±0.110	0.041 ±0.148
NPD	0.005 ±0.004	0.007 ±0.005	0.006 ±0.004	0.005 ±0.007	0.011 ±0.006	0.010 ±0.006	0.049 ±0.103	0.058 ±0.113	0.067 ±0.147
Dice	0.991 ±0.004	0.988 ±0.003	0.986 ±0.004	0.993 ±0.007	0.988 ±0.006	0.987 ±0.006	0.987 ±0.004	0.974 ±0.104	0.984 ±0.003
Jaccard	0.982 ±0.007	0.976 ±0.006	0.972 ±0.007	0.986 ±0.013	0.977 ±0.011	0.973 ±0.012	0.974 ±0.007	0.970 ±0.007	0.968 ±0.006
NSD	0.001 ±0.000	0.001 ±0.000	0.001 ±0.000	0.001 ±0.001	0.002 ±0.001	0.002 ±0.001	0.0009 ±0.0005	0.001 ±0.0005	0.001 ±0.0004
HD	1.497 ±0.425	1.673 ±0.371	1.811 ±0.408	1.715 ±0.535	2.065 ±0.518	2.110 ±0.406	1.882 ±0.445	1.948 ±0.334	2.087 ±0.427

Table 4.4: Morphological Indices for cell area and perimeter (NAD, NPD) and Similarity Indices for three independent experts (E1/E2/E3) for $n = 88$ synthetic hexagonal cells. Indices were calculated pairwise for the experts, for Manually Outlined Contours (MOC), Parametric Active Contours (PAC), and ALPACA. Mean ± Standard Deviation values are shown, with the maximum and minimum values highlighted in dark and light grey, respectively.

	MOC			PAC			ALPACA		
	E1/E2	E1/E3	E2/E3	E1/E2	E1/E3	E2/E3	E1/E2	E1/E3	E2/E3
NAD	0.010 ±0.008	0.011 ±0.007	0.012 ±0.008	0.015 ±0.010	0.017 ±0.011	0.013 ±0.010	0.010 ±0.009	0.009 ±0.007	0.010 ±0.008
NPD	0.009 ±0.006	0.007 ±0.006	0.008 ±0.007	0.009 ±0.006	0.010 ±0.006	0.008 ±0.005	0.023 ±0.023	0.023 ±0.029	0.016 ±0.019
Dice	0.986 ±0.003	0.986 ±0.004	0.986 ±0.003	0.988 ±0.005	0.987 ±0.005	0.989 ±0.005	0.973 ±0.116	0.972 ±0.227	0.974 ±0.116
Jaccard	0.973 ±0.006	0.972 ±0.007	0.972 ±0.006	0.976 ±0.010	0.974 ±0.010	0.978 ±0.009	0.960 ±0.116	0.959 ±0.120	0.961 ±0.119
NSD	0.001 ±3.8E-04	0.001 ±4.8E-04	0.001 ±3.9E-04	0.001 ±6.3E-04	0.001 ±6.2E-04	0.001 ±5.9E-04	0.001 ±2.9E-04	0.001 ±4.0E-04	0.001 ±4.0E-04
HD	1.893 ±0.417	1.885 ±0.393	2.037 ±0.368	2.092 ±0.408	2.125 ±0.281	1.986 ±0.341	2.098 ±0.550	2.179 ±0.595	1.866 ±0.606

4.4 Alternative Approaches

In this section, a qualitative comparison is provided for approaches that can be regarded as similar or alternatives to ALPACA.

The ALPACA approach combines parametric contours with algorithms for detection, adjustment and connection of shared/non shared contour sections, and relies on polygon interpolation, proximity and intersection computations. In consequence, there are manifold possible ways to evaluate its final or intermediate results against alternative approaches. In addition, a proper comparison between ALPACA and other approaches requires implementations over the same (or at least equivalent) numerical and algorithm basic functions, in terms of numerical schemes, data structures, algorithm optimizations, programming languages, code libraries, and parameter settings, which would add an amount of coding and testing far beyond the scope of this work[2]. An example of such complexity can be found in our comparison of discrete differential operators for an established optical flow algorithm [Delpiano et al., 2012], together with numerical solvers, test data sets, and other algorithms available with our open-access implementation [Jara-Wilde et al., 2015]).

Among the surveyed approaches (see 2.2, 2.3, Table 2.1), the ones selected as suitable to compare address the detection and/or adjustment of adjacent ROI contours, although they do not necessarily with the same or equivalent steps defined in ALPACA. The selected approaches are:

- **T-snakes** [McInerney and Terzopoulos, 1995b]. The T-snakes approach provides a parametric contour model with image vector fields, together with algorithms for contour interpolation, and adjacency detection (intersections only), which makes it similar to ALPACA. There is no published implementation of the authors' method, although two versions have been developed by others:
  - A custom prototype that combines T-snakes with gradient vector flow fields has been published [Olmos, 2009]. Its implementation written in C could be extended and adapted, but the implemented active contour coefficient values are not directly comparable with the conventional snakes model.
  - A C++ implementation within an open-source framework [Namías et al., 2016][3] (see the Deformable Model Array below).

  Within the T-snake approach, however, here is no definition of shared sections, yet the rules to merge or split ROI contours could be expanded to include it.
- **3D Active Meshes** [Dufour et al., 2011]. Available in 3D as a plug-in for the Icy bioimaging software [de Chaumont et al., 2012][4], written in Java language. Defines parametric ROI contour models as 3D surface meshes (not directly comparable with 2D polygons) within an active contour approach that includes contour and image intensity features (requires adaptation to be compared with ALPACA), and the contours are checked for intersections (similar to the detection of shared sections in ALPACA).

[2]Only the ALPACA implementation, which is mostly written in a high-level programming language, has about fifteen thousand lines of source code, not counting the active contour approach and post-processing data collection scripts. Other software packages such as RACE have a code base of similar size.

[3]`https://www.cifasis-conicet.gov.ar/namias/Files/Filters/T-Snake.tar.gz`

[4]`http://icy.bioimageanalysis.org/plugin/3d-active-meshes/`

However, instead of defining shared sections, this approach defines a repulsion force that separates the adjacent ROI contour sections which have no influence/dependency on each other for adjusting their shape. Nevertheless, a modified algorithm could be defined to quantify and adjust them, by specifically addressing the optimization and contour models.

- **ACME** [Mosaliganti et al., 2012]. Implemented as open-source, available in C++[5]. It detects membrane sheets over the input image using membrane intensity models (instead of the gradient vector fields used in ALPACA) and without needing contour models of each ROI, no difference in the detection of adjacent and non-adjacent contours (other than the intrinsic fluorescence signal changes that can be expected). This approach avoids the issue of adjacency detection and correction, but the ROI contours have to be retrieved and quantified with additional, separate steps.
- **CellFit/CellFit-3D** [Brodland et al., 2014, Veldhuis et al., 2017]. Source code and implementation details were not published, but a Windows executable application is available for download[6]. These approaches define parametric contour models which detect adjacency and shared sections between two or more ROIs, and dedicated interaction rules for them. To be comparable with ALPACA, they require the addition of intensity gradient vector fields, which appears to be straightforward given the data structures and algorithm steps defined.
- **Deformable Model Array** [Namías et al., 2016]. Implementation available[7] in C++ source code, relying on the ITK library [Yoo et al., 2002, McCormick et al., 2014][8] for standard image processing functions. Highly similar approach in terms of contour model and adjustment steps (T-snakes and GVF snakes), which could be adapted to include or implement ALPACA for comparison, but does not include a shared section definition and posterior steps.
- **RACE** (2D/3D) [Stegmaier et al., 2016]. Implemented as open-source in C++ and CUDA, with ITK library functions. A combined use of image filters and watershed transforms (instead of intensity gradient vector fields) enhance the membrane signals (including adjacent membranes) for segmentation before the detection of ROI contours. To compare it with ALPACA, the quantification of shared sections needs to be added.

[5] `https://github.com/krm15/ACME`
[6] `http://www.civil.uwaterloo.ca/brodland/cellFIT.html`
[7] `https://www.cifasis-conicet.gov.ar/namias/Files/Filters/DMA_Framework_Qt5.tar.gz`
[8] `https://itk.org`

Overall, the presented alternatives and ALPACA are conceived within a similar context of biomedical imaging (and fluorescence microscopy for many of them), and address the problem of segmenting ROIs with shared boundaries. However, they do it by defining different contour models and constraints for the solution. Also, they are defined with different steps and parameters, in addition to several implementation and optimization choices that, despite being justifiable, prevent or hinder an experimental and direct comparison experiment between the models and constraints of each approach in addition to their quality and efficiency indices. Nevertheless, the main distinctive features of ALPACA can be stated from a qualitative perspective as:

- **Explicitly defined shared contour sections**. Shared sections are parametric contours too, suitable for adjustment and connection steps, which were defined to preserve shape and/or image features of the ROIs that originate them.
- **Connection rules for shared and non-shared contour sections**. Each adjusted shared section becomes part of the final contour of two ROIs, each of them subject to further adjustment and connection rules for shared and non-shared contour sections.

Chapter 5

Conclusion

5.1 General Remarks

In this work, a 2D parametric contour model was used as the basis for the pairwise detection and adjustment of shared contour sections of neighboring ROIs. The ALgorithm for Piecewise Adjacent Contour Adjustment ALPACA receives an Adjacency Distance d as input parameter, in order to use it as a threshold for detecting adjacent ROI contour sections. ALPACA also detects overlapping contour sections, and merges them with existing adjacent sections in order to define shared contour sections that set a common boundary for neighboring ROIs. Finally, the shared sections are connected to the non-adjacent sections which are adjusted to ensure morphological consistency of the final contour by applying a piecewise parametric active contour optimization.

The parametric active contour model allows to reduce pixel-level shape irregularities, as well as contour undulations that can naturally occur in manual outlines. ALPACA introduces the handling of proximal and overlapping contour sections from different ROIs: it detects adjacent, non-adjacent, and overlapping 2D sections within a selected Adjacency Distance d, calculates shared sections in replacement to adjacent and overlapping contour sections of neighboring ROIs with minimum shape alterations, and presents piecewise active contour solutions for each pair of ROIs which share one or more sections with shape preserving contour properties at the tips of the shared sections and the overall cell morphology. ALPACA can be integrated with different methods for contour adjustment to handle non-adjacent sections, either as pre- or post-processing stages, or within a mixed approach of non-adjacent/adjacent contour adjustment, allowing, for example, the appearance or disappearance of shared sections (as in the case of motion estimation or simulations for time-lapse experiments).

The presented approach presents a solution to correct and quantify adjacent contours in the xy plane, the optimized 2D contours can set the basis to improve the representation of cells as 3D surfaces, the determination of forces, or the tracking of contours in combination with (or in parallel to) previously published approaches (see 3.3, 4.4, [Mosaliganti et al., 2012, Mashburn et al., 2012, Veldhuis et al., 2017]).

5.2 Future Work

Detection and Handling of Corner/Junction Points for Three or More ROIs Intersecting shared sections from more than two ROI contours can appear due to natural arrangements of cell aggregates that produce junction points, and/or shared sections that could be determined by more than two adjacent contour sections. This can also occur due to large values of d that further extend the adjacency range, potentially covering several junction points. While the detection of such points can be achieved with a procedure equivalent to the pairwise ROI adjacency detection, the replacement of one or more contour sections from a single ROI containing a variable number of corners results in a non-trivial connectivity problem for piecewise contours. In addition, the estimation of junction points needs to take into account image and contour shape features that ensure consistency with the parametric active contour approach, in order to yield morphologically consistent ROI contours. Established approaches [Brodland et al., 2014, Veldhuis et al., 2017] can serve as a basis for defining an extended version of the correspondence vertex list approach presented in this thesis.

Extension to 3D A natural extension for real experiments and data sets is to extend the ALPACA approach to 3D segmentation and quantification. To this end, at least two different strategies can be perused: (i) segmenting 2D image slices from a 3D stack, and then merge the obtained ROIs in order to generate a final 3D segmentation, as in some state of the art software tools such as RACE [Stegmaier et al., 2016]; or (ii) to directly extend the boundary models and detection algorithms for 3D geometries, by using surface boundary models such as polygon meshes, akin to the active meshes approach [Dufour et al., 2011]. We already implemented and started to apply 3D descriptors to neurons in developing fish embryos [Lemus et al., 2017, Lemus et al., 2021], and also 3D optimization algorithms for quantifying the localization of DNA replication sites within culture cells [Liddle et al., 2014].

Segmentation in Time Series Live imaging experiments often require the analysis of dynamic events of change form and organization changes at different levels, in processes involving cell (*e.g.* migration in tissue development or wound healing) or intracellular dynamics of organelles. To this end, tracking and motion estimation approaches have been developed [Rabut and Ellenberg, 2004, Dufour et al., 2005, Nath et al., 2006, Wang et al., 2007, Dzyubachyk et al., 2007, Meijering et al., 2009, Chowdhury et al., 2010, Mikula et al., 2011, Meijering et al., 2012, Sacan et al., 2008, Amat et al., 2014]. In particular, contributions in proper implementation and parameter settings of optical flow have been made in parallel to this work by the author [Delpiano et al., 2012, Jara-Wilde et al., 2015] Their integration with a segmentation approach like ALPACA will provide the necessary image tools that, combined with those from biomedical sciences, will deepen the understanding of the interplay between form and function at different levels, in scenarios of physiology, disease/healing, and others.

Computation Enhancements The ALPACA computation time depends mainly on the exhaustive segment-segment distance computation between ROI contours; it scales in quadratic proportion with respect to the average segment (or vertex) count of the input ROI set. Memory usage scales linearly with respect to the image and contour size. The use of adaptive algorithm design and analysis techniques for ALPACA can lead to better performing algorithms both in sequential and concurrent computing schemes, regarding specific problem instances with particular features of the input and/or output (*e.g.* output-sensitive algorithms).

Possible approaches to consider for computation improvements in ALPACA include:

- Time and memory efficient linear algebraic equation solvers for the parametric active contour adjustment based on n-diagonal matrices, avoiding complete matrix decomposition operations.
- Broadband adjacency checking using adaptive convex hull algorithms (output-dependent complexity) can lower the theoretical bounds of computation time in algorithms with input-dependent complexity; also narrow band and compression approaches for distance computations and/or level set methods (see 2.2.1,2.2.2) can be regarded as adaptive, since computations and storage are performed selectively according to the solution at a given iteration, instead of the whole image, reducing the computation times for the level set function adjustment.

Bibliography

[Abbe, 1873] Abbe, E. (1873). Beiträge zur Theorie des Mikroskops und der mikroskopischen Wahrnehmung. *Archiv für mikroskopische Anatomie*, 9:413–418.

[Abufadel et al., 2008] Abufadel, A., Yezzi, A. J., and Schafer, R. W. (2008). 4D segmentation of cardiac data using active surfaces with spatiotemporal shape priors. In *Applied Pattern Recognition*, pages 77–100. Springer-Verlag, Berlin - Heidelberg.

[Adalsteinsson and Sethian, 1995] Adalsteinsson, D. and Sethian, J. A. (1995). A fast level set method for propagating interfaces. *Journal of Computational Physics*, 118:269–277.

[Aigouy et al., 2010] Aigouy, B., Farhadifar, R., Staple, D. B., Sagner, A., Röper, J.-C., Jülicher, F., and Eaton, S. (2010). Cell flow reorients the axis of planar polarity in the wing epithelium of drosophila. *Cell*, 142:773–786.

[Amat et al., 2014] Amat, F., Lemon, W., Mossing, D. P., McDole, K., Wan, Y., Branson, K., Myers, E. W., and Keller, P. J. (2014). Fast, accurate reconstruction of cell lineages from large-scale fluorescence microscopy data. *Nature Methods*, 11(9):951–958.

[Antony et al., 2013] Antony, P. M. A., Trefois, C., Stojanovic, A., Baumuratov, A. S., and Kozak, K. (2013). Light microscopy applications in systems biology: opportunities and challenges. *Cell Communication and Signaling*, 11(1):1–19.

[Atallah, 1983] Atallah, M. J. (1983). A linear time algorithm for the Hausdorff distance between convex polygons. *Information Processing Letters*, 17:207–209.

[Aubert and Kornprobst, 2006] Aubert, G. and Kornprobst, P. (2006). *Mathematical Problems in Image Processing: Partial Differential Equations and the Calculus of Variations*, volume 147 of *Applied Mathematical Sciences*. Springer, New York, NY, 2nd edition.

[Baker et al., 2011] Baker, S., Scharstein, D., Lewis, J. P., Roth, S., Black, M. J., and Szeliski, R. (2011). A database and evaluation methodology for optical flow. *International Journal of Computer Vision*, 92(1):1–31.

[Ballard, 1981] Ballard, D. (1981). Generalizing the Hough transform to detect arbitrary shapes. *Pattern Recognition*, 13:111–122.

[Barrett, 2015] Barrett, S. (2015). Image SXM. Freeware web-downloadable application.

[Beckmann et al., 1990] Beckmann, N., Kriegel, H.-P., Schneider, R., and Seeger, B. (1990).

The R*-tree: an efficient and robust access method for points and rectangles. In *Proceedings of the 1990 ACM SIGMOD international conference on Management of data - SIGMOD '90*, pages 322–331.

[Bengtsson, 2014] Bengtsson, E. (2014). Quantitative and automated microscopy - where do we stand after 80 years of research? In *Proceedings of the IEEE 11th International Symposium on Biomedical Imaging (ISBI)*, pages 274–277.

[Bentley, 1975] Bentley, J. L. (1975). Multidimensional binary search trees used for associative searching. *Communications of the ACM*, 18(9):509–517.

[Bergeest and Rohr, 2012] Bergeest, J.-P. and Rohr, K. (2012). Efficient globally optimal segmentation of cells in fluorescence microscopy images using level sets and convex energy functionals. *Medical Image Analysis*, 16(7):1436–1444.

[Bertrand, 2005] Bertrand, G. (2005). On topological watersheds. *Journal of Mathematical Imaging and Vision*, 22(2):217–230.

[Betzig et al., 2006] Betzig, E., Patterson, G., Sougrat, R., Lindwasser, O., Olenych, S., Bonifacino, J., Davidson, M., Lippincott-Schwartz, J., and Hess, H. (2006). Imaging intracellular fluorescent proteins at nanometer resolution. *Science*, 313(5793):1642–1645.

[Beucher and Lantuéjoul, 1979] Beucher, S. and Lantuéjoul, C. (1979). Use of watersheds in contour detection. In *Proceedings of the International Workshop in Image Processing CCETT/IRISA, Rennes, France*.

[Bhanu and Talbot, 2015] Bhanu, B. and Talbot, P., editors (2015). *Video Bioinformatics: From Live Imaging to Knowledge*, chapter Video Bioinformatics Methods for Analyzing Cell Dynamics: A Survey, pages 13–56. Springer International Publishing, Cham.

[Bogovic et al., 2013] Bogovic, J. A., Prince, J. L., and Bazin, P.-L. (2013). A multiple object geometric deformable model for image segmentation. *Computer Vision and Image Understanding*, 117:145–157.

[Boost, 2017] Boost (2017). Boost C++ Libraries. [online] `http://www.boost.org/`. [Access: January 21, 2019].

[Bosveld et al., 2012] Bosveld, F., Bonnet, I., Guirao, B., Tlili, S., Wang, Z., Petitalot, A., Marchand, R., Bardet, P.-L., Marcq, P., Graner, F., and Bellaïche, Y. (2012). Mechanical control of morphogenesis by fat/dachsous/four-jointed planar cell polarity pathway. *Science*, 336:724–727.

[Bourgine et al., 2010] Bourgine, P., Čunderlík, R., Drblíková-Stašová, O., Mikula, K., Remešíková, M., Peyriéras, N., Rizzi, B., and Sarti, A. (2010). 4D embryogenesis image analysis using PDE methods of image processing. *Kybernetika*, 46(2):226–259.

[Braden, 1986] Braden, B. (1986). The surveyor's area formula. *The College Mathematics Journal*, 17(4):326–337.

[Bridson, 2003] Bridson, R. E. (2003). *Computational aspects of dynamic surfaces*. PhD thesis, Stanford University.

[Brodland et al., 2014] Brodland, G. W., Veldhuis, J. H., Kim, S., Perrone, M., Mashburn, D., and Hutson, M. S. (2014). CellFIT: A cellular force-inference toolkit using curvilinear cell boundaries. *PLoS One*, 9(6):1–15.

[Bruhn and Weickert, 2005] Bruhn, A. and Weickert, J. (2005). Lucas/kanade meets horn/schunck: Combining local global optic flow methods. *International Journal of Computer Vision*, 61(3):211–231.

[Bruhn et al., 2002] Bruhn, A., Weickert, J., and Schnörr, C. (2002). Combining the advantages of local and global optic flow methods. In *Joint Pattern Recognition Symposium*, pages 454–462, Berlin, Heidelberg. Springer.

[Bustos et al., 2017] Bustos, F. J., Ampuero, E., Jury, N., Aguilar, R., Falahi, F., Toledo, J., Ahumada, J., Lata, J., Cubillos, P., Henríquez, B., Guerra, M. V., Stehberg, J., Neve, R. L., Inestrosa, N. C., Wyneken, U., Fuenzalida, M., Härtel, S., Sena-Esteves, M., Varela-Nallar, L., Rots, M. G., Montecino, M., and van Zundert, B. (2017). Epigenetic editing of the Dlg4/PSD95 gene improves cognition in aged and Alzheimer's disease mice. *Brain*, 140(12):3252–3268.

[Canny, 1986] Canny, J. (1986). A computational approach to edge detection. *IEEE Transactions on Pattern Analysis and Machine Intelligence*, 8(6):679–698.

[Castañeda et al., 2014] Castañeda, V., Cerda, M., Santibáñez, F., Jara, J., Pulgar, E., Palma, K., Lemus, C. G., Concha, M. L., and Härtel, S. (2014). Computational methods for analysis of dynamic events in cell migration. *Current Molecular Medicine*, 14:291–307.

[Chan and Vese, 2001] Chan, T. F. and Vese, L. (2001). An active contour model without edges. *IEEE Transactions on Image Processing*, 10:266–277.

[Chang et al., 2015] Chang, H., Wen, Q., and Parvin, B. (2015). Coupled segmentation of nuclear and membrane-bound macromolecules through voting and multiphase level set. *Pattern Recognition*, 48:882–893.

[Chang et al., 2014] Chang, V., Saavedra, J., Castaneda, V., Sarabia, L., Hitschfeld, N., and Härtel, S. (2014). Gold-standard and improved framework for sperm head segmentation. *Computer Methods and Programs in Biomedicine*, 117:225–237.

[Chiang et al., 1998] Chiang, Y.-J., Silva, C. T., and Schroeder, W. J. (1998). Interactive out-of-core isosurface extraction. *Visualization Conference, IEEE*, 0:167–174.

[Ching et al., 2018] Ching, T., Himmelstein, D. S., Beaulieu-Jones, B. K., Kalinin, A. A., Do, B. T., Way, G. P., Ferrero, E., Agapow, P.-M., Zietz, M., Hoffman, M. M., Xie, W., Rosen, G. L., Lengerich, B. J., Israeli, J., Lanchantin, J., Woloszynek, S., Carpenter, A. E., Shrikumar, A., Xu, J., Cofer, E. M., Lavender, C. A., Turaga, S. C., Alexandari, A. M., Lu, Z., Harris, D. J., DeCaprio, D., Qi, Y., Kundaje, A., Peng, Y., Wiley, L. K., Segler, M. H. S., Boca, S. M., Swamidass, S. J., Huang, A., Gitter, A., and Greene, C. S. (2018).

Opportunities and obstacles for deep learning in biology and medicine. *Journal of the Royal Society Interface*, 15(141):20170387.

[Chowdhury et al., 2010] Chowdhury, A. S., Chatterjee, R., Ghosh, M., and Ray, N. (2010). Cell tracking in video microscopy using bipartite graph matching. In *20th International Conference on Pattern Recognition (ICPR)*, pages 2456–2459.

[Clausen et al., 2017] Clausen, M., Colin-York, H., Schneider, F., Eggeling, C., and Fritzsche, M. (2017). Dissecting the actin cortex density and membrane-cortex distance in living cells by super-resolution microscopy. *Journal of Physics D: Applied Physics*, 50(6):064002.

[Coelho et al., 2009] Coelho, L. P., Shariff, A., and Murphy, R. F. (2009). Nuclear segmentation in microscope cell images: A hand-segmented dataset and comparison of algorithms. In *Proceedings of the 6th IEEE International Symposium on Biomedical Imaging: From Nano to Macro, ISBI*, pages 518–521.

[Cohen et al., 1992] Cohen, I., Cohen, L. D., and Ayache, N. (1992). Using deformable surfaces to segment 3-D images and infer differential structures. In *ECCV*, pages 648–652.

[Cohen et al., 1995] Cohen, J. D., Lin, M. C., Manocha, D., and Ponamgi, M. (1995). I-collide: An interactive and exact collision detection system for large-scale environments. In *I3D 95, Proceedings of the 1995 Symposium on Interactive 3D Graphics*, pages 189–196, New York, USA. ACM.

[Cohen, 1991] Cohen, L. D. (1991). On active contour models and balloons. *Computer Vision, Graphics and Image Processing: Image Understanding*, 53(2):211–218.

[Concha et al., 2012] Concha, M. L., Bianco, I. H., and Wilson, S. W. (2012). Encoding asymmetry within neural circuits. *Nature Reviews Neuroscience*, 13:832–843.

[Concha et al., 2003] Concha, M. L., Russell, C., Regan, J. C., Tawk, M., Sidi, S., Gilmour, D. T., Kapsimali, M., Sumoy, L., Goldstone, K., Amaya, E., Kimelman, D., Nicolson, T., Gründer, S., Gomperts, M., Clarke, J. D., and Wilson, S. W. (2003). Local tissue interactions across the dorsal midline of the forebrain establish CNS laterality. *Neuron*, 39:423–438.

[Cootes et al., 1995] Cootes, T. F., Taylor, C. J., Cooper, D. H., and Graham, J. (1995). Active shape models - their training and application. *Computer Vision and Image Understanding*, 61(1):38–59.

[de Berg et al., 2008] de Berg, M., Cheong, O., van Kreveld, M., and Overmars, M. (2008). *Computational Geometry: Algorithms and Applications*. Springer-Verlag, Berlin - Heidelberg, 3rd edition.

[de Chaumont et al., 2012] de Chaumont, F., Dallongeville, S., Chenouard, N., Hervé, N., Pop, S., Provoost, T., Meas-Yedid, V., Pankajakshan, P., Lecomte, T., Montagner, Y. L., Lagache, T., Dufour, A., and Olivo-Marin, J.-C. (2012). Icy: an open bioimage informatics platform for extended reproducible research. *Nature Methods*, 9:690–696.

[de Tullio et al., 2007] de Tullio, L., Maggio, B., Härtel, S., Jara, J., and Fanani, M. L. (2007). The initial surface composition and topography modulate sphingomyelinase-driven sphingomyelin to ceramide conversion in lipid monolayers. *Cell Biochemistry and Biophysics*, 47(2):169–177.

[Delpiano, 2013] Delpiano, J. (2013). *Analysis and evaluation of optical flow methods with applications in biology*. PhD thesis, Department of Electrical Engineering, University of Chile, Chile.

[Delpiano et al., 2012] Delpiano, J., Jara, J., Scheer, J., Ramírez, O., del Solar, J. R., and Härtel, S. (2012). Performance of optical flow techniques for motion analysis of fluorescent point signals in confocal microscopy. *Machine Vision and Applications*, 23:675–689. doi 10.1007/s00138-011-0362-8.

[Dice, 1945] Dice, L. R. (1945). Measures of the amount of ecologic association between species. *Ecology*, 26:297–302.

[Dima et al., 2011] Dima, A. A., Elliott, J. T., Filliben, J. J., Halter, M., Peskin, A., Bernal, J., Kociolek, M., Brady, M. C., Tang, H. C., and Plant, A. L. (2011). Comparison of segmentation algorithms for fluorescence microscopy images of cells. *Cytometry A*, 79(7):545–559.

[Dufour et al., 2005] Dufour, A., Shinin, V., Tajbakhsh, S., Guillén-Aghion, N., Olivo-Marin, J.-C., and Zimmer, C. (2005). Segmenting and tracking fluorescent cells in dynamic 3-D microscopy with coupled active surfaces. *IEEE Transactions on Image Processing*, 14(9):1396–1410.

[Dufour et al., 2011] Dufour, A., Thibeaux, R., Labruyere, E., Guillen, N., and Olivo-Marin, J. (2011). 3-D active meshes: Fast discrete deformable models for cell tracking in 3-D time-lapse microscopy. *IEEE Transactions on Image Processing*, 20(7):1925–1937.

[Dufour et al., 2017] Dufour, A. C., Jonker, A. H., and Olivo-Marin, J.-C. (2017). Deciphering tissue morphodynamics using bioimage informatics. *Philosophical Transactions of the Royal Society of London B: Biological Sciences*, 372(1720).

[Dunn, 1964] Dunn, O. J. (1964). Multiple comparisons using rank sums. *Technometrics*, 6(3):241–252.

[Dzyubachyk et al., 2007] Dzyubachyk, O., Niessen, W., and Meijering, E. (2007). A variational model for level-set based cell tracking in time-lapse fluorescence microscopy images. In *Proceedings of the 4th IEEE International Symposium on Biomedical Imaging ISBI: From Nano to Macro*, pages 97–100.

[Dzyubachyk et al., 2010] Dzyubachyk, O., van Cappellen, W. A., Essers, J., Niessen, W. J., and Meijering, E. (2010). Advanced level-set-based cell tracking in time-lapse fluorescence microscopy. *IEEE Transactions on Medical Imaging*, 29(3):852–867.

[Fanani et al., 2009] Fanani, M. L., de Tullio, L., Härtel, S., Jara, J., and Maggio, B. (2009). Sphingomyelinase-induced domain shape relaxation driven by out-of-equilibrium changes

of composition. *Biophysical Journal*, 96(1):67–76.

[Fanani et al., 2010] Fanani, M. L., Härtel, S., Maggio, B., DeTullio, L., Jara, J., Olmos, F., and Oliveira, R. G. (2010). The action of sphingomyelinase in lipid monolayers as revealed by microscopic image analysis. *Biochimica et Biophysica Acta - Biomembranes*, 1798(7):1309–1323.

[Farrell et al., 2017] Farrell, D. L., Weitz, O., Magnasco, M. O., and Zallen, J. A. (2017). SEGGA: a toolset for rapid automated analysis of epithelial cell polarity and dynamics. *Development*, 144(9):1725–1734.

[Fidorra et al., 2009] Fidorra, M., García, A., Ipsen, J. H., Härtel, S., and Bagatolli, L. A. (2009). Lipid domains in giant unilamellar vesicles and their correspondence with equilibrium thermodynamic phases: A quantitative fluorescence microscopy imaging approach. *Biochimica et Biophysica Acta (BBA) - Biomembranes*, 1788(10):2142–2149.

[Fink et al., 1998] Fink, C., Morgan, F., and Loew, L. M. (1998). Intracellular fluorescent probe concentrations by confocal microscopy. *Biophysical Journal*, 75(4):1648–1658.

[Finkel and Bentley, 1974] Finkel, R. and Bentley, J. (1974). Quad trees: A data structure for retrieval on composite keys. *Acta Informatica*, 4(1):1–9.

[Frangi et al., 1998] Frangi, A. F., Niessen, W. J., Vincken, K. L., and Viergever, M. A. (1998). Multiscale vessel enhancement filtering. In Wells, W. M., Colchester, A., and Delp, S., editors, *Medical Image Computing and Computer-Assisted Intervention - MICCAI '98*, volume 1496 of *Lecture Notes in Computer Science*, pages 130–137. Springer, Berlin - Heidelberg.

[Friedl and Gilmour, 2009] Friedl, P. and Gilmour, D. (2009). Collective cell migration in morphogenesis, regeneration and cancer. *Nature Reviews Molecular Cell Biology*, 10:445–457.

[Friedman, 1937] Friedman, M. (1937). The use of ranks to avoid the assumption of normality implicit in the analysis of variance. *Journal of the American Statistical Association*, 32(200):675–701.

[Gonzalez and Woods, 2007] Gonzalez, R. C. and Woods, R. E. (2007). *Digital Image Processing*. Prentice Hall, 3rd edition.

[Hagan and Zhao, 2009] Hagan, A. and Zhao, Y. (2009). Parallel 3D image segmentation of large data sets on a GPU cluster. In *Proceedings of the 5th International Symposium on Advances in Visual Computing: Part II*, pages 960–969, Berlin - Heidelberg. Springer-Verlag.

[Hall et al., 2009] Hall, M., Frank, E., Holmes, G., Pfahringer, B., Reutemann, P., and Witten, I. H. (2009). The WEKA data mining software: An update. *SIGKDD Explorations*, 11(1):10–18.

[Härtel et al., 2007] Härtel, S., Jara, J., Lemus, C. G., and Concha, M. L. (2007). 3D morpho-

topological analysis of asymmetric neuronal morphogenesis in developing zebrafish. In Tavares, J. M. and Nata, J., editors, *Computational Modeling of Objects Represented in Images. Fundamentals, Methods and Applications*, pages 215–220. Taylor and Francis Group.

[Hell et al., 2004] Hell, S., Dyba, M., and Jakobs, S. (2004). Concepts for nanoscale resolution in fluorescence microscopy. *Current Opinion in Neurobiology*, 14(5):599–609.

[Horn and Schunk, 1981] Horn, B. K. and Schunk, B. G. (1981). Determining optical flow. *Artificial Intelligence*, 17:185–204.

[Hough, 1959] Hough, P. (1959). Machine analysis of bubble chamber pictures. In *Proceedings of the International Conference on High Energy Accelerators and Instrumentation*, volume 73.

[Houston et al., 2006] Houston, B., Nielsen, M. B., Batty, C., Nilsson, O., and Museth, K. (2006). Hierarchical RLE level set: A compact and versatile deformable surface representation. *ACM Transactions on Graphics*, 25(1):151–175.

[Ishihara and Sugimura, 2012] Ishihara, S. and Sugimura, K. (2012). Bayesian inference of force dynamics during morphogenesis. *Journal of Theoretical Biology*, 313:201–211.

[Jaouen et al., 2014] Jaouen, V., Gonzalez, P., Stute, S., Guilloteau, D., Chalon, S., Buvat, I., and Tauber, C. (2014). Variational segmentation of vector-valued images with gradient vector flow. *IEEE Transactions on Image Processing*, 23(11):4773–4785.

[Jara-Wilde et al., 2020] Jara-Wilde, J., Castro, I., Lemus, C. G., Palma, K., Valdés, F., Castañeda, V., Hitschfeld-Kahler, N., Concha, M. L., and Härtel, S. (2020). Optimising adjacent membrane segmentation and parameterisation in multi-cellular aggregates by piecewise active contours. *Journal of Microscopy*, 278(2):59–75.

[Jara-Wilde et al., 2015] Jara-Wilde, J., Cerda, M., Delpiano, J., and Härtel, S. (2015). An implementation of combined local-global optical flow. *Image Processing On Line (IPOL)*, 5:139–158.

[Kapur et al., 1985] Kapur, J., Sahoo, P., and Wong, A. (1985). A new method for gray-level picture thresholding using the entropy of the histogram. *Computer Vision, Graphics and Image Processing*, 29(3):273–285.

[Kass et al., 1988] Kass, M., Witkin, A., and Terzopoulos, D. (1988). Snakes: Active contour models. *International Journal of Computer Vision*, 1(4):321–331.

[Keller, 2013] Keller, P. J. (2013). In vivo imaging of zebrafish embryogenesis. *Methods*, 62:268–278.

[Keller et al., 2008] Keller, P. J., Schmidt, A. D., Wittbrodt, J., and Stelzer, E. H. K. (2008). Reconstruction of zebrafish early embryonic development by scanned light sheet microscopy. *Science*, 322(5904):1065–1069.

[Keller and Stelzer, 2008] Keller, P. J. and Stelzer, E. H. K. (2008). Quantitative in vivo

imaging of entire embryos with digital scanned laser light sheet fluorescence microscopy. *Current Opinion in Neurobiology*, 18(6):624–632.

[Kockara et al., 2007] Kockara, S., Halic, T., Iqbal, K., Bayrak, C., and Rowe, R. (2007). Collision detection: A survey. In *IEEE International Conference on Systems, Man and Cybernetics (ISIC)*, pages 4046–4051.

[Kubitschek, 2017] Kubitschek, U., editor (2017). *Fluorescence Microscopy: From Principles to Biological Applications*. Wiley-VCH, Weinheim, Germany, 2nd edition.

[Lakowicz, 2006] Lakowicz, J. R. (2006). *Principles of Fluorescence Spectroscopy*. Principles of Fluorescence Spectroscopy. Springer, New York, 3rd edition.

[Lam et al., 1992] Lam, L., Lee, S.-W., and Suen, C. Y. (1992). Thinning methodologies-a comprehensive survey. *IEEE Transactions on Pattern Analysis and Machine Intelligence*, 14(9):869–885.

[Lecaudey et al., 2008] Lecaudey, V., Cakan-Akdogan, G., Norton, W. H. J., and Gilmour, D. (2008). Dynamic Fgf signaling couples morphogenesis and migration in the zebrafish lateral line primordium. *Development*, 135(16):2695–2705.

[LeCun et al., 2015] LeCun, Y., Bengio, Y., and Hinton, G. (2015). Deep learning. *Nature*, 521:436–444.

[Lemus et al., 2021] Lemus, C. G., Jara-Wilde, J., Palma, K., Reig, G., Marcellini, S., Härtel, S., and Concha, M. L. (2021). Nodal signalling controls brain asymmetry by directing asymmetric cellular mophogenesis in zebrafish embryo. In preparation.

[Lemus et al., 2017] Lemus, C. G., Palma, K., Jara, J., Cramer, T., Härtel, S., and Concha, M. L. (2017). Asymmetric morphogenesis of the parapineal organ in the embryonic zebrafish brain. *Mechanisms of Development*, 145:S56.

[Li et al., 2005] Li, C., Liu, J., and Fox, M. D. (2005). Segmentation of edge preserving gradient vector flow: An approach toward automatically initializing and splitting of snakes. In *Proceedings of 2005 IEEE Conference on Computer Vision and Pattern Recognition, (CVPR '05)*, pages 162–167, Los Alamitos, California. IEEE Computer Society Press.

[Liddle et al., 2020] Liddle, P., Jara-Wilde, J., Lafon-Hughe, L., Castro, I., Härtel, S., and Folle, G. (2020). dSTORM microscopy evidences in hela cells clustered and scattered γH2AX nanofoci sensitive to ATM, DNA-PK, and ATR kinase inhibitors. *Molecular and Cellular Biochemistry*, 473(1):77–91.

[Liddle et al., 2014] Liddle, P., Lafon-Hughes, L., Tomaso, M. V. D., Reyes-Ábalos, A. L., Jara, J., Cerda, M., Härtel, S., and Folle, G. A. (2014). Bleomycin-induced γH2AX foci map preferentially to replicating domains in CHO9 interphase nuclei. *Chromosome Research*, 22:463–481.

[Lin and Gottschalk, 1998] Lin, M. C. and Gottschalk, S. (1998). Collsion detection between geometric models: A survey. In *Proceedings of IMA Conference on Mathematics of*

Surfaces, volume 1, pages 602–608.

[Losasso et al., 2004] Losasso, F., Gibou, F., and Fedkiw, R. (2004). Simulating water and smoke with an octree data structure. *ACM Transactions on Graphics*, 23(3):457–462.

[Lucas et al., 2012] Lucas, B. C., Kazhdan, M., and Taylor, R. H. (2012). Multi-object geodesic active contours (MOGAC). In Ayache, N., Delingette, H., Golland, P., and Mori, K., editors, *Medical Image Computing and Computer-Assisted Intervention - MICCAI 2012*, volume 7511 of *Lecture Notes in Computer Science*, pages 404–412. Springer-Verlag, Berlin - Heidelberg.

[Ludwig et al., 2009] Ludwig, O., Delgado, D., Goncalves, V., and Nunez, U. (2009). Trainable classifier-fusion schemes: An application to pedestrian detection. In *Proceedings of the 12th IEEE Conference on Intelligent Transportation Systems*, volume 1, pages 432–437.

[Marr, 1982] Marr, D. (1982). *Vision*. Freeman, San Francisco.

[Marr and Hildreth, 1980] Marr, D. and Hildreth, E. (1980). Theory of edge detection. In *Proceedings of the Royal Society of London B: Biological Sciences*, volume 207, pages 187–217, London. The Royal Society.

[Mashburn et al., 2012] Mashburn, D. N., Lynch, H. E., Ma, X., and Hutson, M. S. (2012). Enabling user-guided segmentation and tracking of surface labeled cells in time-lapse image sets of living tissues. *Cytometry A*, 85:409–418.

[Massey Jr., 1951] Massey Jr., F. J. (1951). The Kolmogorov-Smirnov test for goodness of fit. *Journal of the American Statistical Association*, 46(253):68–78.

[McCormick et al., 2014] McCormick, M., Liu, X., Jomier, J., Marion, C., and Ibanez, L. (2014). ITK: enabling reproducible research and open science. *Frontiers in Neuroinformatics*, 8:13.

[McInerney and Terzopoulos, 1995a] McInerney, T. and Terzopoulos, D. (1995a). A dynamic finite element surface model for segmentation and tracking in multidimensional medical images with application to cardiac 4D image analysis. *Computerized Medical Imaging and Graphics*, 19(1):69–83.

[McInerney and Terzopoulos, 1995b] McInerney, T. and Terzopoulos, D. (1995b). Topologically adaptable snakes. In *Proceedings of the Fifth International Conference on Computer Vision (ICCV'95)*, pages 840–845.

[McInerney and Terzopoulos, 1996] McInerney, T. and Terzopoulos, D. (1996). Deformable models in medical image analysis: a survey. *Medical Image Analysis*, 1(2):91–108.

[McInerney and Terzopoulos, 1999] McInerney, T. and Terzopoulos, D. (1999). Topology adaptive deformable surfaces for medical image volumen segmentation. *IEEE Transactions on Medical Imaging*, 18(10):840–850.

[Meijering, 2012] Meijering, E. (2012). Cell segmentation: 50 years down the road [life sci-

ences]. *IEEE Signal Processing Magazine*, 29(5):140–145.

[Meijering et al., 2012] Meijering, E., Dzyubachyk, O., and Smal, I. (2012). Methods for cell and particle tracking. *Methods in Enzymology*, 504:183–200.

[Meijering et al., 2009] Meijering, E., Dzyubachyk, O., Smal, I., and van Cappellen, W. A. (2009). Tracking in cell and developmental biology. In *Seminars in Cell and Developmental Biology*, volume 20, pages 894–902.

[Melani et al., 2007] Melani, C., Peyriéras, N., Mikula, K., Zanella, C., Campana, M., Rizzi, B., Veronesi, F., Sarti, A., Lombardot, B., and Bourgine, P. (2007). Cells tracking in a live zebrafish embryo. In *Proceedings of the 29th Annual International Conference of the IEEE/Engineering in Medicine and Biology Society EMBS, 2007*, pages 1631–1634.

[Michelin et al., 2014] Michelin, G., Guignard, L., Fiuza, U.-M., and Mandalain, G. (2014). Embryo cell membranes reconstruction by tensor voting. In *Proceedings of the IEEE 11th International Symposium on Biomedical Imaging (ISBI)*, pages 1259–1262.

[Mikula et al., 2011] Mikula, K., Peyriéras, N., Remešíková, M., and Smíšek, M. (2011). 4D numerical schemes for cell image segmentation and tracking. In Fořt, J., Fürst, J., Halama, J., Herbin, R., and Hubert, F., editors, *Finite Volumes for Complex Applications VI Problems & Perspectives*, volume 4 of *Springer Proceedings in Mathematics*, pages 693–701. Springer-Verlag, Berlin - Heidelberg.

[Mikula et al., 2012] Mikula, K., Smíšek, M., and Špir, R. (2012). Parallel algorithms for segmentation of cellular structures in 2D+time and 3D morphogenesis data. In *Proceedings of ALGORITMY 2012*, pages 416–426.

[Mikut et al., 2013] Mikut, R., Dickmeis, T., Driever, W., Geurts, P., Hamprecht, F. A., Kausler, B. X., Ledesma-Carbayo, M. J., Marée, R., Mikula, K., Pantazis, P., Ronneberger, O., Santos, A., Stotzka, R., Strähle, U., , and Peyriéras, N. (2013). Automated processing of zebrafish imaging data: A survey. *Zebrafish*, 10:401–421.

[Mischler et al., 2006] Mischler, D., Romaniuk, B., Benassarou, A., and Bittar, E. (2006). Robust 4D segmentation of cells in confocal images. In *Proceedings of the International Conference on Computer Vision and Graphics*, pages 1–6.

[Mohan et al., 2014] Mohan, K., Purnapatra, S. B., and Mondal, P. P. (2014). Three dimensional fluorescence imaging using multiple light-sheet microscopy. *PLoS One*, 9(6):e96551.

[Mónaco et al., 2021] Mónaco, A., Canales-Huerta, N., Jara-Wilde, J., Härtel, S., Chabalgoity, A., Moreno, M., and Scavone, P. (2021). Salmonella typhimurium triggers extracellular traps release in murine macrophages. *Frontiers in Cellular and Infection Microbiology*, In revision.

[Montagnat and Delingette, 2005] Montagnat, J. and Delingette, H. (2005). 4D deformable models with temporal constraints: application to 4D cardiac image segmentation. *Medical Image Analysis*, 9(1):87–100.

[Montero and Heisenberg, 2004] Montero, J.-A. and Heisenberg, C.-P. (2004). Gastrulation dynamics: cells move into focus. *Trends in Cell Biology*, 14(11):620–627.

[Moraga, 2019] Moraga, H. (2019). Clasificación y comparación de métodos de detección de colisiones de fase amplia para imágenes sintéticas en 2D+tiempo. MSc thesis, University of Chile, Computer Science Department.

[Mosaliganti et al., 2012] Mosaliganti, K. R., Noche, R. R., Xiong, F., Swinburne, I. A., and Megason, S. G. (2012). ACME: Automated cell morphology extractor for comprehensive reconstruction of cell membranes. *PLoS Computational Biology*, 8(12):e1002780.

[Namías et al., 2016] Namías, R., D'Amato, J. P., del Fresno, M., Vénere, M., Pirró, N., and Bellemare, M.-E. (2016). Multi-object segmentation framework using deformable models for medical imaging analysis. *Medical & Biological Engineering & Computing*, 54(8):1181–1192.

[Nath et al., 2006] Nath, S., Bunyak, F., and Palaniappan, K. (2006). Robust tracking of migrating cells using four-color level set segmentation. In *8th international conference on Advanced Concepts For Intelligent Vision Systems (ACIVS)*, pages 920–932.

[Nielsen and Museth, 2006] Nielsen, M. B. and Museth, K. (2006). Dynamic tubular grid: An efficient data structure and algorithms for high resolution level sets. *Journal of Scientific Computing*, 26(3):261–299.

[Nixon and Aguado, 2008] Nixon, M. and Aguado, A. S. (2008). *Feature Extraction & Image Processing*. Academic Press, London, 2nd edition.

[Obara et al., 2012] Obara, B., Fricker, M., and Grau, V. (2012). Coherence enhancing diffusion filtering based on the phase congruency tensor. In *Biomedical Imaging (ISBI), 2012 9th IEEE International Symposium on*, pages 202–205.

[Olmos, 2009] Olmos, L. F. (2009). Segmentación de objetos en imágenes de microscopia mediante contornos activos con adaptabilidad topológica. Memoria para optar al título de Ingeniero Civil en Computación e Ingeniero Civil Matemático, Universidad de Chile.

[Osher and Paragios, 2003] Osher, S. and Paragios, N., editors (2003). *Geometric Level Set Methods in Imaging, Vision, and Graphics*. Springer-Verlag, New York, 3rd edition.

[Osher and Sethian, 1988] Osher, S. and Sethian, J. A. (1988). Fronts propagating with curvature-dependent speed: Algorithms based on Hamilton-Jacobi formulations. *Journal of Computational Physics*, 79(1):12–49.

[Otsu, 1979] Otsu, N. (1979). A threshold selection method from gray-level histograms. *IEEE Transactions on Systems, Man and Cybernetics*, 9(1):62–66.

[Pantazis and Supatto, 2014] Pantazis, P. and Supatto, W. (2014). Advances in whole-embryo imaging: a quantitative transition is underway. *Nature Reviews Molecular Cell Biology*, 15:327–339.

[Papari and Petkov, 2011] Papari, G. and Petkov, N. (2011). Edge and line oriented contour detection: State of the art. *Image and Vision Computing*, 29:79–103.

[Pawley, 2006] Pawley, J., editor (2006). *Handbook of Biological Confocal Microscopy (Chapter 43: Confocal and Multi-photon Imaging of Living Embryos).* Springer-Verlag, New York, US.

[Pham et al., 2000] Pham, D. L., Xu, C., and Prince, J. (2000). Current methods in medical image segmentation. *Annual Review of Biomedical Engineering*, 2:315–337.

[Planchon et al., 2011] Planchon, T. A., Gao, L., Milkie, D. E., Davidson, M. W., Galbraith, J. A., Galbraith, C. G., and Betzig, E. (2011). Rapid three-dimensional isotropic imaging of living cells using Bessel beam plane illumination. *Nature Methods*, 8(5):417–426.

[Pop et al., 2013] Pop, S., Dufour, A., Garrec, J.-F. L., Ragni, C. V., Cimper, C., Meilhac, S. M., and Olivo-Marin, J.-C. (2013). Extracting 3D cell parameters from dense tissue environments: application to the development of the mouse heart. *Bioinformatics*, 29:772–779.

[Prewitt, 1970] Prewitt, J. M. (1970). Object enhancement and extraction. *Picture processing and Psychopictorics*, 10(1):15–19.

[Rabut and Ellenberg, 2004] Rabut, G. and Ellenberg, J. (2004). Automatic real-time three-dimensional cell tracking by fluorescence microscopy. *Journal of Microscopy*, 216(2):131–137.

[Ramírez et al., 2010] Ramírez, O., García, A., Rojas, R., Couve, A., and Härtel, S. (2010). Confined displacement algorithm determines true and random colocalization in fluorescence microscopy. *Journal of Microscopy*, 239(3):173–183.

[Regan et al., 2009] Regan, J. C., Concha, M. L., Roussigne, M., Russell, C., and Wilson, S. W. (2009). An Fgf8-dependent bistable cell migratory event establishes CNS asymmetry. *Neuron*, 61:27–34.

[Reig et al., 2017] Reig, G., Cerda, M., Sepúlveda, N., Flores, D., Castañeda, V., Tada, M., Härtel, S., and Concha, M. L. (2017). Extra-embryonic tissue spreading directs early embryo morphogenesis in killifish. *Nature Communications*, 8:1–14.

[Richardson et al., 2016] Richardson, J., Gauert, A., Briones-Montecinos, L., Fanlo, L., Alhashem, Z.-M., Assar, R., Marti, E., Kabla, A., Härtel, S., and Linker, C. (2016). Leader cells define directionality of trunk, but not cranial, neural crest cell migration. *Cell Reports*.

[Ritter et al., 2010] Ritter, J., Spille, J.-H., Kaminski, T., and Kubitscheck, U. (2010). A cylindrical zoom lens unit for adjustable optical sectioning in light sheet microscopy. *Biomedical Optics Express*, 2:185–193.

[Rørth, 2009] Rørth, P. (2009). Collective cell migration. *Annual Review of Cell and Developmental Biology*, 25:407–429.

[Roycroft and Mayor, 2018] Roycroft, A. and Mayor, R. (2018). Michael Abercrombie: contact inhibition of locomotion and more. *The International journal of developmental biology*, 62:5–13.

[Sacan et al., 2008] Sacan, A., Ferhatosmanoglu, H., and Coskun, H. (2008). CellTrack: an open-source software for cell tracking and motility analysis. *Bioinformatics*, 24(14):1647–1649.

[Sanchez-Corrales et al., 2018] Sanchez-Corrales, Y. E., Blanchard, G. B., and Röper, K. (2018). Radially patterned cell behaviours during tube budding from an epithelium. *eLife*, 7:e35717.

[Santi, 2011] Santi, P. A. (2011). Light sheet fluorescence microscopy: a review. *Journal of Histochemistry and Cytochemistry*, 59(2):129–38.

[Sapiro, 1997] Sapiro, G. (1997). Color snakes. *Computer Vision and Image Understanding*, 68(2):247–253.

[Sapiro, 2001] Sapiro, G. (2001). *Geometric Partial Differential Equations and Image Analysis*. Cambridge University Press, Cambridge, UK.

[Sarti et al., 2000] Sarti, A., Malladi, R., and Sethian, J. A. (2000). Subjective surfaces: A method for completing missing boundaries. *Proceedings of the National Academy of Sciences of the United States of America*, 97(12):6258–6263.

[Sarti et al., 2002] Sarti, A., Malladi, R., and Sethian, J. A. (2002). Subjective surfaces: A geometric model for boundary completion. *International Journal of Computer Vision*, 46(3):201–221.

[Schermelleh et al., 2010] Schermelleh, L., Heintzmann, R., and Leonhardt, H. (2010). A guide to super-resolution fluorescence microscopy. *The Journal of Cell Biology*, 190(2):165–175.

[Schindelin et al., 2012] Schindelin, J., Arganda-Carreras, I., Frise, E., Kaynig, V., Longair, M., Pietzsch, T., Preibisch, S., Rueden, C., Saalfeld, S., Schmid, B., Tinevez, J., White, D., Hartenstein, V., Eliceiri, K., Tomancak, P., and Cardona, A. (2012). FIJI: an open-source platform for biological-image analysis. *Nature Methods*, 9(7):676–682.

[Schmidhuber, 2012] Schmidhuber, J. (2012). Deep learning in neural networks: An overview. *Neural Networks*, 61:485–117.

[Sethian, 2010] Sethian, J. A. (1996-2010). Moving interfaces and boundaries: Level set methods and fast marching methods. [online] http://math.berkeley.edu/~sethian/. [Access: March 03, 2019].

[Shapiro and Stockman, 2001] Shapiro, L. G. and Stockman, G. C. (2001). *Computer Vision*. Prentice-Hall, New Jersey.

[Shapiro and Wilk, 1965] Shapiro, S. S. and Wilk, M. B. (1965). An analysis of variance test

for normality (complete samples). *Biometrika*, 52(3–4):591–611.

[Sherrard et al., 2010] Sherrard, K., Robin, F., Lemaire, P., and Munro, E. (2010). Sequential activation of apical and basolateral contractility drives ascidian endoderm invagination. *Current Biology*, 20(17):1–12.

[Signore and Concha, 2014] Signore, I. A. and Concha, M. L. (2014). Genetics: a common origin for neuronal asymmetries? *Current Biology*, 5:R201–R204.

[Skylaki et al., 2016] Skylaki, S., Hilsenbeck, O., and Schroeder, T. (2016). Challenges in long-term imaging and quantification of single-cell dynamics. *Nature Biotechnology*, 34:1137–1144.

[Sobel, 1970] Sobel, I. E. (1970). *Camera models and machine perception*. PhD thesis, Dept. of Computer Science, Stanford, California. AAI7102831.

[Sommer et al., 2011] Sommer, C., Strähle, C., Köthe, U., and Hamprecht, F. A. (2011). ilastik: Interactive learning and segmentation toolkit. In *Proceedings of the Eighth IEEE International Symposium on Biomedical Imaging (ISBI)*, pages 230–233.

[Sørensen, 1948] Sørensen, T. (1948). A method of establishing groups of equal amplitude in plant sociology based on similarity of species and its application to analyses of the vegetation on Danish commons. *Kongelige Danske Videnskabernes Selskab*, 5:1–34.

[Spontón and Cardelino, 2015] Spontón, H. and Cardelino, J. (2015). A review of classic edge detectors. *Image Processing On Line*, pages 90–123.

[Stegmaier et al., 2016] Stegmaier, J., Amat, F., Lemon, W. C., McDole, K., Wan, Y., Teodoro, G., Mikut, R., and Keller, P. J. (2016). Real-time three-dimensional cell segmentation in large-scale microscopy data of developing embryos. *Developmental Cell*, 36(2):225–240.

[Swoger et al., 2014] Swoger, J., Pampaloni, F., and Stelzer, E. H. (2014). Light-sheet-based fluorescence microscopy for three-dimensional imaging of biological samples. *Cold Spring Harbor Protocols*, 2014(1):1–18.

[Teschner et al., 2005] Teschner, M., Kimmerle, S., Heidelberger, B., Zachmann, G., Raghupathi, L., Fuhrmann, A., Cani, M.-P., Faure, F., Magnemat-Thalmann, N., Strasser, W., and Volino, P. (2005). Collision detection for deformable models. *Computer Graphics Forum*, 24(1):61–81.

[Tukey, 1949] Tukey, J. (1949). Comparing individual means in the analysis of variance. *Biometrics*, 5(2):99–114.

[Unal et al., 2005] Unal, G., Yezzi, A., and Krim, H. (2005). Information-theoretic active polygons for unsupervised texture segmentation. *International Journal of Computer Vision*, 62(3):199–220.

[Vachier and Meyer, 2005] Vachier, C. and Meyer, F. (2005). The viscous watershed trans-

form. *Journal of Mathematical Imaging and Vision*, 22(2-3):251–267.

[Veldhuis et al., 2017] Veldhuis, J. H., Ehsandar, A., Maître, J.-L., Hiiragi, T., Cox, S., and Brodland, G. W. (2017). Inferring cellular forces from image stacks. *Philosophical Transactions of the Royal Society B: Biological Sciences*, 372(1720):20160261.

[Verveer et al., 2007] Verveer, P. J., Swoger, J., Pampaloni, F., Greger, K., Marcello, M., and Stelzer, E. H. K. (2007). High-resolution three-dimensional imaging of large specimens with light sheet-based microscopy. *Nature Methods*, 4(4):311–313.

[von Gioi et al., 2012] von Gioi, R. G., Jakubowicz, J., Morel, J.-M., and Randall, G. (2012). LSD: a line segment detector. *Image Processing On Line*, 2:35–55.

[Vonesch et al., 2006] Vonesch, C., Aguet, F., Vonesch, J.-L., and Unser, M. (2006). The colored revolution of bioimaging. *IEEE Signal Processing Magazine*, 23(3):20–31.

[Wang et al., 2012] Wang, G., Manning, M. L., and Amack, J. D. (2012). Regional cell shape changes control form and function of Kupffer's vesicle in the zebrafish embryo. *Developmental Biology*, 370:52–62.

[Wang et al., 2007] Wang, X., He, W., Metaxas, D., Mathew, R., and White, E. (2007). Cell segmentation and tracking using texture-adaptive snakes. In *Proceedings of the 4th IEEE International Symposium on Biomedical Imaging ISBI: From Nano to Macro*, pages 101–104.

[Waters and Wittman, 2014] Waters, J. C. and Wittman, T., editors (2014). *Quantitative Imaging in Cell Biology*, volume 123 of *Methods in Cell Biology*. Elsevier, Amsterdam, NL.

[Weiler and Atherton, 1977] Weiler, K. and Atherton, P. (1977). Hidden surface removal using polygon area sorting. *Computer Graphics*, 11(2):214–222.

[Whitaker, 1998] Whitaker, R. T. (1998). A level-set approach to 3D reconstruction from range data. *International Journal of Computer Vision*, 29(3):203–231.

[Williams and Shah, 1992] Williams, D. J. and Shah, M. (1992). A fast algorithm for active contours and curvature estimation. *CVGIP: Image Understanding*, 55(1):14–26.

[Xu et al., 2000] Xu, C., Jr., A. Y., and Prince, J. L. (2000). On the relationship between parametric and geometric active contours. In *Proceedings of 34th Asilomar Conference on Signals, Systems and Computers*, pages 483–489.

[Xu and Prince, 1997] Xu, C. and Prince, J. L. (1997). Gradient vector flow: A new external force for snakes. In *Proceedings of the 1997 IEEE Conference on Computer Vision and Pattern Recognition (CVPR '97)*, pages 66–71, Los Alamitos, CA. IEEE Computer Society Press.

[Xu and Prince, 1998] Xu, C. and Prince, J. L. (1998). Generalized gradient vector flow external forces for active contours. *Signal Processing*, 71(2):131–139.

[Yap et al., 2018] Yap, A. S., Duszyc, K., and Viasnoff, V. (2018). Mechanosensing and mechanotransduction at cell–cell junctions. *Cold Spring Harbor Perspectives in Biology*, 10(8).

[Yates, 1974] Yates, R. C. (1974). *Curves and Their Properties.* National Council of Teachers of Mathematics.

[Yeo et al., 2011] Yeo, S. Y., Xie, X., Sazonov, I., and Nithirasu, P. (2011). Geometrically induced force interaction for three-dimensional deformable models. *IEEE Transactions on Image Processing*, 20(5):1373–1387.

[Yoo et al., 2002] Yoo, T., Ackerman, M., Lorensen, W., Schroeder, W., Chalana, V., Aylward, S., Metaxas, D., and Whitaker, R. (2002). Engineering and algorithm design for an image processing API: A technical report on ITK – the insight toolkit. In Westwood, J., editor, *Proceedings of Medicine Meets Virtual Reality*, pages 586–592, Amsterdam. IOS Press.

[Zanella et al., 2010] Zanella, C., Campana, M., Rizzi, B., Melani, C., Sanguinetti, G., Bourgine, P., Mikula, K., Peyriéras, N., and Sarti, A. (2010). Cells segmentation from 3-D confocal images of early zebrafish embryogenesis. *IEEE Transactions on Image Processing*, 79(3):770–781.

[Zhao and Xie, 2013] Zhao, F. and Xie, X. (2013). An overview of interactive medical image segmentation. *Annals of the BMVA*, 2013(7):1–22.

[Zimmer et al., 2011] Zimmer, H., Bruhn, A., and Weickert, J. (2011). Optic flow in harmony. *International Journal of Computer Vision*, 93(3):268–288.

Appendices

A Statistical Analysis of Similarity Indices

This section presents the tests performed to find statistically significant differences in the morphological Similarity Indices (Dice, Jaccard, Hausdorff Distance HD, and Normalized Sum of Distances NSD) obtained with MOC, PAC, and ALPACA contours from Expert (E1, E2, E3) and Ground Truth (GT) segmentations of synthetic and PpO cells (see 4.1, 4.3). Measurements of the Similarity Indices for Expert/Ground Truth (E1/GT, E2/GT, E3/GT) and Expert/Expert (E1/E2, E1/E3, E2/E3) contours were tested with the procedures described below. All tests were performed with the GraphPad Prism 8.0.1 software (GraphPad Software; San Diego, California, USA).

A .1 Similarity Indices across Algorithm Steps in Synthetic Cells

The first set of tests aims to detect significant differences in the Similarity Indices from Experts/Ground Truth contour measurements, that could be attributed to the steps of the ALPACA approach.

In order to select the comparison test for the Similarity Indices, it was necessary to determine first if the measured data can be treated as normally distributed. To this end, the Kolmogorov–Smirnov test [Massey Jr., 1951] was applied for each set of measurements, with significance level $\alpha = 0.05$. The obtained p values (Table A1) indicate that:

- for GT/E2, measurements for MOC (Dice and Jaccard) and PAC (Dice, Jaccard and NSD) are **rejected** as normally distributed; and
- for GT/E3, measurements for MOC (Dice, Jaccard and NSD) and ALPACA (HD and NSD) are **rejected** as normally distributed.

Comparison of Algorithm Steps

The changes in the Similarity Indices between MOC, PAC, and ALPACA steps were tested for the measurements data of Expert/Ground Truth. Since some data sets could not be treated as normally distributed, the comparisons were performed with the non-parametric Friedman test [Friedman, 1937] (Table A2, rows 2-3), followed by a *post hoc* Dunn test [Dunn, 1964] (Table A2, rows 4-8). The Friedman test is used to detect differences in the Similarity Indices measured at each algorithm step across Expert/Ground Truth combinations. The obtained p values indicate that a difference was detected in all cases; however, a complementary test was needed to determine which pairs of data sets present a significant difference. To this end, the non-parametric *post hoc* Dunn test was applied for the Similarity Indices from pairs of algorithm steps for each Expert/Ground Truth measurement set. The results from Table A2 are summarized as follows:

- Overall, the test results show that **in every Expert/Ground Truth measurement set, significant differences were found for all Similarity Indices between MOC and ALPACA (first and last steps), suggesting that the Similarity Indices for the synthetic cell contours changed after the application of the ALPACA approach**.
- The Friedman found a significant difference in all of the Indices, *i.e.* at least one data set does not appear to have the same distribution.
- For the Dice coefficient, the *post hoc* Dunn test found:
  - in MOC/PAC, significant differences for E1/GT only; and
  - in MOC/ALPACA and PAC/ALPACA, significant differences for every Expert/GT.
- For the Jaccard index, the *post hoc* Dunn test found:
  - in MOC/PAC, significant differences for E1/GT only;
  - in PAC/ALPACA, significant differences for E2/GT and E3/GT; and
  - in MOC/ALPACA, significant differences for every Expert/GT.
- For the Hausdorff Distance, the *post hoc* Dunn test found:
  - in MOC/PAC, significant differences for every Expert/GT;

  - in PAC/ALPACA, significant differences for E2/GT only; and
  - in MOC/ALPACA, significant differences for every Expert/GT.
- For the Normalized Sum of Distances, the *post hoc* Dunn test found:
  - in MOC/PAC, significant differences for E2/GT and E3/GT;
  - in PAC/ALPACA, significant differences for every Expert/GT; and
  - in MOC/ALPACA, significant differences for every Expert/GT.

A .2 Similarity Indices for Expert/Expert in Synthetic Cells

Complementary to the previous comparison, tests for detecting significant differences in the measured indices among Expert/Expert contours were applied. A test for normality was applied to find significant differences between experts using the Similarity Indices. Table A3 shows the results of the Kolmogorov-Smirmov test, applied with significance level $\alpha = 0.5$. In summary:

- Measurements of Dice and Jaccard indices are **rejected** as normally distributed across all steps and experts, except PAC for E1/E3.
- Measurements of NSD in all steps for E1/E2 are **rejected** as normally distributed, together with the ALPACA step for E1/E3.
- Measurements of HD are **accepted** as normally distributed for all pairs of experts.

Comparison of Experts

In order to find significant differences between measurements, the Friedman test was applied for the data sets that were rejected as normally distributed, and the ANOVA test, for the accepted. Significance level $\alpha = 0.5$ was used. Results are shown in Table A4, and summarized as:

- **Significant differences were found for most of the Expert/Expert and Expert/Ground Truth measurements**.
- For E1/E2, **no** significant differences found in HD across all steps.
- For E1/E3, **no** significant differences found in Dice and Jaccard across all steps.
- For E1/E3, **no** significant differences found in HD in PAC/ALPACA.
- For E1/E3, **no** significant differences found in NSD in MOC/ALPACA.
- For E2/E3, **no** significant differences found in HD in MOC/PAC and MOC/ALPACA.
- For E2/E3, **no** significant differences found in NSD in MOC/PAC.

Table A1: Normality Test of Experts/Ground Truth Similarity Indices obtained for MOC/PAC/ALPACA steps in synthetic cells. Kolmogorov-Smirnov test p values are shown. Significance level $\alpha = 0.05$. Similarity Indices: Dice, Jaccard, NSD (Normalized Sum of Distances), HD (Hausdorff Distance).

	E1/GT			E2/GT			E3/GT		
	MOC	PAC	ALPACA	MOC	PAC	ALPACA	MOC	PAC	ALPACA
Dice	0.0327	0.0001	<0.0001	>0.1000	>0.1000	0.04	>0.1000	0.0032	<0.0001
Jaccard	0.0337	<0.0001	<0.0001	>0.1000	>0.1000	0.0378	>0.1000	0.0027	<0.0001
HD [px]	<0.0001	<0.0001	0.0029	<0.0001	0.0009	0.0298	<0.0001	0.0003	>0.1000
NSD	0.0314	<0.0001	0.0128	0.0449	0.0551	0.0128	>0.1000	0.0161	0.0844

Table A2: Friedman and *post hoc* Dunn tests applied to the Experts/Ground Truth Similarity Indices obtained for MOC/PAC/ALPACA steps in synthetic cells. p values are shown (significant values in grey cells). Significance level $\alpha = 0.5$.

	Dice			Jaccard			Hausdorff Distance [px]			Normalized Sum of Distances		
	Friedman Test			Friedman Test			Friedman Test			Friedman Test		
All	<0.0001			<0.0001			<0.0001			<0.0001		
	E1/GT	E2/GT	E3/GT	E1/GT	E2/GT	E3/GT	E1/GT	E2/GT	E3/GT	E1/GT	E2/GT	E3/GT
MOC/PAC	0.0421	0.7705	0.1763	<0.0001	0.7705	0.1763	<0.0001	<0.0001	<0.0001	0.0055	<0.0001	<0.0001
PAC/ALPACA	<0.0001	<0.0001	<0.0001	>0.9999	<0.0001	0.0010	>0.9999	0.0102	>0.1763	0.0138	0.0075	0.0005
MOC/ALPACA	<0.0001	<0.0001	<0.0001	<0.0001	<0.0001	<0.0001	<0.0001	<0.0001	<0.0001	<0.0001	<0.0001	0.0039

Table A3: Normality test of Expert/Expert Similarity Indices obtained for MOC/PAC/ALPACA steps in synthetic cells. Kolmogorov-Smirnov test p values are shown (significant values in grey cells). Significance level $\alpha = 0.05$. Similarity Indices: Dice, Jaccard, NSD (Normalized Sum of Distances), HD (Hausdorff Distance).

	MOC			PAC			ALPACA		
	E1/E2	E1/E3	E2/E3	E1/E2	E1/E3	E2/E3	E1/E2	E1/E3	E2/E3
Dice	0.2502	0.4891	0.2674	0.817	0.0003	0.5191	0.1349	0.1527	<0.1437
Jaccard	0.2496	0.5082	0.2997	0.8265	0.0003	0.5687	0.1268	0.1482	0.1497
HD [px]	0.0001	<0.0001	<0.0001	<0.0001	0.0003	0.0001	0.0355	0.0297	<0.0001
NSD	0.1796	0.0024	0.0023	0.499	0.0125	0.0739	0.5253	0.1525	<0.0001

Table A4: Friedman and ANOVA/Tukey tests applied to the Expert/Expert Similarity Indices for MOC/PAC/ALPACA steps in synthetic cells. p values are shown (significant values in grey cells). Significance level $\alpha = 0.5$.

	Dice			Jaccard			Hausdorff Distance [px]			Normalized Sum of Distances		
	ANOVA	Friedman	ANOVA	ANOVA	Friedman	Friedman	Friedman	Friedman	Friedman	ANOVA	Friedman	Friedman
	E1/E2	E1/E3	E2/E3	E1/E2	E1/E3	E2/E3	E1/E2	E1/E3	E2/E3	E1/E2	E1/E3	E2/E3
	<0.0001	0.9775	<0.0001	<0.0001	0.9775	<0.0001	0.0597	0.0011	0.0028	<0.0001	<0.0001	<0.0001
MOC/PAC	0.0014	>0.9999	<0.0001	0.0013	>0.9999	<0.0001	0.057	0.0009	0.4974	0.0189	0.0019	0.099
PAC/ALPACA	<0.0001	>0.9999	<0.0001	<0.0001	>0.9999	<0.0001	0.4068	0.7229	<0.0019	<0.0001	0.0002	<0.0001
MOC/ALPACA	<0.0001	>0.9999	<0.0001	<0.0001	>0.9999	<0.0001	>0.9999	0.0426	0.1285	<0.0001	>0.9999	<0.0001

A .3 Comparison of Experts and ALPACA Steps in PpO Cells

First, a test for normality was applied to the measured Similarity Indices. Since the number of PpO cells is lower than the number of synthetic cells, the Shapiro-Wilk test [Shapiro and Wilk, 1965] was applied. Table A5 presents the p values obtained with significance level $\alpha = 0.5$ for the index measurements between each pair of experts: E1/E2, E2/E3, E1/E3, given the absence of Ground Truth data. As the table shows, **only measurements for E1/E2 were rejected as normally distributed: the Dice coefficient in ALPACA, and the Jaccard index in all steps**. In accordance with the Shapiro-Wilk findings, the ANOVA and Tukey range tests [Tukey, 1949] were applied to the Jaccard index measurements between E1/E2, and the Friedman's test, to the remaining data sets. Results from Table A6 are summarized as:

- Overall, **in PAC/ALPACA almost all of the significant differences appear in intersection-based indices (Dice, Jaccard); while in MOC/ALPACA they appear almost exclusively for E1/E2 in all Similarity Indices**.
- In MOC/PAC, **no** significant differences were found for all expert pairs and Similarity Indices.
- In PAC/ALPACA for Dice and Jaccard, significant differences were found for all expert pairs.
- In PAC/ALPACA for HD and NSD, **no** significant differences were found for all expert pairs, except NSD for E3/E1.
- In MOC/ALPACA
  - significant differences were found for all Similarity Indices between E1/E2, and HD for E2/E3; and
  - **no** significant differences were found for the rest.

Table A5: Normality test of Expert/Expert Similarity Indices obtained from MOC/PAC/ALPACA steps between Experts in PpO cells. Shapiro-Wilk test p values are shown (significant values in grey cells). Significance level $\alpha = 0.05$. Similarity Indices: Dice, Jaccard, NSD (Normalized Sum of Distances), HD (Hausdorff Distance).

	Dice			Jaccard			Hausdorff Distance [nm]			Normalized Sum of Distances		
	E2/E3	E1/E2	E3/E1	E2/E3	E1/E2	E3/E1	E2/E3	E1/E2	E3/E1	E2/E3	E1/E2	E3/E1
MOC	<0.0001	0.0172	<0.0001	<0.0001	0.1302	<0.0001	<0.0001	<0.0001	<0.0001	<0.0001	<0.0001	<0.0001
PAC	<0.0001	0.0437	<0.0001	<0.0001	0.2364	<0.0001	<0.0001	<0.0001	<0.0001	<0.0001	<0.0001	<0.0001
ALPACA	<0.0001	0.6539	<0.0001	<0.0001	0.8568	<0.0001	<0.0001	<0.0001	<0.0046	<0.0001	<0.0001	<0.0001

Table A6: Friedman and ANOVA/Tukey tests applied to the Expert/Expert Similarity Indices obtained for MOC/PAC/ALPACA steps in PpO cells. p values are shown (significant values in grey cells). Significance level $\alpha = 0.5$.

	Dice			Jaccard			Hausdorff Distance [nm]			Normalized Sum of Distances		
	Friedman Test			Friedman Test	ANOVA	Friedman Test	Friedman Test			Friedman Test		
	E2/E3	E1/E2	E3/E1	E2/E3	E1/E2	E3/E1	E2/E3	E1/E2	E3/E1	E2/E3	E1/E2	E3/E1
	0.0321	0.0340	0.0022	0.0321	0.0093	0.0022	0.0130	0.0031	0.3535	0.0529	0.0014	0.0488
MOC/PAC	0.9519	0.9203	0.1723	0.9519	0.3055	0.1723	0.1723	0.2674	0.9519	0.4008	0.4008	0.6892
PAC/ALPACA	0.0280	0.0214	0.0014	0.0280	0.0280	0.0014	0.9519	0.2674	>0.9999	0.0492	0.1072	0.0214
MOC/ALPACA	0.3288	0.0278	0.3288	0.3288	0.0280	0.3288	0.0112	0.0020	0.4845	>0.9999	0.0010	0.0574